VNIVERSITAT DE VALÈNCIA

“Development and optimization of single crystal materials with perovskite structure for optoelectronic applications”

Ismael Fernández Guillén

Directors: Rafael Abargues, Pablo P. Boix, and Said Agouram.

Doctoral thesis from the Doctoral Programme in Physics

Institute of Materials Science
University of Valencia
Juny, 2025

Agradecimeintos

En esta vida hay muchas cosas que no elegimos, como la época o el lugar donde nacemos, así como la familia con la que nos toca vivir. En mi caso, puedo sentirme muy afortunado por la familia que me ha tocado, sin la cual no estaría ahora mismo donde estoy ni tan feliz como me siento. Gracias por vuestras enseñanzas, alegrías y sobre todo por la paciencia y el cariño.

Por otro lado están las situaciones que sí elegimos, al menos aparentemente. Con ello me refiero a los amigos y personas que pretendemos nos acompañen durante esta vida. A este respecto tampoco puedo hacer otra cosa que sentirme igualmente agradecido. Desde los amigos de la infancia y del pueblo, por vuestro amor incondicional y ser una extensión los unos de los otros hasta formar una familia. A los amigos del grado por los buenos ratitos que echábamos incluso en las épocas más difícil de la carrera. A los amigos del máster que aún están ahí, fue un máster idílico gracias a vosotros, muy agradecido por ello. A las personas y amigos que me han acompañado en Valencia durante la tesis, enseñándome a hacer buena ciencia cuando hay que hacerla y a divertirse cuando se hace buena ciencia, anteponiendo siempre lo humano por encima de todo. Gracias por los buenos ratitos y esas noches que se alargaban entre disertaciones de toda índole y algún que otro licor. Finalmente, agradecer a esas personas que llegan a tu vida a darte lecciones (generalmente agradables), sin las cuales no sería quién soy. Gracias por enseñarme de paciencia, de empatía, de diversión y a cultivar el arte de amar.

¨La verdadera ciencia enseña, sobre todo a dudar y sorprenderse¨

Abstract

Metal halide perovskites have recently emerged as highly versatile materials for next-generation neuromorphic computing, owing to their unique combination of electronic and ionic conductivity, low-cost processability, and tunable optoelectronic properties. Within this broad field, single-crystal metal halide perovskites stand out due to their superior structural order, minimal trap density, and enhanced stability, making them ideal candidates for high-performance memristive devices.

This Thesis focuses on the development, fundamental study, and optimization of perovskite single crystals and thin single crystal-based memristors. The work is structured around two primary objectives: first, to enhance the optoelectronic properties of bulk single crystals through novel surface passivation treatments, and second, the development, fundamental study, and optimization of memristive devices based on thin single crystals.

Chapter 3 investigates how surface engineering through laser-induced modification of $MAPbBr_3$ crystals enhances photoluminescence by passivating nonradiative recombination centers, offering insights into optoelectronic processes and crystal lattice dynamics.

Chapter 4 introduces a novel thin single-crystal device based on simple architecture that simultaneously overcomes endurance and switching ratio limitations typically observed in polycrystalline and bulk single-crystal memristors. By optimizing the geometry and leveraging the intrinsic ion-electron interplay in $MAPbBr_3$, devices exhibit a LRS/HRS ratio of up to 50 and endurance exceeding 10^3 cycles, setting new benchmarks in the field.

Chapter 5 further explores the impact of compositional engineering by fabricating both mixed-halide thin single crystals, demonstrating multistate non-volatile switching behavior with the use mixed-halide perovskite single crystal-based memristor. These compositional and morphological engineering unlock defect control, enabling precise modulation of key performance parameters.

Overall, this work aims to comprehensively develop the properties of perovskite single crystals, encompassing both fundamental material enhancements and the advancement of memristive devices based on single crystal architectures. By integrating compositional and morphological engineering, this study provides essential insights and strategies for the realization of stable,

low-power, and high-density memory elements, paving the way for their integration into scalable neuromorphic computing technologies.

Table of Contents

Chapter 1

Introduction to the Thesis

Abstract

This chapter introduces the urgent need for new computing paradigms in light of current limitations in performance and environmental impact. Neuromorphic computing is presented as a promising solution, with metal halide perovskites emerging as novel materials capable of supporting this transition due to their outstanding optoelectronic properties and low-cost synthesis. The chapter outlines the motivations, challenges, and opportunities of leveraging perovskites in neuromorphic architectures.

1.1 Motivation and Context of Memristor Research

Data computing has evolved dramatically since the mid-20th century, transitioning from room-sized mainframes to the portable and powerful devices we use today[1]. The advent of the von Neumann architecture, proposed in 1945, marked a milestone in computing design. This architecture, characterized by the separation of memory and processing units, became the foundation of modern computing. Over the decades, innovations such as the transistor, integrated circuits, and Moore's Law, which predicted the doubling of transistors in microchips approximately every two years, drove exponential growth in computing power and efficiency[2].

However, as we enter the era of big data, artificial intelligence (AI), and the Internet of Things (IoT), the traditional von Neumann model is increasingly unable to meet modern demands. Data-intensive applications require massive computational resources, and the physical and architectural limitations of current systems have begun to hinder progress[3]. The separation between memory and processors in the von Neumann model creates a significant bottleneck, known as the memory wall[4], where the speed of data transfer between these units becomes a limiting factor. This problem is exacerbated as the volume and complexity of data grow, particularly in AI-driven tasks such as neural network training, which require rapid and efficient handling of enormous datasets.

Additionally, Moore's Law is slowing as transistor sizes approach atomic scales, where quantum effects and heat dissipation pose insurmountable challenges[5]. The miniaturization that fuelled decades of advancements is no longer sustainable, underlining the need to seek novel alternatives. Coupled with these challenges are rising energy demands and environmental concerns. Data centers, which power the global digital ecosystem, consume vast amounts of electricity, contributing significantly to greenhouse gas emissions[6]. With increasing reliance on cloud computing and data-intensive technologies, these issues are becoming critical. Furthermore, costs have risen due to the need for advanced infrastructure, expensive hardware, and operational expenses, including cooling systems and power supplies[7].

In this context, emerging technologies and alternative computing paradigms are being explored to overcome these limitations. Particularly, memristors-based technologies represent a meaningful approach in this scenario. Memristors, short for "memory resistors," are a class of electronic devices that combine memory and computation in a single component[8]. This property positions them as a transformative technology in the field of data computing, overcoming limitations as the von Neumann bottleneck or the Moore´s law above mentioned[9]. With their ability to achieve high-speed, low-power, and scalable operation, memristors are poised to revolutionize applications ranging from high-density memory storage to neuromorphic computing[10], [11]. Specifically, neuromorphic computing where memristor devices mimic the adaptive behavior of biological synapses, enabling energy-efficient, real-time learning systems, is illustrating a new approach in the field of data computing[11], [12].

1.1.1 Neuromorphic computing

Neuromorphic computing is a paradigm of computing that seeks to mimic the structure and function of the human brain, specifically how biological neurons and synapses communicate and process information[13]. In the brain, computation and memory are not separate but integrated within neurons and synapses, allowing data to be processed in parallel and with minimal delay. This integration serves as a model for replicating the brain's efficiency in processing information. For instance, the generative pre-trained transformer (GPT) models powering ChatGPT operate on clusters of anywhere from eight to thousands of graphics processing units, each drawing up to 700 watts of power[14]. This large demand of energy consumption is particularly problematic for AI applications, where small devices must operate independently without relying on large external servers or substantial power supplies. By contrast, the most elaborate neural network known, the human brain, operates by consuming about 20 watts of power for a one-hour essay-writing session [15].

At the core, neuromorphic computing makes use of memristors, which are a promising approach to replicate some processes similar to neurons, serving as the fundamental units for emulate brain´s computation and memory storage. The functioning of neuromorphic systems is based on spiking neural networks (SNNs), which is a type of artificial neural network that mimics the way biological neurons communicate using electrical impulses, or "spikes"[16]. Unlike traditional neural networks that process information in continuous or discrete values[17], SNNs encode and transmit information through the precise timing and frequency of spikes. A defining feature of neuromorphic computing is synaptic plasticity, the ability of synapses to adjust their strength based on the frequency and intensity of spikes. This approach allows SNNs to replicate the temporal dynamics of real neural systems, making them closer to the functionality of the human brain, Figure 1. Each neuron and synapse operates independently yet collectively forms a massive parallel processing network, allowing for scalability and the efficient handling of complex tasks[18].

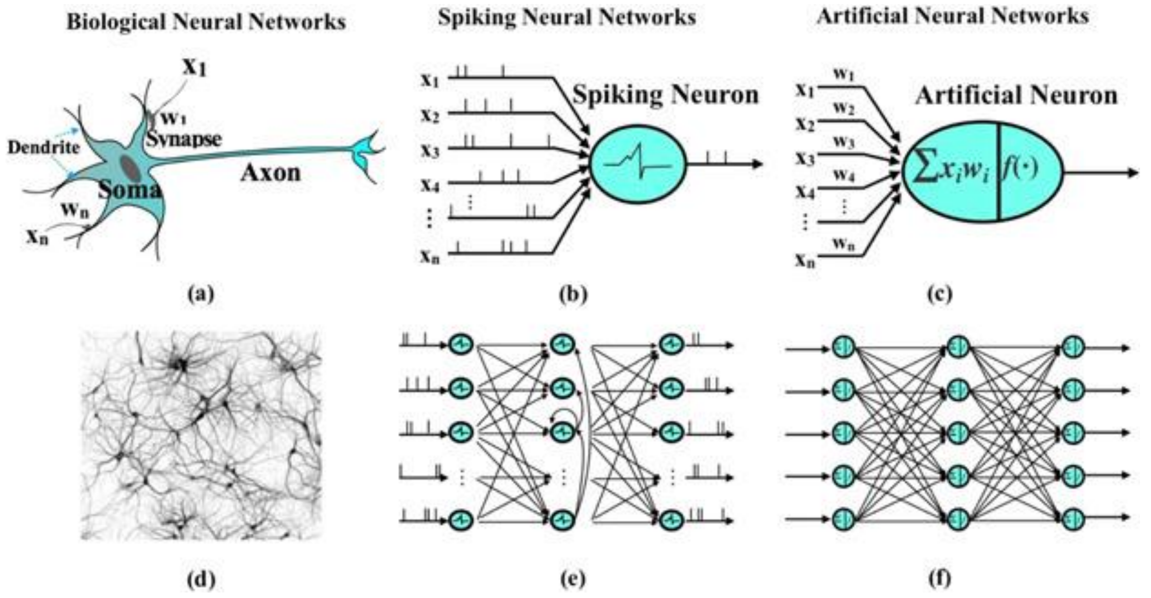

Figure 1. Schematic of the biological neurons networks, spiking neural networks, and artificial neural networks[19].

1.1.2 Devices Architectures for Neuromorphic Computing

This biologically inspired SNN approach requires specialized architectures that not only emulate the behavior of neurons and synapses but also support the efficient processing and learning dynamics unique to SNNs.

One of the most common used architectures is the crossbar array structure[20]. In SNNs, neurons communicate using discrete spikes, and the synaptic weights determine how these spikes influence downstream neurons. The crossbar array structure directly maps these interactions by assigning each crosspoint in the array to a memristive device, which stores the synaptic weight.

In this configuration, the horizontal lines serve as inputs, representing pre-synaptic neurons, while the vertical lines act as outputs, or post-synaptic neurons, Figure 2. This architecture provides a foundation for highly efficient, parallel computation by leveraging the natural alignment of its rows and columns for simultaneous processing. Moreover, the compact design of the crossbar architecture and its scalability allow for the dense integration of numerous processing elements within a small footprint.

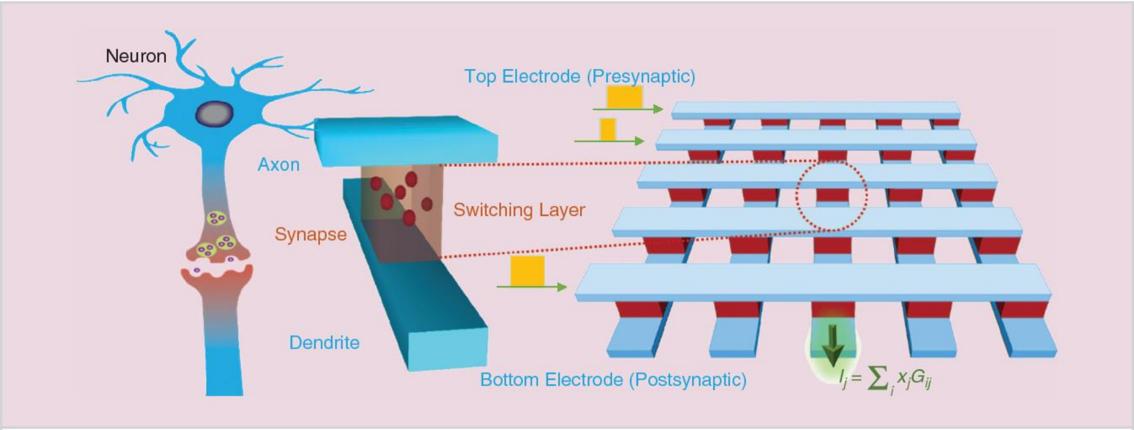

Figure 2. An illustration highlighting the parallels between biological synapses and artificial synapses and networks built using memristors[21].

When a spike (voltage signal) is applied to a row in the crossbar, the memristors multiply the spike signal by the stored weight, and the resulting current flows to the corresponding column, representing the weighted sum of inputs. Each row of the weight matrix W corresponds to the incoming connections for a specific post-synaptic neuron, while each column represents the outgoing connections from a pre-synaptic neuron. The method operates by multiplying the input vector (v) by the weight matrix (G), generating an output vector (I) that reflects the aggregated effect of all pre-synaptic signals on each post-synaptic neuron, Figure 3a. These parameters can be extrapolating to SNN system, where the input vector is defined by (x), the weight is (W) and the output vector is defined by (y), Figure 3b. These operations form the backbone of neural computation and are based on the matrix-vector multiplication (MVM) method[22].

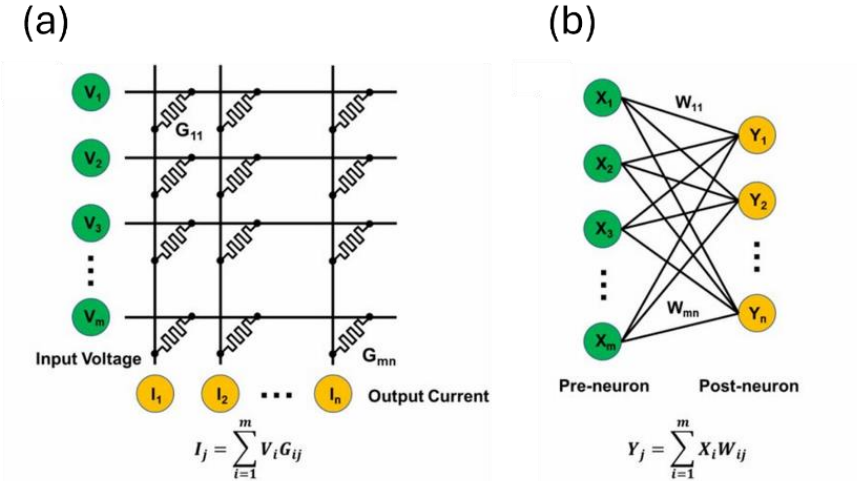

Figure 3. Schematic representation of the analogy between (a) MVM method applied in the crossbar array architecture, and (b) SNN model[23].

To sum up, neuromorphic computation combines memristors, which have the potential to emulate neurons behaviour, in specific architectures such as cross bar array, where memristors facilitate energy-efficient MVM, the core operation underlying signal propagation and learning. This hardware possible to emulate the biological neural network of the brain via SNNs approaches, achieving a compact and scalable design that mimics the parallelism and connectivity of biological brains, Figure 4.

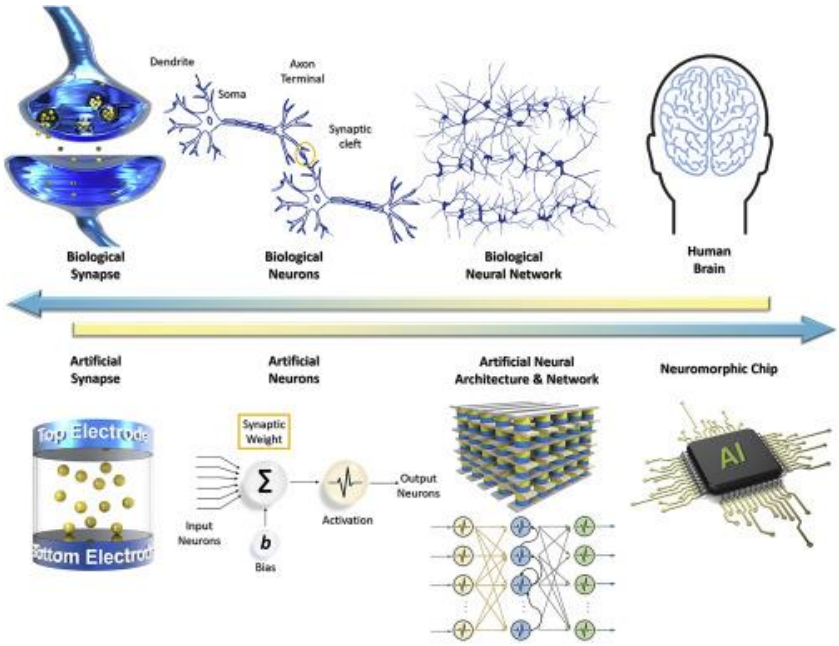

Figure 4. A detailed comparison between the human brain nervous system and artificial neural systems in neuromorphic devices[24].

1.2 Fundamentals of Memristors

The theoretical foundation of the memristor lies in the work of Leon Chua, who mathematically postulated its existence in 1971. Chua's idea emerged from symmetry arguments within circuit theory. Traditional elements describe relationships between pairs of the four fundamental electrical quantities: voltage (V), current (I), charge (q), and magnetic flux (ϕ): Resistors relate V and I, capacitors relate q and V, and inductors relate ϕ and I. Chua proposed that there must be a fourth element to directly link q and ϕ, which he called the memristor[25], equation 1. However, it wasn't until 2008 that researchers at HP Labs, led by Stan Williams, experimentally realized memristors using thin films of titanium dioxide (TiO_2), demonstrating their practical implementation[26].

$$M(q) = \frac{d\phi}{dq} \qquad \text{Equation 1}$$

Regardless of the classical definition, the modern conception of memristive systems has expanded considerably to accommodate the complex physical mechanisms underlying memristive behavior[8]. Most remarkably is that the uniqueness of a memristor lies in its ability of change the resistance states based on the amount of charge that has passed through it, adjusting its resistance accordingly. This state-dependent resistance arises from physical mechanisms such as ionic migration, where ions or vacancies move within the material under an applied electric field, altering local conductivity[27].

The performance of memristors is defined by several key parameters that determine their suitability for various applications. One critical parameter is the resistance states, specifically the high-resistance state (HRS) and low-resistance state (LRS), which correspond to binary "0" and "1" in memory devices. The ratio between these states, known as the LRS/HRS ratio, is essential for ensuring clear differentiation and reliable operation. The set voltage and reset voltage are the thresholds required to switch the memristor into its low and high resistance states, respectively, and they impact the energy efficiency and operational stability of the device. Another important parameter is the retention time, which indicates how long the memristor can maintain its resistance state without power, this is a vital measure for non-volatile memory stability. The endurance of a memristor, or the number of switching cycles it can perform without degradation, determines its longevity and robustness, particularly in applications requiring frequent read/write operations. The switching speed, defined as the time taken to transition between resistance states, is crucial for high-speed memory and logic applications, with faster speeds enabling better performance[10].

Memristors can be broadly categorized into volatile and non-volatile types based on their ability to retain resistance states after the removal of an external stimulus. These categories differ significantly in their properties, operational parameters, and potential applications. Understanding these distinctions is crucial for designing memristor-based systems tailored to specific technological needs.

1.2.1 Volatile Memristors

Volatile memristors are characterized by their transient resistance states, which revert to an equilibrium value once the external stimulus, such as power is removed[10]. This behavior is primarily due to temporary physical changes like polarization or short-lived ionic displacement within the material[28]. These memristors exhibit rapid switching speeds, often in the nanosecond range, making them ideal for applications requiring real-time responsiveness. Energy consumption per switching event is minimal, but their operation requires continuous power to maintain functionality in active systems, leading to higher long-term energy costs for sustained usage[29].

Most remarkably is that volatile memristors, unlike traditional binary devices, can exhibit multistate behavior where the resistance of the device can be tuned to multiple discrete or continuous levels within a range. The multistate behavior in volatile memristors is closely tied to the control of the applied voltage pulses. By varying the magnitude, duration, or frequency of the external stimulus, different resistance levels can be achieved[30], [31], Figure 5. These multistates are particularly valuable in neuromorphic computing, where they emulate the short-term plasticity of biological synapses. In such systems, synaptic weights, analogous to the resistance levels, can be adjusted dynamically to facilitate learning and adaptation in artificial neural networks[29]. Despite their advantages, the transient nature of multistates in volatile memristors poses challenges for long-term data storage.

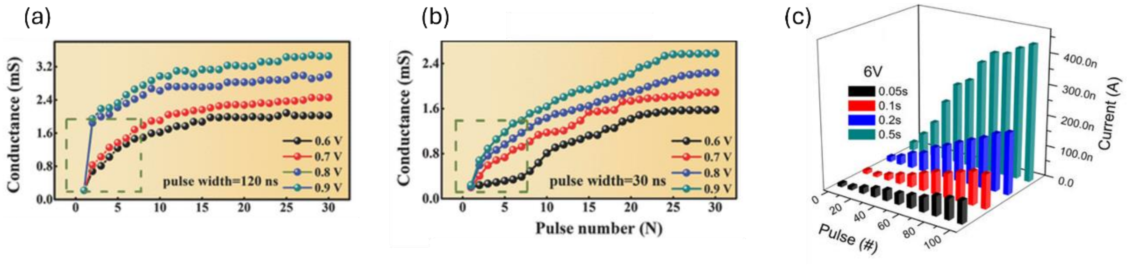

Figure 5. Correlation between the conductance change with different magnitudes (0.9, 0.8, 0.7, and 0.6 V), at different frequencies of pulse width (a) 120 ns, and (b) 30 ns[30]. (c) Conductance response with different pulses duration at 6V[31].

1.2.2 Non-Volatile Memristors

Non-volatile memristors are defined by their ability to retain discrete resistance states indefinitely after the removal of an external stimulus, such as voltage or current[32]. These devices primarily operate in two well-defined resistance states, the HRS and the LRS, which correspond to binary "0" and "1" in memory applications, Figure 6. Unlike volatile memristors, which can support multistate operation due to their transient nature, non-volatile memristors focus exclusively on these two states to ensure reliability, stability, and clarity in data storage and retrieval. This binary operation is particularly advantageous in applications requiring robust and persistent memory, such as resistive random-access memory (ReRAM)[33], [34].

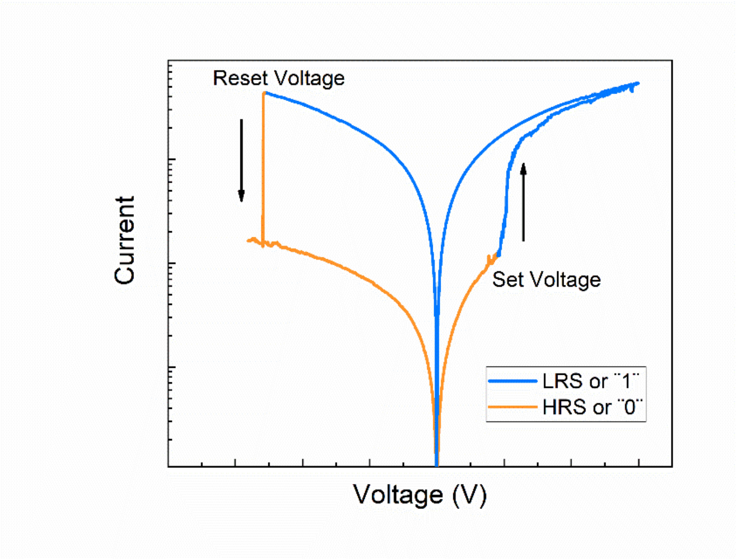

Figure 6. Memristor I-V curve representing the LRS (blue line) and the HRS (orange line) with their respective set and reset voltages.

The performance of non-volatile memristors is defined by several critical parameters that determine their reliability, efficiency, and suitability for specific applications. Retention time is a vital metric, indicating how long the device can maintain its resistance state without external power. Non-volatile memristors are engineered for retention times ranging from years to decades, making them ideal for archival and long-term storage. Endurance, or the number of switching cycles a memristor can withstand without degradation, is another crucial parameter, particularly for applications requiring frequent data rewriting. Switching speed, typically measured in nanoseconds to microseconds, reflects the time required to transition between resistance states. While non-volatile memristors may have slightly slower switching speeds than volatile counterparts, they remain fast enough for most memory and computational tasks. The LRS/HRS ratio is a critical measure of data reliability, as a higher ratio ensures clear differentiation between binary states. Other critical parameters include set and reset voltages, which determine the energy required for state transitions, and overall energy consumption, which is minimized by the non-volatility of the devices.

In terms of applications, non-volatile memristors are pivotal in the development of ReRAM, offering faster speeds, lower power consumption, and higher density compared to conventional flash memory[33]. Beyond memory, their compatibility with crossbar arrays architectures enables parallel processing and in-memory computing, where data storage and computation occur within the same device, which is critical for achieving brain-inspired computational efficiency[35], [36].

As above mentioned, a critical distinction respect to volatile memristors is that non-volatile memristors typically operate in binary states, meanwhile volatile memristor operate with multiples resistance states, allowing neuromorphic applications as it is mentioned above. Nevertheless, the inability of volatile memristors to retain data over time restricts their suitability for applications needing long-term storage.

Neuromorphic devices based non-volatile technology present a compelling alternative offering reliable and persistent data store[36]. However, their applicability is limited when it comes to emulating complex synaptic plasticity, such as gradual weight modulation or spike-timing-dependent plasticity (STDP), which are essential for more advanced and biologically inspired learning[37]. To overcome such limitations, the use of non-volatile devices with multistate states of conductance represents a step forward in the field, although, few devices based on multistate ReRAM have been developed and the mechanism behind multistate behaviour is still misunderstood[38], [39].

1.2.3 Limitations of Traditional Memristors Materials

The materials used to fabricate memristors are diverse, reflecting the wide range of applications and performance requirements for these devices. Each material class offers unique properties that influence the switching mechanism, stability, endurance, and scalability of the memristor.

First generation of memristors was made of metal oxide materials. Metal oxides, such as titanium dioxide (TiO_2), hafnium oxide (HfO_2), and tantalum oxide (TaO_x), are among the most widely studied materials for memristors[40]. These materials exhibit resistive switching due to the migration of oxygen vacancies, which form or disrupt conductive pathways[41]. The advantages of metal oxides include their high switching speeds, and robust non-volatility[40]. They also offer excellent endurance, often supporting millions to billions of switching cycles. Nevertheless, metal oxides still suffering of critical parameters as low LRS/HRS ratio and high set and reset voltages, that is translated in not clear distinction between different states and more energy consumption, respectively[40]. Moreover, a key disadvantage is their variability in performance due to the stochastic nature of filament formation and rupture, which can lead to inconsistencies in resistance states.

Organic materials, such as conductive polymers and small molecules, are the second generation of materials used in memristor fabrication[42]. These materials switch resistively through mechanisms like charge trapping, ion migration, or redox reactions[43]. The primary advantage of organic memristors is their mechanical flexibility and potential for low-cost, large-area fabrication through printing techniques[42]. They are also lightweight and can be processed at low temperatures. However, their major drawbacks include lower switching speeds and high set and reset voltages, with limited endurance due to material degradation, and poorer retention times compared to inorganic alternatives[44]. Their stability under environmental conditions, such as moisture and temperature, also needs significant improvement for broader adoption[44].

Currently, perovskite-based memristors are attracted significant attention due to their high ionic mobility, tunable electronic properties, and ability to achieve both volatile and non-volatile switching offering energy-efficient fabrication and cost-effective performance, including flexible devices[45]. Memristors based on perovskite display high LRS/HRS ratios with extremely low set and rest voltages and long retention times. Nevertheless, the endurance due to ambient degradation of these materials is still a bottleneck to overcome[46].

1.3 Perovskite-based Memristors

In this section it is presented the state of the art of perovskite-based memristors, starting with an overview of perovskite materials. Special emphasis is placed on single crystal (SC) perovskites, as a promise candidate to overpass polycrystalline (PC) counterparts given their superior structural and optoelectronic properties. We discuss their synthesis methods, key physical characteristics, and the advantages they offer for develop different devices. This foundation sets the stage for analyzing their performance and potential in memristive devices.

1.3.1 Perovskite Materials

Metal halide perovskites (MHPs) refer to a class of materials within the crystallographic family of perovskites, characterized by the general stoichiometry ABX_3. In the case of MHPs, A is defined as $CH_3NH_3^+$ (MA), $HC(NH_2)_2^+$ (FA), and Cs^+ cations; B refers to Pb^{2+}, Sn^{2+}; and X concerns to Cl^-, Br^-, I^- halides[47]. The metal is situated in an octahedral halide environment, with the halides located at the vertices, while the cations occupy the gaps within the octahedral structure Figure 7.

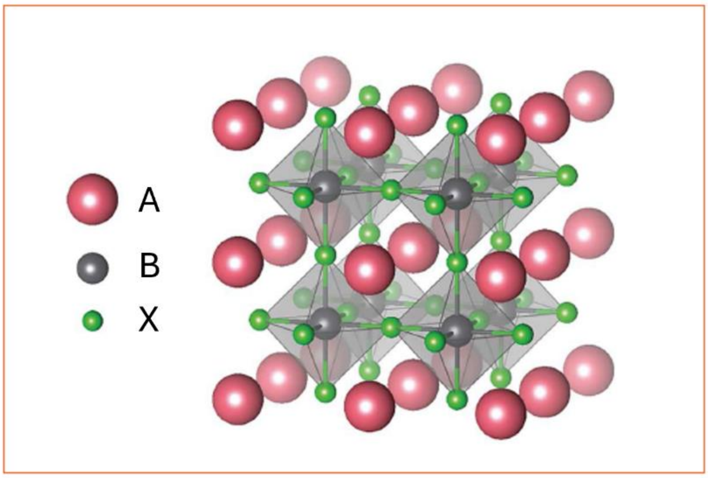

Figure 7. Scheme of ABX_3 perovskite structure.

One of the most remarkable features of MHPs is their exceptional optoelectronic performance. MHPs exhibit high absorption coefficients[48], long carrier diffusion lengths[49], and tunable bandgaps[50], making them ideal for a wide range of devices applications as solar cells[51], laser and light emitting diodes (LEDs)[52], or memristors[53]. Moreover, their defect tolerance is particularly noteworthy, structural imperfections that would degrade the performance of conventional semiconductors, as silicon, have minimal impact on MHPs[54]. This property simplifies fabrication, allowing for low-cost solution processing techniques[55].

Solution-based methods are widely used for the synthesis of perovskites due to their simplicity and scalability. The spin coating technique is the most employed to produce PC thin films[56]. This production of PC perovskites typically involves depositing a perovskite precursor solution onto a substrate, followed by a spin process in which an anti-solvent is added, finishing with a thermal annealing to crystallize the film, Figure 8. This process is straightforward, inexpensive, and adaptable to various substrates, making it suitable for large-scale manufacturing.

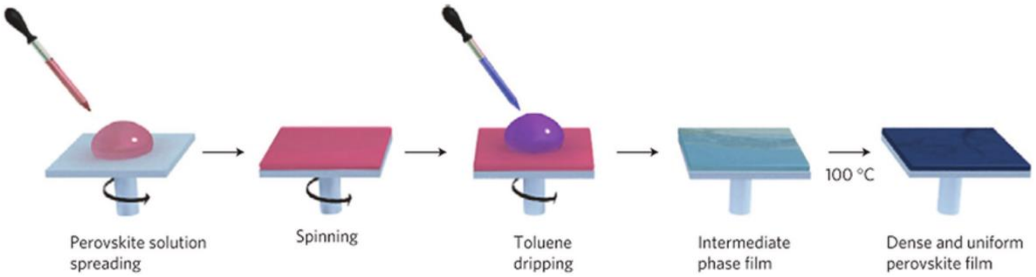

Figure 8**.** Scheme of spin-coating deposition process[57].

However, grain boundaries inherent of PC structures represent important limitations. These grain boundaries act as defect sites, leading to charge carrier trapping and recombination[58], which reduces the efficiency of devices Figure 9a. They can also serve reactive points, accelerating degradation under operational or environmental stress[59]. Although polycrystals dominated perovskite devices manufacturing, SC perovskites are emerging as a promising alternative due to their superior intrinsic properties, such as the absence of grain boundaries, which eliminates charge trapping and reduces recombination losses[60], [61], Figure 9b. Moreover, their long-range crystalline order results in exceptional charge carrier mobilities, extended diffusion lengths, and enhanced stability under environmental stress[62], [63]. Nevertheless, SCs still suffer from large-scale synthesis[64]. Additionally, their growth processes can result in non-uniform crystal sizes and surface defects, which require advanced passivation and surface treatments to mitigate[65], [66]. These challenges underscore the need for continued research to overcome the limitations of SC perovskites while their PC counterparts continue to provide a straightforward path to the development of high-efficiency devices.

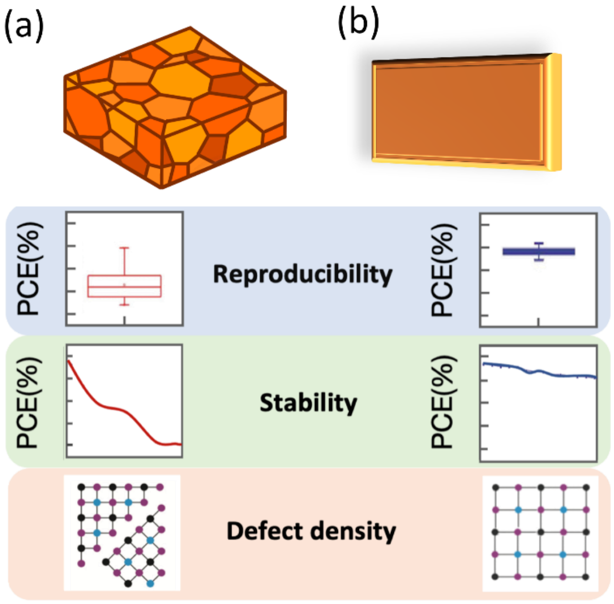

Figure 9. Schematic representation of (a) polycrystalline perovskite film, and (b) single crystal perovskite, with their corresponding keys parameters.

In the field of devices applications, MHPs have particularly revolutionized the field of photovoltaics, emerging as one of the most promising materials for next-generation solar cells[67]. In just over a decade, MHP-based solar cells have achieved power conversion efficiencies (PCE) exceeding 26%[68], rivalling silicon counterparts. This significant progress represents a unified effort in different fields that leaves behind a legacy of understanding of the fundamental physic of perovskite materials, which can be leveraged for the development of new technologies. For instance, the study of the ionic nature in solar cells devices and its effects on electronic behavior has established a new field of applications for memristive devices and neuromorphic computation.

The ionic nature of MHPs arises from their flexible lattice structure, where weak interactions between ions allow for easy migration under external stimuli such as electric fields or temperature gradients[69]. The mobility of these ions occurs through mechanisms such as vacancy hopping or diffusion[70], [71]. One of the most prominent effects of ionic mobility is the hysteresis observed in current-voltage (I-V) measurements. As ions migrate under an applied electric field, they alter the internal electric field distribution within the perovskite layer. This redistribution of charge results in transient polarization effects, causing the current response to depend on the direction and speed of the voltage sweep[72], [73]. For example, in perovskite solar cells, this leads to forward and reverse I-V curves that do not overlap. Depending on the discrepancies between the forward and reverse scans (FS, and RS respectively), two physical phenomena can be defined: a capacitive effect occurs if the RS exhibits higher current than the FS, and an inductive effect occurs if the RS exhibits lower current than the FS, figure 10.

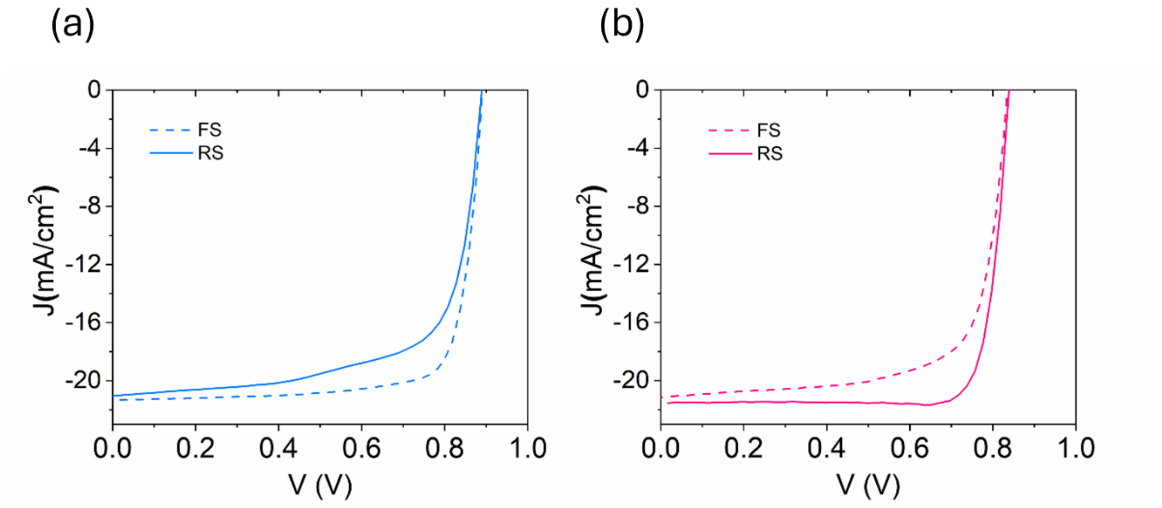

Figure 10. (a) Capacitive, and (b) inductive hysteresis of halide perovskite solar cells under illumination.

Capacitive effects arise from the intrinsic dielectric properties of the perovskite material itself. Perovskites have relatively high dielectric constants[74], meaning they can store significant amounts of charge in response to an external electric field. During the FS, the capacitor is charges, while in the RS it discharges, this results in a higher current in the RS compared to the FS[73].

Inductive effects, originate due to the accumulation of charges at interfaces and within the bulk of the perovskite material when subjected to an electric field. This accumulation generates a layer of ions at the interfaces which is linked to delayed current responses and recombination processes[75], originating inductive effects, resulting in higher current in the FS compared to the FS.

Hysteresis is strongly dependent on factors such as voltage, waiting time, scan rate, and the nature of the interfaces. Higher voltages, longer waiting times, or slower scan rates facilitate ion migration, leading to accumulation at the interfaces and the emergence of inductive effects. Conversely, lower voltages, shorter waiting times, or faster scan rates hinder ion migration through the bulk, reducing the accumulation at the interfaces[75].

Interestingly, the inductive behavior in I-V measurements of solar cells, driven by ionic migration, charge accumulation, and polarization, closely mirrors memristive dynamics where resistance dynamically changes based on the history of voltage applied to the device. Such phenomena observed in I-V characterization of solar cells have been one of the main driving forces in the development of perovskite-based memristors.

1.3.2 Single crystal Perovskite Materials

As previously mentioned, SC perovskites represent a promising alternative to their PC counterparts. Unlike PC films, which consist of multiple crystalline domains separated by grain boundaries, SCs feature a continuous and defect-minimized lattice structure. This absence of grain boundaries effectively mitigates charge trapping, non-radiative recombination, and degradation pathways commonly observed in PC materials. The superior optoelectronic properties of SC perovskites, such as enhanced carrier mobility, prolonged carrier lifetimes, and lower trap-state densities, illustrate their potential for high-performance device applications. These properties are described in detail in the following section.

1.3.2.1 Optoelectronic properties of perovskite single crystals.

i) Optical Properties

In optoelectronic devices, the bandgap energy of the semiconductor governs its optical absorption spectrum by setting the threshold photon energy required for electronic excitation. In perovskite materials, the bandgap can be precisely tuned through halide and cation substitution[50]. For instance, $MAPbX_3$ SCs exhibit bandgaps of 1.53 eV (X=I), 2.24 eV (X=Br), and 2.97 eV (X=Cl), Figure 11a,b. Mixed-halide systems allow for continuous bandgap tuning across this range, enabling spectral response engineering Figure 11c,d. The bandgap tuning directly reflect in properties such as photoluminescence (PL) response, figure 11e.

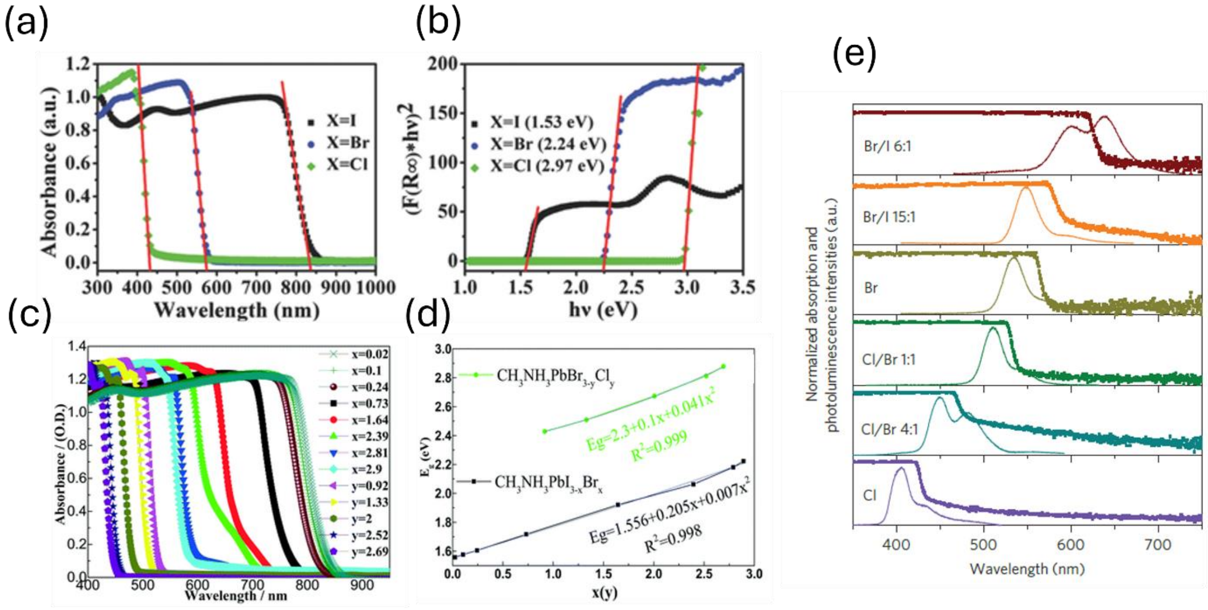

Figure 11. (a) UV–vis–NIR absorption spectrum of $CH_3NH_3PbX_3$ (X = Cl, Br, I) SCs, (b) estimate the optical bandgap of each material composition[76]. (c) Absorbance spectra of $CH_3NH_3PbI_{3-x}Br_x$ and $CH_3NH_3PbBr_{3-y}Cl_y$ SCs, and (d) Relationship between the extracted optical bandgap and the halide content (x or y)[77]. (e) absorption spectra (squares) and photoluminescence spectra (solid lines) of single-halide and mixed-halide perovskite SCs[78].

A-site substitutions (e.g., replacing MA^+ with FA^+ or Cs^+) have a comparatively smaller effect on the bandgap but significantly influence the lattice stability and phase behavior[79]. Substituting the B-site cation with Sn^{2+} (as in $MASnI_3$) reduces the bandgap to ~1.15 eV, extending light absorption into the near-infrared[80].

SCs also exhibit extended absorption onsets due to their thickness and reduced in-gap defect states. For example, $MAPbI_3$ SCs show a redshifted absorption edge (~900 nm) compared to films (~800 nm), attributable to their weakly indirect bandgap (~60 meV below the direct transition)[81]. The optical behavior can be further modulated by varying the number of inorganic layers, which affects both the bandgap and the excitonic nature of the absorption and emission[82].

ii) Carrier transport

Carrier transport in SCs is governed by carrier mobility, lifetime, and diffusion length, all of which are significantly enhanced relative to polycrystalline films[83]. Carrier mobility can be evaluated using a variety of techniques, including space-charge-limited current (SCLC) method, Hall effect measurements and, time-of-flight (TOF) analysis[84]. Lifetime can be characterized by time-resolved photoluminescence (TRPL), Transient Absorption Spectroscopy (TAS), and transient photovoltage (TPV) techniques[85], [86], [87]. Diffusion length can be determined by Scanning Photocurrent Microscopy (SPCM), and Surface Photovoltage (SPV) techniques[88]. Each of these approaches provides distinct insights into charge transport behavior under different experimental conditions. Regardless of the specific characterization technique employed, single crystal metal halide perovskites (SC-MHP) consistently exhibit significantly higher carrier mobility compared to their PC counterparts[83], [84].

In PC perovskite films, the high density of grain boundaries introduces structural defects that create deep trap states within the bandgap, leading to carrier trapping and limited transport efficiency. Conversely, SC-MHP, characterized by the absence of grain boundaries, exhibit substantially reduced point defect densities. This structural coherence facilitates enhanced carrier mobility and enables more efficient charge transport behavior.

In perovskites, the carrier transport parameters, conductivity (σ), mobility (μ), and diffusion length (L_D), can be accurately assessed using the SCLC method[89]. This technique involves measuring the dark current–voltage response of a symmetric device. The resulting I–V curve typically features three regimes: the Ohmic region (linear current increase), the trap-filled limit (TFL) region, and the trap-free Child's region (quadratic current increase).

In the Ohmic region, the electrical conductivity is calculated using the relation:

$$\sigma = \frac{I}{VL} \qquad \text{Equation 2}$$

where I is the current, V is the applied voltage, and L is the thickness of the crystal.

The trap density n_t, representing the density of electrically active defect states, is extracted from the transition voltage between the Ohmic and TFL regions using:

$$n_t = \frac{2\varepsilon\varepsilon_0 V_{TFL}}{qL^2} \qquad \text{Equation 3}$$

Here, $\varepsilon$is the relative permittivity of the crystal (obtained from capacitance–frequency measurements), ε_0 is the vacuum permittivity, q is the elementary charge, and V_{TFL} is the trap-filled limit voltage.

Once traps are filled, carrier transport becomes space-charge-limited and the carrier mobility can be calculated in the Child regime using Mott–Gurney's law:

$$\mu = \frac{8L^3 J_D}{9\varepsilon\varepsilon_0 V_b^2} \qquad \text{Equation 4}$$

where J_D is the current density and V_b is the applied voltage.

Carrier mobilities in SCs typically range from 10 to over 500 $cm^2V^{-1}s^{-1}$, depending on the composition and measurement method (ToF, Hall effect, SCLC)[84]. For example, $MAPbI_3$ SCs show mobilities up to 164 $cm^2V^{-1}s^{-1}$ (SCLC), while $CsPbBr_3$ SCs exceed 500 $cm^2\ V^{-1}\ s^{-1}$. These high mobilities are paired with long carrier lifetimes, often reaching hundreds of microseconds[90], due to the suppressed trap-assisted recombination. The combination of high mobility and long lifetime leads to diffusion lengths over 175 µm[91].

Anisotropic transport has also been observed in SCs with different crystallographic orientations. For instance, the (110) facet of $MAPbBr_3$ exhibits longer carrier lifetimes and lower dark current compared to the (100) facet, due to differences in trap densities and surface defect distributions[92]. Such orientation-dependent behavior is critical for optimizing SC integration in planar device architectures.

iii) Ion Migration

Although perovskite SCs lack grain boundaries, commonly considered primary ion migration pathways in PC films[93], they are not exempt from ionic movement. Point defects such as halide (I^-) and organic cation (MA^+) vacancies and interstitials remain mobile under external stimuli, including electric fields and photoexcitation. Activation energies for ion migration typically range from 0.1−0.6 eV for I^- vacancies and interstitials, 0.5−1.2 eV for MA^+ vacancies and interstitials, and >1 eV for Pb^{2+} vacancies, suggesting that both the halide anion and the organic cation can migrate[94], [95].

Light illumination accelerates ion migration by lowering activation energies, e.g., from 0.83 eV (dark) to 0.33 eV (illumination) for $MAPbI_3$[96]. This behavior contributes to hysteresis in device I-V measurement and can lead to long-term instability in devices such as solar.

Strategies to suppress ion migration in SCs include compositional tuning (e.g., incorporating GA^+ or Sr^{2+}), dimensional reduction (e.g., 2D/quasi-2D perovskites), and passivation techniques[97], [98], [99]. These strategies suppress ion migration by increasing lattice rigidity and introducing interfacial charge repulsion, which together block pathways for mobile species like halide and organic cation vacancies. Nevertheless, ion migration remains a key challenge for reliable SC-based devices, particularly under continuous operation or electric bias.

iv) Defects

In perovskite SCs, the overall defect density is significantly lower than in their PC counterparts due to the absence of grain boundaries, which are major sources of structural disorder in thin films. However, the dominant origin of defects in SCs shifts to the crystal surface, where the lattice is more susceptible to disruption. Surface termination leads to incomplete coordination of ions, and interactions with ambient conditions (such as moisture and oxygen) contribute to the formation of shallow point defects, such as halide vacancies and interstitials[100].

The space-charge limited current technique is one of the most widely employed methods to quantify trap densities in perovskite materials. As mentioned above. This technique involves fabricating a single-carrier device, typically with electron-only or hole-only transport layers, and measuring the I–V response under dark conditions. At low voltages, the current exhibits an Ohmic behavior, while at higher voltages, it transitions into a TFL regime. The voltage at which this transition occurs is known as the trap-filled limit voltage (V_{TFL}), and it marks the point at which the injected carrier density equals the trap density. The trap density n_t can be calculated using the equation 5.

$$V_{TFL} = \frac{en_t L^2}{2\varepsilon\varepsilon_0} \qquad \text{Equation 5}$$

Where ε is the relative dielectric constant of the perovskite, ε_0 is the vacuum permittivity, V_{TFL} is the trap-filled limit voltage, q is the elementary charge, and L is the thickness of the perovskite material.

The SCLC method has proven effective in quantifying trap densities in high-quality perovskite SCs. Reported values in can be as low as 10^8–10^{11} cm^{-3}, significantly lower than the typical 10^{14}–10^{18} cm^{-3} found in PC films[101], [102].

The crystallographic facet also influences defect distribution and recombination dynamics in perovskite SCs. For instance, the (112) plane of $MAPbI_3$ shows more defects than the (100) plane, affecting local carrier dynamics and photophysical properties[103]. Demonstrating that orientation control during crystal growth is therefore essential for minimizing defect-related losses.

v) Stability

The stability of perovskite SCs under environmental and operational stress is one of their most compelling advantages. Their lack of grain boundaries blocks facile diffusion pathways for moisture and oxygen, dramatically improving air and thermal stability. $MA_{0.45}FA_{0.55}PbI_3$ SCs have demonstrated stability in ambient air for over 14 months without encapsulation, retaining structural integrity and optical appearance[104] contrasting with the faster degradation of polycrystalline counterpart at ambient conditions[105].

Nevertheless, light-induced degradation remains a concern. As mentioned above, Illumination reduces the activation energy required for halide and organic cation vacancies to move within the lattice. Recent studies have shown that prolonged light exposure can lead to the generation of new trap states in perovskite SCs. These traps, often located near the surface or interfaces, can act as nonradiative recombination centers, reducing carrier lifetimes and overall device efficiency, leading to performance degradation over time even in high-quality SCs[106], [107].

1.3.2.2 Single crystal perovskites synthesis methods

To unlock the outstanding optoelectronic properties of perovskites, it is essential to synthesize high-quality SCs. While PC perovskites are commonly fabricated via spin-coating, a rapid and scalable technique that typically does not require stringent control over the crystallization conditions, SCs growth demands much more precise regulation of parameters such as temperature, solvent composition, and supersaturation.

Various synthesis methods have been developed to grow these crystals with precise control over size, morphology, and thickness. Among the most widely used techniques are solution-based methods and vapor-phase growth, each offering distinct advantages and limitations depending on the target application[108], [109]. Here we focus on the solution-based methods, due to its simplicity, cost-effectiveness, and ability to produce high-quality crystals with controlled dimensions. To achieve controlled nucleation and centimetre scale crystals, four primary strategies are employed: (i) temperature-cooling crystallization (TCC), wherein solubility decreases upon cooling acidic or aqueous halide-rich solutions; (ii) antisolvent vapor-assisted crystallization (AVC), where controlled vapor diffusion of a miscible poor solvent triggers supersaturation and growth; and (iii) inverse temperature crystallization (ITC), which exploits the anomalous solubility behavior of certain perovskites in polar aprotic solvents such as γ-butyrolactone (GBL), dimethylformamide (DMF), and dimethyl sulfoxide (DMSO); and, (iv) confined inverse temperature crystallization (CITC), a modified version of ITC where crystal growth is physically restricted between two surfaces or within defined geometries, allowing precise control over crystal thickness. Each of these techniques offers distinct advantages in terms of speed and crystal quality, and morphology control, and will be discussed below.

i) Temperature Cooling Crystallization (TCC)

Among the earliest reported methods, TCC relies on the decrease in solubility of perovskite precursors at lower temperatures[108]. In this process, a saturated solution, often based on hydrohalic acids such as HI or HBr, is gradually cooled from elevated temperatures (e.g., 100 °C) to ambient conditions. This facilitates slow and steady crystal growth as solubility decreases. TCC is particularly effective for growing large crystals with high structural quality, including various 3D and low-dimensional systems. However, the method is inherently slow (often requiring weeks), and the lack of precise control over temperature gradients and supersaturation levels can lead to phase transitions or defect formation.

ii) Antisolvent Vapor-Assisted Crystallization (AVC)

The antisolvent vapor-assisted crystallization (AVC) method offers a strategy for growing high-quality SCs under ambient or low-temperature conditions, particularly when thermal stability is a concern[110]. This technique exploits the differential solubility of perovskite precursors in miscible solvent–antisolvent pairs. Typically, the perovskite precursors (e.g., PbX_2 and AX, where A = MA^+, FA^+, Cs^+, and X = Br^-, Cl^-, I^-) are dissolved in a solvent with high precursor solubility like DMF, GBL, or DMSO. The solution is then exposed to the vapor of a solvent with low precursor solubility, such as toluene, diethyl ether, or dichloromethane, which slowly diffuses into the solution. As the antisolvent vapor permeates the precursor solution, it gradually lowers the solubility of the perovskite, inducing supersaturation and subsequent nucleation, Figure 12.

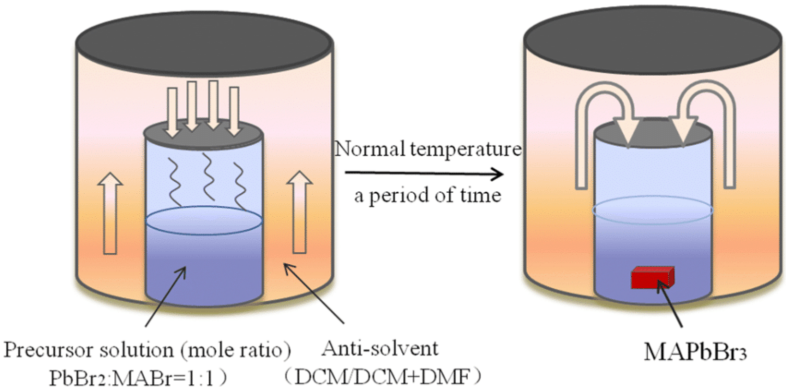

Figure 12. Schematic diagram of perovskite SCs growth via AVC method[111].

The vapor-phase diffusion ensures slower and more controlled supersaturation, which is crucial for high crystal quality. The AVC approach has enabled the synthesis of $FAPbX_3$, $MAPbX_3$ (X = I, Br), $CsPbBr_3$, and various low-dimensional or lead-free perovskites with well-defined facets[108]. However, AVC requires precise control over the diffusion rate of the antisolvent. If the process is too fast, uncontrolled nucleation and polycrystalline aggregation may occur, if too slow, the yield becomes impractically low.

iii) Inverse Temperature Crystallization (ITC)

Among the most widely adopted techniques for growing perovskite SCs, ITC takes advantage of a unique and non-classical solubility behavior exhibited by many halide perovskites in specific solvents[112]. Contrary to the usual trend where solubility increases with temperature, in solvents like GBL, DMF, and DMSO, compounds such as $APbX_3$, (where A = MA^+, FA^+, Cs^+, and X = Br^-, Cl^-, I^-) display inverse solubility, meaning their solubility decreases as temperature rises.

In practice, a saturated solution is prepared at room temperature and then gradually heated, typically within the range of 80–120 °C. As the solution enters a supersaturated state, nucleation initiates, followed by rapid crystal growth, Figure 13. By carefully tuning solvent composition, precursor concentration, and heating rate, it is possible to obtain large, high-quality crystals within hours, orders of magnitude faster than temperature-cooling or antisolvent vapor-assisted crystallization techniques.

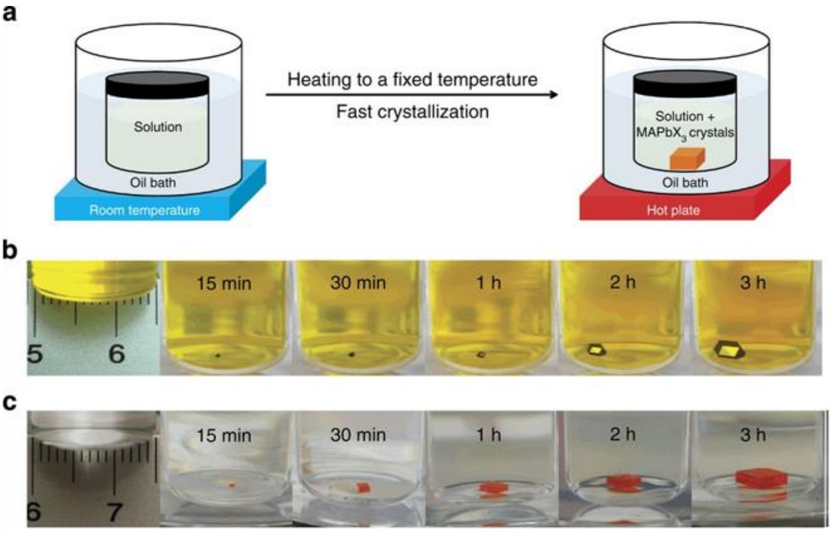

Figure 13. (a) Schematic illustration of the (ITC setup, where the vial containing the precursor solution is immersed in a temperature-controlled heating bath. The solution is gradually heated from room temperature to elevated setpoints, approximately 80 °C for $MAPbBr_3$ and 110 °C for $MAPbI_3$, to induce crystallization. (b, c) Time-resolved growth of $MAPbI_3$ and $MAPbBr_3$ SCs, showing progressive enlargement and facet development at various intervals[112].

ITC has proven particularly effective in generating centimetre scale crystals, especially when combined with seed-assisted growth to ensure directional control and suppress spontaneous nucleation. Moreover, the method has been extended to mixed-cation (e.g., FA/MA/Cs) and mixed-halide systems, although the presence of multiple precursors can introduce challenges related to phase segregation and solubility mismatch[113].

iv) Confined Inverse Temperature Crystallization (CITC)

Confined inverse temperature crystallization, is an evolution of the conventional ITC method, designed to overcome key limitations of bulk SC perovskites, such as the excessive thickness relative to efficient charge extraction and device integration[114]. CITC addresses these issues by physically restricting crystal growth within defined spatial boundaries, typically between two substrates, reducing the thickness of the SCs from hundreds of microns to a few micrometers, obtaining thin single crystals (TSC), Figure 14.

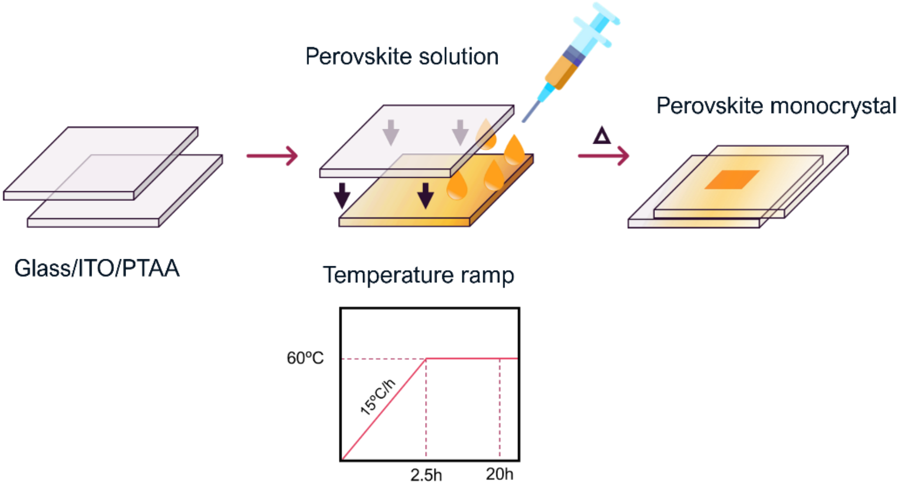

Figure 14. Scheme of the CITC method to fabricate thin perovskite SCs.

In this method, a saturated precursor solution, such as $MAPbI_3$ in GBL, is injected or drop-cast into a narrow space created by parallel substrates. Upon heating, the inverse temperature solubility behavior triggers crystallization, but the vertical expansion is limited by the confinement geometry. As a result, crystals grow laterally, yielding thin, and flat SC perovskite layers with tunable thicknesses ranging from several hundred nanometers to a few micrometers.

CITC method has been successfully applied in devices with planar structures, such as solar cells, memristors, and photodetector, where efficient charge extraction and device integration are critical for achieving high performance[114].

In this thesis we focus on the ITC and CITC method to fabricate bulk SC and TSC, respectively. We discard solution-based synthesis methods like vapor-assisted crystallization or slow evaporation, because, although they do not require an increase in temperature, their synthesis times extend over several days, even weeks, whereas the ITC and CITC methods require only a few hours.

1.3.2.4 Devices based on single crystals perovskites

In terms of devices, their superior structural and optoelectronic characteristics, as above described, make them highly promising for applications in solar cells, photodetectors, LEDs, laser and memristors.

i) Solar cells

Single crystal perovskites have the potential to surpass the efficiency and stability limitations of polycrystalline perovskite solar cells (PC-PSCs). In conventional PC-PSCs, grain boundaries act as charge trap sites, increasing recombination and reducing charge extraction efficiency. However, (single crystal perovskite solar cells) SC-PSCs eliminate these grain boundaries, leading to significantly improved carrier transport properties and higher power conversion efficiencies. Another major advantage of SC-PSCs is their enhanced operational stability. In PC films, ion migration at grain boundaries contributes to instability and hysteresis effects. Since SCs lack grain boundaries, they exhibit reduced ion migration, leading to improved long-term stability. For instance, SC-PSCs have exceeded 24% PCE since their first report in 2016, approaching the 26% efficiency achieved by their polycrystalline counterparts, which were first reported in 2009[68], [115].

ii) Photodetectors

Photodetectors are devices that convert light signals into electrical signals, making them essential for applications such as imaging, optical communication, biomedical sensing, and environmental monitoring. Perovskite SC photodetectors exhibit high photoresponsivity, fast response times, and low dark currents due to their excellent charge transport properties and low trap densities[116].

For instance, $MAPbI_3$ SCs photodetectors have exhibited detectivities exceeding 10^{12} Jones and response times below 1 µs, outperforming their PC thin-film counterparts by several orders of magnitude[117]. These metrics are further enhanced by the sharp absorption edges and high optical quality intrinsic to SCs, enabling efficient photogeneration and collection of charge carriers.

iii) LEDs and lasers

SC-MHP have emerged as promising candidates for next-generation light-emitting technologies, including LEDs and lasers, owing to their exceptional optical gain, narrow emission linewidths, and high photoluminescence quantum yields (PLQYs)[118].

In LEDs, radiative recombination efficiency is the central performance metric, and perovskite SCs provide a near-ideal platform to maximize this. Several studies have reported external quantum efficiencies (EQEs) exceeding 10% in SC-based devices. For instance, Song et al. demonstrated a $MAPbBr_3$ SC-LED with an EQE of 11.7% and stable operation over 30 hours at 100 cd/m^2, enabled by a surface engineering approach that passivated shallow traps and improved hole transport[119].

Regarding to lasers applications, the high optical quality, low defect density, and long carrier diffusion lengths of perovskite SCs facilitate population inversion and reduced threshold energy for lasing. Notably, SCs can support both optically and electrically pumped lasing, although the former is more widely studied. For example, $MAPbBr_3$ and $CsPbBr_3$ SCs have been extensively explored for microcavity lasing. Zhang et al. reported room-temperature continuous-wave lasing from $CsPbBr_3$ SCs using a distributed feedback cavity design, achieving a threshold as low as 0.3 $\mu J/cm^2$ and linewidth narrowing below 0.2 nm[120].

iv) Memristors

Memory devices require high carrier mobility, defect tolerance and stable electrical performance. Due to the absence of grain boundaries, SC-MHP, are intended to show all these key advantages and translated them in excellent LRS/HRS ratios, high endurance and low power energy consumption memristors. Specifically, the endurance of these devices, a critical parameter, can be improved by using SC-based memristors, as the absence of grain boundaries eliminates reactive sites where perovskite materials tend to degrade.

Despite their potential, SC-based memristors are still in the early stages of development. Few devices based on SC has been fabricated[121], [122], [123] where further rigorous research is necessary to fully evaluate key parameters as endurance, retention time, and the underlying switching mechanisms take advantage of the higher robustness of SC materials. One of the goals in this thesis, as it is explained to the final of this chapter, is address such questions to unlock the full potential of SC-based memristors in high-performance memory and computing applications.

1.3.3 State of the Art of Perovskite-based Memristors

Since the first report of the memristive properties in perovskite materials, perovskite-based memristors have experienced a significant development[124]. One of the key properties that position MHPs as straightforward in the memristor field is their intrinsic ion mobility[125]. Their ionic nature is translated in properties as superior LRS/HRS ratio, lower set and reset voltage and the ability to achieve non-volatile and volatile memristor[126], [127]. Moreover, their high defects tolerance allows low-cost solution fabrications methods and enhances their memristive properties, as intrinsic defects like halide vacancies facilitate ionic mobility[56].

Nevertheless, the polycrystalline nature of these perovskite memristors is characterized by grains separated by grain boundaries, which significantly influence the performance and reliability of these devices. Grain boundaries act as defect density sites, which accelerate degradation mechanisms under operational conditions, such as voltage stress or exposure to environmental factors like moisture and oxygen[58], [59]. As a result, devices often experience reduced retention times, diminished endurance, which are critical parameters in memristor devices[124].

Efforts to mitigate the disadvantages of the polycrystalline nature include strategies as grain boundary passivation using chemical agents[128], advanced fabrication techniques, such as slow crystallization or solvent engineering to increase grain size and reduce boundary density[129], or the fabrication of more complex architecture devices by adding different metal layer[130], which increases the fabrication cost. While these approaches improve stability, they cannot fully replicate the superior performance of SC perovskite materials[61], which lack grain boundaries altogether. Unfortunately, 3D perovskite SC memristor devices approach remain mostly unexplored, where no efficiency devices, with high set and reset voltage[121], or without endurance test[131] have been reported.

1.3.3.1 Mechanism behind Perovskite-based Memristors

The discussion surrounding the mechanisms of resistive switching in perovskite-based memristors is a topic of significant interest and debate that remains inconclusive. Such discussion primarily revolves around two dominant phenomena: filamentary switching, driven by the migration of ions and vacancies[132], and interfacial effects, which involve charge accumulation or redistribution at the electrodes' interfaces[133].

In the filamentary switching mechanism, resistive switching is attributed to the migration of ionic species, such as halide vacancies or metal ions, under the influence of an external electric field[134]. These mobile ions form localized conductive filaments that bridge the insulating gaps within the perovskite layer, resulting in the LRS. The subsequent rupture of these filaments under reverse bias restores the HRS, Figure 15a. Filamentary switching is often associated with abrupt changes in resistance, which, offers an efficient pathway for achieving high switching speeds and low power consumption[134]. Notably, the filamentary switching process is inherently stochastic, as the formation and rupture of these filaments depend on the local distribution of vacancies and defects within the material. This stochastic nature of filament formation and rupture introduces variability in switching behavior and device performance. For example, the localized migration of ions can lead to non-uniform filaments, resulting in device-to-device variability. Additionally, prolonged filamentary switching can accelerate material degradation, reducing the lifetime and stability of the devices[135]. Nevertheless, to mitigate this degradation by filamentary process, the use of inert electrodes such as Pt or Au, rather than reactive electrodes, reduces the likelihood of the chemical reactions that could alter filament behavior[136].

Alternatively, interfacial mechanisms are attributed to the accumulation or redistribution of ionic species, vacancies, or charge carriers at the interfaces between the perovskite active layer and the device electrodes[137]. In this model, resistive switching occurs due to changes in the interfacial potential barrier or charge carrier transport near the contacts. Ions, such as halide vacancies, accumulate at the electrode interfaces under an applied bias, which modulates the Schottky barrier, thereby altering the device's resistance[138], Figure 15b. Unlike the localized nature of filamentary switching, interfacial effects are often more spatially distributed and provide smoother transitions between resistance states[132]. This behavior is particularly advantageous for applications requiring analog (multistate) switching, such as neuromorphic computing, where a continuous range of resistance states is needed to emulate synaptic weights.

Compared to filamentary switching, interfacial mechanisms are typically more uniform and spatially distributed, as they do not rely on the formation of localized conductive pathways. This uniformity can lead to improved switching reproducibility and device stability over extended operational cycles. Furthermore, interfacial mechanisms are less susceptible to stochastic behavior, making them more suitable for applications requiring high reliability and endurance.

However, interfacial switching also presents challenges, particularly in terms of device stability and the slow migration of ionic species over repeated cycles. Prolonged operation can lead to electrode degradation, interfacial reactions, or drift of the ionic distribution, all of which can affect the device's switching performance[139]. Strategies to address these challenges include interface engineering, such as the use of buffer layers, passivation techniques, which minimize chemical reactions and maintain stable interfaces[139], [140], [141], [142].

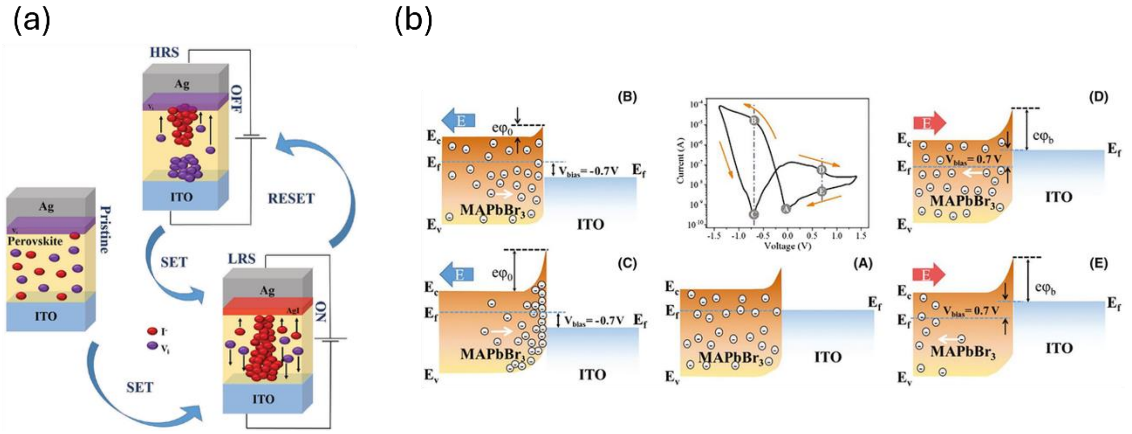

Figure 15. (a) Filament[143], and (b) interfacial[138] mechanism resistive switching scheme in perovskite-based memristors.

The interplay between these two mechanisms, filamentary and interfacial, remains an area of active research. In some cases, both processes may coexist, and their relative contributions can depend on the specific device structure, material composition, and operational conditions. For example, devices with higher defect densities and reactive electrodes may favor filament formation, whereas devices with well-engineered interfaces may exhibit interfacial switching as the dominant mechanism. This duality underscores the complexity of perovskite memristors and the need for a deeper understanding of the material's defect chemistry, ion transport dynamics, and interface physics.

An additional interesting process in perovskite memristors is known as electroforming. The electroforming process is a crucial step in the activation of many perovskite-based memristors, preparing them for reliable resistive switching behavior. During this process, an initial voltage, typically higher than the operational switching voltage, is applied to the device to induce structural and electronic changes in the perovskite layer. These changes could involve the redistribution of ionic species, defect generation, or the formation of conductive filaments, creating a pathway for subsequent low-voltage switching between the HRS and the LRS[144], [145]. The magnitude of this forming voltage depends on the material composition, electrode configuration, and device thickness[145], [146]. After forming, the device stabilizes, transitioning from a pristine state to an active memristive state. The forming process establishes a baseline configuration for repeatable resistive switching during subsequent voltage cycles.

Overall, elucidating the precise mechanisms behind resistive switching and electroforming process in perovskite-based memristors is essential for optimizing their performance and addressing current challenges such as stability, reproducibility, and scalability. By tailoring material properties and device architectures, it is possible to harness the advantages of both filamentary and interfacial switching, paving the way for reliable and efficient memristive devices suitable for next-generation memory and neuromorphic computing applications.

1.4 Thesis Outline

This thesis is organized into six chapters, each contributing to a comprehensive understanding of halide perovskite single crystals for next-generation resistive memory and optoelectronic devices.

Chapter 1: Introduction

This chapter provides the context and motivation for the thesis. It begins by outlining the limitations of conventional computing paradigm in terms of power consumption, performance, and environmental impact. The emerging field of neuromorphic computing is introduced as a promising alternative, and resistive switching devices (memristors) are presented as key enablers of this new paradigm. Within this framework, halide perovskites are proposed as versatile materials owing to their unique combination of ionic–electronic transport, tunable optoelectronic properties, and low-cost solution processability. Special attention is devoted to SC perovskites, which offer superior structural and electrical properties compared to their PC counterparts. The chapter concludes with a statement of objectives and the scope of the thesis.

Chapter 2: Methods; Synthesis, Device Fabrication, and Optoelectronic and Structural Characterization

This chapter outlines the experimental methodologies developed and employed throughout the thesis. It covers the synthesis of bulk and thin perovskite single crystals using (ITC and CITC, respectively. The fabrication protocols for SC-based memristor devices are described in detail, along with the integration of graphite electrodes for contact formation. Structural, morphological, and optoelectronic characterization techniques, such as X-ray diffraction (XRD), scanning electron microscopy (SEM), PL, time-resolved PL, micro-PL mapping, and impedance spectroscopy, are presented as a practical toolbox for assessing material quality and device performance.

Chapter 3: Bosting Photoluminescence in $MAPbBr_3$ Single Crystals through Laser-Based Surface Modification

This chapter investigates the laser passivation of $MAPbBr_3$ bulk SCs through continuous-wave laser treatment. A robust increase in photoluminescence (≈100×) and a measurable bandgap shift (≈75 meV) are observed, attributed to a surface restructuring process resulting in the formation of a $PbBr_2$-rich layer. Structural and chemical analyses (XRD, XPS) combined with optical techniques (PL, TRPL, PLE) confirm a modified surface region that passivates nonradiative defects. These findings reveal a light-induced mechanism for enhancing crystal stability and emission properties through surface composition engineering.

Chapter 4: Perovskite Thin Single Crystal for a High Performance and Long Endurance Memristors

This chapter presents the design and performance of memristive devices based on thin single crystal $MAPbBr_3$, synthesized via the CITC method. The devices exhibit high LRS/HRS ratios (up to 50), excellent retention (>10^4 s), and stable switching behavior over 10^3 cycles. The use of impedance spectroscopy enables real-time tracking of the electroforming process and confirms the role of ion migration in the switching mechanism. These results demonstrate the feasibility of high-performance single crystal memristors for neuromorphic computing.

Chapter 5: Compositional Engineering of Monocrystalline Metal Halide Perovskite Memristors for Multistate Non-Volatile Operation

As a continuation of the previous chapter, this section introduces halide mixing as a strategy to achieve multistate memory behavior in TSC perovskite memristors. Devices based on $MAPb(Br_{0.9}I_{0.1})_3$ show six distinct resistance levels, while those based on $MAPb(Br_{0.8}Cl_{0.2})_3$ achieve three. Comparative analysis with PC analogs highlights the critical role of defect density in enabling stable and distinguishable resistive states. The chapter concludes that multistate ReRAM functionality can be achieved through controlled morphological and compositional engineering.

Chapter 6: Conclusions

The final chapter synthesizes the key findings from all previous chapters. It reflects on the role of laser-assisted surface engineering, thin SC device integration, and halide composition tuning in enhancing optoelectronic and memristive performance, respectively. The work collectively demonstrates the versatility and potential of SC-MHPs as active layers in high-density, low-power, and multistate memory devices. Future directions for long-term stability, and hybrid neuromorphic architectures are briefly discussed.

1.5 Objectives of the Thesis

This doctoral thesis is structured around two primary research objectives, each addressing distinct challenges in the field of halide perovskite-based devices, with a particular focus on their application in resistive memory technologies and optoelectronic performance optimization.

1. Surface Engineering of Bulk Single Crystal Perovskites for Enhanced Optoelectronic Performance.

The first objective is to investigate novel laser-induced passivation strategies for improving the optoelectronic response of bulk $MAPbBr_3$ SCs. This involves understanding the structural, chemical, and electronic modifications induced by continuous-wave laser irradiation and correlating them with enhancements in PL efficiency and spectral properties. The goal is to elucidate the mechanisms behind surface restructuring, particularly the formation of a dual-layer system consisting of $PbBr_2$ and a bandgap-widened $MAPbBr_3$ interface, and to validate its potential for defect passivation and high PL emission.

2. Development and Functional Characterization of Thin Single Crystal Memristors.

The second objective focuses on the fabrication, and fundamental understanding of TSC perovskite memristive devices. Using CITC, this work aims to preserve the structural advantages of single crystals while enabling high performance with simply architecture devices. Electrical performance is assessed through cyclic voltammetry, endurance and retention testing, and impedance spectroscopy. The study also examines the influence of crystal morphology on switching properties by comparing the performance of TSC memristor devices versus PC ones.

3. Compositional Engineering for Multistate Operation in ReRAM Devices.

As an extension of the second objective, the thesis explores the effect of halide composition on the memristive behavior of TSC perovskites. Mixed-halide systems, $MAPb(Br_{0.9}I_{0.1})_3$ and $MAPb(Br_{0.8}Cl_{0.2})_3$, are synthesized and studied in its memristor properties, identifying the origin of multilevel resistance states. This objective includes a comparative analysis of PC and TSC devices to correlate defect landscape with electrical performance and memristive properties. The ultimate aim is to establish design principles for high-density, low-power memory applications using halide perovskite materials.

Through these interconnected research goals, the thesis contributes to both the fundamental understanding and practical realization of stable, tunable, and efficient perovskite-based devices for neuromorphic computing and beyond.

Chapter 2

Methods and Characterization Techniques

This chapter outlines the main fabrication strategies and characterization methods used in the development and analysis of perovskite-based memristive devices throughout this Thesis. Rather than presenting an exhaustive review, the goal is to provide a focused and practical guide to the experimental procedures, highlighting the key techniques applied for crystal growth, device integration, and the optoelectronic, electrical and structural evaluation of perovskite materials.

2.1 Device Fabrication

2.1.1 Inverse Temperature Crystallization Method

This thesis focuses on the of the fabrication memristor devices based on single crystals perovskites. As mentioned above, to synthetise single crystal perovskites, several methods have been developed to optimize crystal quality and scalability, including solution-based techniques as ITC[112], CITC method[114], AVC[110] or TCC[108]. Here, ITC method is chosen due to the simplicity, relatively low-time consuming, and the ability to obtain reproducible high-quality crystals. This method relies on the unusual property of certain perovskite precursors, in specific solvents, whose solubility decreases with increasing temperature, enabling controlled crystal nucleation and growth. When the solubility reaches a saturation point due to temperature increasing, the solution collapses, forming a nucleus of perovskite SCs which keeps growing while temperature increases, Figure 16a. Nevertheless, while this method offers high-quality SCs for fundamental studies, their undesirable volume/thickness ratio impossibilities their use to fabricate devices as solar cells or memristors[147].

2.1.2 Confined Inverse Temperature Crystallization Method

However, it is possible obtain thicker single crystal by confining the solution during ITC method. In this CITC method, the crystallization process is confined within a restricted space, such as microchannels, small capillaries, or sandwiched with substrates, to achieve better control over crystal size, morphology, and dimensionality, Figure 16b. This technique is particularly useful for growing perovskite crystals with specific geometries and thickness suitable for device fabrication, such as thin films or microplates, by addressing the volume-to-thickness limitations of conventional ITC.

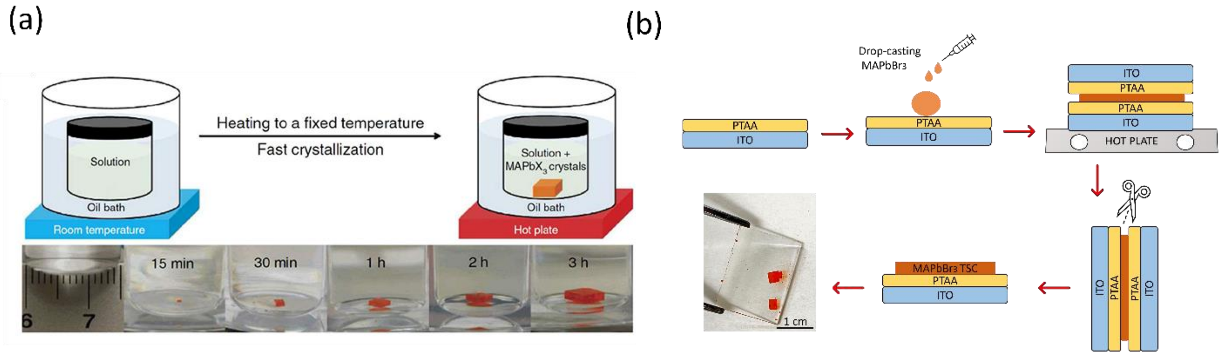

Figure 16. (a) ITC process[112], and (b) CITC scheme.

In this thesis, ITC method is used in chapter 3 to growth $MAPbBr_3$ SCs where it is demonstrated an improvement of optoelectronic properties via surface laser passivation. In chapter 4, CITC method is used to fabricate $MAPbBr_3$ TSC memristors, and determine their memristive properties. Finally, in chapter 5, CITC method is used to fabricate $MAPbCl_3$, $MAPbBr_3$, $MAPbI_3$, $MAPb(Br_{0.8}Cl_{0.2})_3$ and $MAPb(Br_{0.9}I_{0.1})_3$ TSC memristor devices.

2.2 Optoelectronic and Structural Characterization

2.2.1 I-V Response

I-V measurement is a fundamental technique for investigating the electronic transport behavior of a wide variety of materials and device structures. This measurement allows the extraction of critical parameters such as electrical conductivity, contact resistance, charge injection barriers, and nonlinear transport characteristics. In this thesis, a Gamry inter-face 1010E potentiostate is mainly used to characterize memristor devices.

Memristors operate based on the electrical response to different stimulus as voltage. To determine the set and reset voltages of the memristor devices, an I-V curve is measured. The endurance response is evaluated by applying a sequence of voltage pulses as follows: (i) set voltage, (ii) read voltage, (iii) reset voltage, and (iv) read voltage. This sequence is repeated until the device fails and no distinct states can be differentiated. To determine the retention time, chronoamperometry is performed as follows: the device is first set to the HRS, and the current is monitored at the read voltage until it collapses or becomes unstable. Subsequently, the device is set to the LRS, and the current is measured at the read voltage until it becomes unstable or decreases dramatically.

2.2.2 Impedance Spectroscopy (IS)

Impedance spectroscopy is an analytical technique used to study the electrical and electrochemical properties of perovskite materials and devices, such as solar cells, memristors, and LEDs. This method involves applying an alternating current (AC) voltage to a device and measuring the resulting current over a range of frequencies. The response provides insight into charge transport, recombination dynamics, ionic migration, and interfacial effects in perovskite systems.

The core principle of IS involves applying a small sinusoidal voltage (typically 5–10 mV) over a broad range of frequencies, from 1 MHz down to 0.1 Hz, and measuring the corresponding current response. The ratio of voltage to current yields the complex impedance $Z(\omega)=Z'+jZ''$, where Z and Z'' are the real and imaginary components, respectively.

As mentioned above, perovskites are known for their mixed ionic-electronic conductivity, a property that significantly influences their electrical performance. IS is uniquely suited to studying this dual behavior. At high frequencies, the response is typically dominated by electronic transport within the bulk of the perovskite layer. This includes the movement of charge carriers such as electrons and holes through the crystal lattice. The bulk resistance and dielectric properties of the material can be extracted from this frequency range. In contrast, low-frequency responses are more indicative of ionic processes. Mobile ions, such as halide vacancies (e.g., iodine or bromine) or organic cation migrations (e.g., methylammonium), contribute to polarization effects within the device. IS can detect these slow processes as they manifest in increased impedance or additional arcs in the Nyquist plot.

The interpretation of IS data requires equivalent circuit modeling to assign physical meaning to the observed features. Commonly used models for perovskite devices include combinations of resistors, capacitors, inductor, and constant phase elements to represent bulk transport, interfacial charge transfer, and ionic migration[148].

In this thesis, for the first time, the electroforming process is monitored in situ by IS. The robustness of the TSC memristors, allow a stable impedance spectroscopy measurement during electroforming process, insight about which ions or species are involved in the electroforming process.

2.2.3 Steady-State Photoluminescence (PL) Spectroscopy

Steady-state photoluminescence spectroscopy is a non-destructive optical technique widely used to probe the electronic and optical properties of semiconductors. By analyzing the light emitted from a material upon photoexcitation, PL measurements provide direct insight into bandgap energy, and material homogeneity.

In a typical PL setup, the sample is illuminated with monochromatic light of energy higher than the bandgap, promoting electrons from the valence to the conduction band. The radiative recombination of photoexcited carriers results in the emission of photons, whose spectral distribution is collected and analyzed to extract fundamental information about the electronic transitions within the material.

The experimental setup for steady-state PL measurements typically includes the following components:

1. Excitation Source: A continuous-wave (CW) laser or filtered xenon/LED lamp is used to generate a stable excitation beam at a selected wavelength. The excitation energy is chosen to ensure sufficient absorption while avoiding material degradation or nonlinear effects.
2. Optical Path and Focusing System: Lenses or optical fibers guide and focus the excitation light onto the sample surface. In some cases, neutral density filters are introduced to adjust the excitation intensity.
3. Sample Holder and Environmental Control: The sample is mounted on a stage, which may include temperature or atmosphere control depending on the requirements of the experiment. This allows for the study of PL under ambient, vacuum, or controlled gas environments.

4. Detection System: Emitted light is collected perpendicularly (or at a specified angle) to the excitation path and directed into a spectrometer equipped with a CCD or photodiode array detector. The resulting PL spectrum is plotted as intensity versus wavelength or energy.

PL spectra are typically used to estimate the optical bandgap from the peak emission energy and to evaluate the presence of trap states via sub-bandgap emission features. In high-quality crystalline materials, sharp and intense emission peaks with narrow full width at half maximum (FWHM) indicate low defect density and efficient radiative recombination. Conversely, broad or red-shifted emissions often reflect non-radiative losses, disorder, or interface effects.

Steady-state PL is particularly useful for comparative studies of material quality, defect passivation strategies, and compositional tuning in thin films and bulk crystals.

2.2.4 Time Resolved Photoluminescence (TRPL)

Time-resolved photoluminescence measurements, focus on the temporal dynamics of excited-state decay processes. Upon excitation with a short, high-intensity pulse, electrons are promoted to higher energy states. As these carriers relax back to the ground state, they emit photons with characteristic time-dependent intensity profiles.

A typical TRPL setup consists of:

1. Pulsed Excitation Source: Ultrafast lasers, capable of generating brief and intense light pulses, are used to excite the sample. The excitation wavelength is selected to match the material’s absorption edge, ensuring effective photoexcitation.
2. Sample Mounting and Alignment: Samples are positioned on adjustable holders that allow precise spatial alignment to optimize the excitation and collection geometry.
3. Time-Correlated Single Photon Counting (TCSPC) System: The emitted photons are detected using a high-speed TCSPC setup, which records the arrival time of individual photons relative to the excitation pulse. By accumulating photon counts over many excitation cycles, a decay histogram is built to characterize the luminescence lifetime.

4. Spectral Filtering: A monochromator or spectrometer is placed between the sample and the detector to isolate specific emission wavelengths. This allows for wavelength-resolved lifetime measurements, providing insight into different emissive states and recombination pathways.

The resulting decay curves, which typically follow mono- or multi-exponential kinetics, reveal the contributions of radiative and non-radiative processes, including trap-mediated recombination and energy transfer mechanisms.

2.2.5 X-ray Photoelectron Spectroscopy (XPS)

X-ray photoelectron spectroscopy is a powerful surface-sensitive technique used to determine the elemental composition, chemical environment, and electronic structure of materials within the top few nanometers of the surface. The method is based on the photoelectric effect: when a material is irradiated with monochromatic X-rays, electrons from core atomic orbitals are ejected. By measuring their kinetic energy and knowing the energy of the incident photons, the binding energy of each electron can be calculated, this value is characteristic of specific elements and their oxidation states.

An XPS spectrum displays the number of detected photoelectrons as a function of binding energy, where sharp peaks correspond to different elements and chemical states present at the surface. Given that only electrons emitted from the outermost ~1–10 nm escape without significant energy loss, the technique is particularly well suited for analyzing surface chemistry, passivation layers, and thin films.

A typical XPS system includes the following components:

1. X-ray Source: Most commonly, aluminum Kα (1486.6 eV) or magnesium Kα (1253.6 eV) sources are used to generate the incident X-rays.
2. Ultra-High Vacuum (UHV) Chamber: All measurements are performed under ultra-high vacuum conditions to prevent electron scattering by ambient gas molecules, thereby ensuring accurate energy detection.

3. Electron Energy Analyzer: A hemispherical analyzer measures the kinetic energy of the emitted electrons with high precision. This step is essential for resolving closely spaced energy levels and identifying subtle chemical shifts.
4. Detector and Processing Unit: The signal is captured by a detector and analyzed by dedicated software, which allows for peak deconvolution, quantitative elemental analysis, and assessment of chemical bonding environments.

2.2.6 X-ray Diffraction (XRD)

X-ray diffraction is a non-destructive analytical method used to probe the crystallographic structure, phase identity, and lattice orientation of crystalline materials. The technique exploits the diffraction of X-rays by periodic atomic planes within the crystal, following Bragg's law: $n\lambda=2d\sin\theta n$

where λ is the X-ray wavelength, d is the interplanar spacing, and θ is the incident angle. Constructive interference occurs when this condition is met, producing characteristic peaks in the diffraction pattern.

The intensity of diffracted beams is plotted as a function of 2θ, allowing researchers to identify crystal phases and estimate structural parameters such as lattice constants, grain size, and degree of crystallinity.

A standard XRD setup includes:

1. X-ray Source: A Cu Kα source emitting X-rays at 1.54 Å is typically used to irradiate the sample.
2. Goniometer System:
    - *Sample Rotation Mode*: The sample is rotated to vary the incidence angle θ, while the detector may remain stationary or track the corresponding 2θ position.
    - *θ–2θ Configuration*: The sample remains fixed while both the X-ray source and detector are moved in synchrony to satisfy the θ–2θ condition. This arrangement is widely used in thin-film and single-crystal characterization due to its simplified alignment and reproducibility.

3. Detector: The intensity of diffracted X-rays is recorded at various angles to generate a pattern reflecting the atomic arrangement within the material.

X-ray diffraction is widely applied in materials science for phase identification, crystallinity assessment, and structural refinement. It is indispensable for verifying the formation of target crystal structures, detecting secondary phases, and quantifying preferential orientation in thin films. In the context of halide perovskites and related semiconductors, XRD also enables monitoring of degradation processes, phase transitions, and strain effects, providing crucial insights into the stability and structural evolution of the material under operational conditions.

2.2.7 Scanning Electron Microscopy (SEM)

Scanning electron microscopy is a widely utilized technique for surface characterization, offering high-resolution imaging of materials at the micro- to nanoscale. Unlike optical microscopy, which is limited by the wavelength of light, SEM employs a focused beam of high-energy electrons to probe the surface topography and composition of solid specimens.

In SEM operation, the electron beam is raster-scanned across the sample surface. As the electrons interact with atoms in the specimen, various types of signals are generated, most notably secondary electrons (SE) and backscattered electrons (BSE). These emissions are collected by dedicated detectors to form detailed images that reveal the sample's morphology, texture, and compositional contrast.

The primary components of a SEM system include:

1. Electron Source: The electron beam is generated using an electron gun, which may be based on a thermionic emitter (e.g., tungsten filament or LaB_6) or a field emission source, the latter providing higher brightness and resolution. Typical accelerating voltages range from 1 to 30 kV, selected according to the resolution required and the sample's sensitivity.
2. Electron Optics: A series of electromagnetic lenses and apertures focus and shape the beam, enabling precise control of the spot size and beam current.
3. Sample Chamber and Stage: The specimen is placed on a motorized stage within a high-vacuum chamber to minimize electron scattering by gas molecules. The stage allows for adjustment in multiple axes (x, y, z, tilt, and rotation) to optimize imaging conditions.

4. Detectors:
   - *Secondary Electron Detector*: Captures low-energy electrons emitted from the near-surface region, producing high-contrast images that highlight surface features.
   - *Backscattered Electron Detector*: Records electrons reflected from deeper within the sample, providing contrast based on atomic number, useful for distinguishing different elements.
5. Vacuum System: Essential to maintain the free path of electrons, the vacuum environment reduces collisions with air molecules and protects the electron optics from contamination.

SEM is particularly valuable for assessing grain size, surface roughness, fracture morphology, and particle dispersion in a wide range of materials. Its versatility, combined with rapid imaging and high depth of field, makes it a foundational tool in materials characterization.

Chapter 3

Boosting Photoluminescence in $MAPbBr_3$ Single Crystals through Laser-Based Surface Modification

Chapter 3 details all the results from the study of a novel-contactless method to passivate $MAPbBr_3$ SCs, enhancing PL emission two order of magnitude, with an increasing of the band gap of approximately 75 mV respect to untreated crystals. The findings presented throughout this chapter are derived from and correspond to those reported in the peer-reviewed published article; ACS Photonics 2023, 10, 12, 4151–4159

Everything detailed in this chapter aligns with the established data and conclusions within the original publication

Abstract

SC-MHPs have garnered considerable attention for their potential to outperform PC films in optoelectronic applications. However, surface recombination remains a major limitation due to nonradiative losses. Here, we demonstrate that exposing $MAPbBr_3$ SCs to CW blue laser light induces surface modification, resulting in the formation of a $PbBr_2$ capping layer and a subsurface perovskite region with an increased band gap of approximately 75 meV. This process enhances the PL by nearly two orders of magnitude. We propose that tensile strain caused by partial decomposition of $CH_3NH_3^+$ under laser irradiation and oxygen atmosphere distorts the lattice, leading to band gap broadening. The concurrent formation of formic acid and methylamine contributes to surface passivation and protects against environmental degradation.

3.1 Introduction

As above mentioned, Iin the last ten years, MHPs have emerged as key materials for next-generation optoelectronic technologies due to their unique semiconducting characteristics.[149], [150], [151] These compounds offer advantages such as cost-effective and low-temperature processing, making them attractive for devices including photodetectors[152], lasers[153], LEDs[154], and solar cells[155].

The outstanding optoelectronic properties of MHPs, such as high absorption coefficients, long carrier diffusion lengths, and low fabrication costs[156], [157], [158], [159] have positioned these materials at the forefront of photovoltaic development. Recent advancements have pushed the PCE of perovskite solar cells beyond 26%[68], achieved through careful optimization of crystal quality, composition, interfaces, and device architecture[160], [161]. Most developments to date have relied on PC thin films, where increasing grain size and enhancing crystal quality have been pivotal[160], [162].

Although defects in metal halide perovskites are frequently described as benign[163], grain boundaries can nonetheless serve as initiation points for material degradation[164], [165], [166]. Consequently, the traps that form spontaneously in these regions often function as nonradiative recombination centers. Since nonradiative recombination accounts for the majority of energy losses in photovoltaic devices, the open-circuit voltage (V_{OC}) typically falls below its theoretical maximum[167], [168].

By contrast, SC-MHP obtained through chemical synthesis[169], [170] exhibit exceptionally low trap densities in the bulk, along with superior charge mobility and extended carrier lifetimes[84], [91]. While their physical dimensions may limit direct integration into devices, recent demonstrations have achieved power conversion efficiencies exceeding 22% in SC-PSCs[100], [171]. Owing to the absence of grain boundaries and the presence of continuous monocrystalline domains, SCs provide an almost ideal platform for next-generation MHP-based optoelectronics. Nonetheless, despite their promising performance, further insight into surface-related carrier dynamics remains essential[172], [173].

In recent years, considerable attention has been devoted to mitigating nonradiative recombination at MHP interfaces using chemical passivation agents. However, this strategy remains inefficient, as many of these additives are large organic molecules that tend to lower electrical conductivity and limit device integration[174], [175]. An alternative approach employing ultraviolet (UV) laser treatment has proven effective in enhancing the efficiency of polycrystalline thin-film solar cells, though the fundamental mechanism behind this improvement remains unclear[176]. Another promising route involves the use of inorganic compounds inherently related to the MHP absorber, such as PbX_2 (X = Cl, Br, I), which has been shown to passivate grain boundaries in lead halide perovskites and improve the V_{OC} of perovskite solar cells (PSCs)[177], [178], [179], [180], [181].

Currently, PbX_2 formation within the MHP layer is typically achieved through thermal annealing, though this process carries the risk of inducing thermal degradation[182]. A different method consists of incorporating an excess amount of PbX_2 directly into the precursor formulation[183], [184]. Nevertheless, both approaches lack the ability to precisely control the spatial distribution of PbX_2, which is essential to ensure its localization at the perovskite crystal boundaries rather than within the bulk of the material. A more advanced technique has recently been introduced[185], which relies on low-temperature humidity modulation to direct the accumulation of PbI_2 specifically at the grain boundaries on the surface of MHP films. This process results in the formation of a self-organized type-I band alignment at the PbI_2/MHP interface, leading to a significant enhancement in V_{OC} from 1.07 V to 1.17 V and an increase in photovoltaic power conversion efficiency from 20.2% to 22.4%. Despite these promising advances, the physical phenomena occurring at MHP/PbX_2 interfaces remain poorly understood[186], [187], [188], [189].

In this chapter, we introduce a strategy to suppress surface-related nonradiative losses in $MAPbBr_3$ SCs via CW blue laser irradiation. Using both macro- and micro-photoluminescence (PL and μPL) techniques, complemented by structural characterization through X-ray diffraction and X-ray photoelectron spectroscopy (XPS), we demonstrate that CW blue laser exposure leads to an enhancement of approximately two orders of magnitude in PL intensity and a band gap widening of around 75 meV in the treated $MAPbBr_3$ (where MA = CH_3NH_3) crystals. Following laser treatment, a thin white layer appears on the crystal surface, which is identified as crystalline $PbBr_2$. Beneath this layer, a modified $MAPbBr_3$ phase with an enlarged band gap and improved photophysical characteristics is formed. In the following discussion, we explore the underlying mechanisms that may explain these observations.

3.2 Experimental

Synthesis of Single Crystals. Lead(II) bromide ($PbBr_2$, 98% purity, Fisher Chemical), methylammonium bromide (MABr, 98% purity, Ossila), and dimethylformamide (DMF, 99.8% purity, Sigma-Aldrich) were used as starting materials.

$PbBr_2$ and MABr were each dissolved in DMF to prepare a 1 M solution. The mixture was stirred at room temperature under ambient conditions until the precursors were fully dissolved. The resulting solution was then filtered using 0.2 μm pore-size filter to eliminate any particulates. After filtration, the solution was transferred into a sealed 20 cm^3 glass vial and placed in an oil bath. The temperature of the bath was initially raised at a rate of 20 °C/h until reaching 60 °C. Subsequently, the heating rate was reduced to 10 °C/h to bring the solution to 80 °C. Once this temperature was achieved, it was maintained for 24 hours. This ITC protocol resulted in the formation of $MAPbBr_3$ SCs with consistent size and morphology.

Optoelectronic measurements were carried out using an Edinburgh Instruments FLS 1000 fluorimeter equipped with a double-grating Czerny–Turner monochromator. The spectrally resolved photoluminescence signal was directed into a high-speed photomultiplier tube (PMT) housed in a cooled enclosure. This setup was employed for both steady-state PL and time-resolved photoluminescence experiments. For TRPL, excitation was provided by a 405 nm pulsed laser with a pulse width of 1 ns. The resulting PMT output was processed through a photon-counting system, yielding an instrument response function (IRF) of approximately 200 ps.

SEM images were acquired using a HITACHI S-4800 microscope (Tokyo, Japan) operated at 2 kV.

XPS measurements were performed at the ALOISA multipurpose beamline of the Elettra synchrotron facility in Trieste, employing a tunable and monochromatized photon source with a beam spot size of 0.1 mm × 0.3 mm. The photon energy was adjustable in the range of 130 to 2800 eV. Spectra were recorded using a custom-built hemispherical analyzer with a mean radius of 66 mm, coupled to a two-dimensional delay-line detector from Elettra. For the experiments reported in this study, a photon energy of 515 eV was selected, providing an overall spectral resolution of 150 meV (full width at half maximum, FWHM). Data acquisition was conducted in normal emission geometry, with the samples positioned at a grazing angle of 4° relative to the incident beam, under near p-polarized conditions. The sample temperature was controlled and could be varied from 150 °C down to room temperature. The binding energy (BE) scale was calibrated using the C 1s peak of adventitious carbon, fixed at 284.8 eV. Spectral analysis was carried out using a custom data processing library developed in Igor Pro, following subtraction of the Shirley background. Multicomponent peak fitting was performed using Voigt functions to account for instrumental and intrinsic broadening.

Atomic force microscopy (AFM) and Kelvin probe force microscopy (KPFM) measurements were conducted using a scanning probe microscope (AISt-NT) equipped with silicon tips coated with platinum. The cantilevers had an elastic constant of 3 N/m, and the scan rate was fixed at 0.5 Hz. The spatial resolution of the system was approximately 20 nm, while the electrical resolution for potential measurements was around 5 mV. Illumination during measurements was provided by a 405 nm laser diode.

The crystalline structure of the samples was examined by X-ray diffraction (XRD) using a Bruker D8 Advance diffractometer equipped with a Cu Kα radiation source (λ = 1.5418 Å). Measurements were performed in grazing incidence mode with an incident angle of 1°, and data were collected at a scan rate of 5°/min over a 2θ range spanning from 12° to 50°.

Confocal micro-photoluminescence (μPL) spectroscopy was performed with the samples mounted on the cold finger of a vibration-free closed-cycle cryostat (AttoDRY800, Attocube AG). Excitation and collection of the PL signal were achieved using a 50× long working distance microscope objective with a numerical aperture (NA) of 0.42, positioned outside the cryostat. The emitted photoluminescence was filtered using a long-pass filter, then dispersed through a double-grating spectrograph with a 0.3 m focal length (Acton SP-300i, Princeton Instruments), and finally detected by a thermoelectrically cooled silicon CCD camera (Newton EMCCD, ANDOR) to acquire the μPL spectra.

3.3 Results and discussion

$MAPbBr_3$ SCs were prepared via ITC technique, which is extensively documented as one of the most straightforward and effective methods for producing high-quality crystals with minimal trap-state densities[84], [190]. For the present study, we selected crystals with lateral dimensions of approximately 5 mm × 4 mm and a thickness close to 1 mm (Figure 17a).

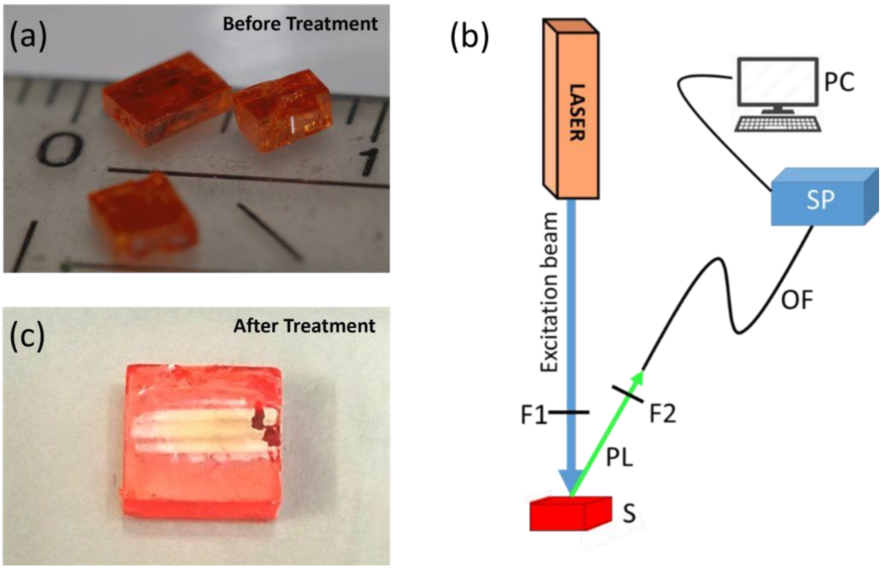

Figure 17. Optical images of (a) a pristine and (c) a laser over-treated $MAPbBr_3$ SC. (b) Schematic diagram of the experimental setup: S, sample; PL, photoluminescence; F1 and F2, optical filters used to adjust the excitation power and block scattered excitation light, respectively; OF, optical fiber; SP, spectrograph; PC, computer.

The PL spectra were recorded in situ using the same 445 nm CW laser beam employed for excitation. A schematic representation of the experimental configuration for laser processing of $MAPbBr_3$ SC is provided in Figure 17b. During the entire procedure, both the sample and the laser beam remained fixed. The laser treatment protocol consisted of three distinct stages: Stage I, “stabilization”, which involved illumination at a fluence of 0.15 W/cm^2 for 5 minutes; Stage II, “treatment”, where the excitation power density was increased to 1.5 W/cm^2 and maintained for 10–15 minutes; and Stage III, “post-treatment”, in which the power density was reduced back to 0.15 W/cm^2 for an additional 10 minutes. Following the treatment, a white film visibly formed on the crystal surface, becoming increasingly prominent with extended exposure durations, as illustrated in Figure 17c.

Figure 18 compiles the evolution of PL intensity and spectral changes occurring during the laser treatment. To describe the changes in PL intensity, the time-dependent PL emission at 540 nm is shown in Figure 18a, a wavelength chosen because it remains close to the PL peak maximum throughout the entire process (as seen in Figure 18b). For clarity in presentation, the PL data corresponding to Stage II in Figure 18a have been scaled down by a factor of 10 to compensate for the tenfold increase in excitation power. As such, the normalized PL intensity depicted in Figure 18a can be approximately interpreted as a relative PLQY.

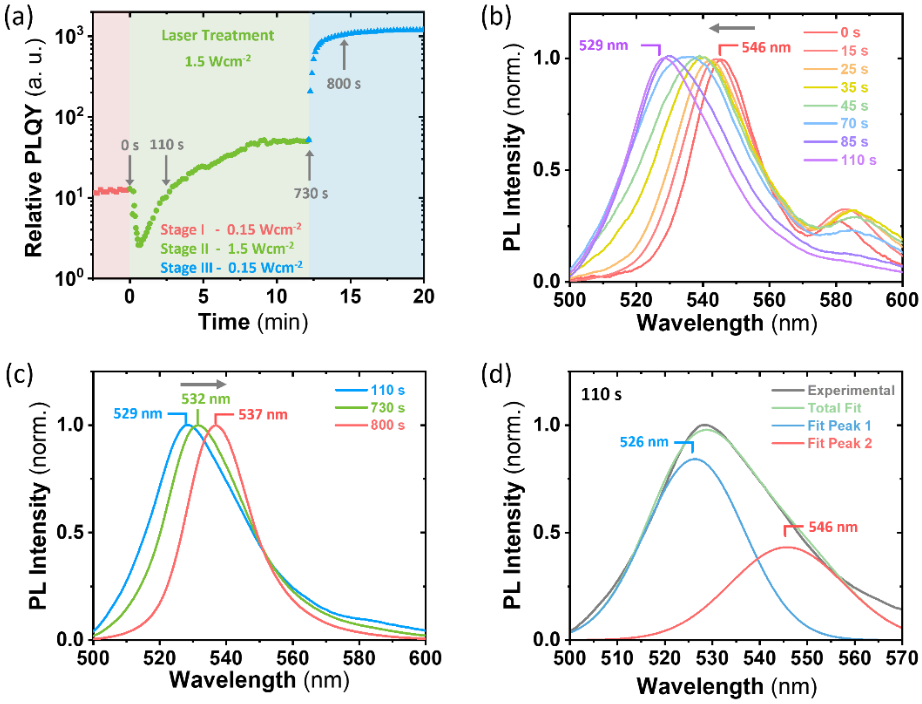

Figure 18. (a) Temporal evolution of the normalized photoluminescence (PL) intensity of $MAPbBr_3$ SC monitored in situ at 540 nm under continuous illumination with a 445 nm CW laser: stage I (red line) corresponds to an excitation fluence of 0.15 W/cm^2, stage II (green line) to 1.5 W/cm^2, and stage III (blue line) to 0.15 W/cm^2; (b) normalized PL spectra acquired in situ at different time points during stage II of the laser treatment; (c) normalized PL spectra recorded with varying delays from the start of stage II; (d) spectral deconvolution of the PL signal measured 110 s after the initiation of stage II, revealing two Gaussian components centered at 526 nm and 546 nm.

The most significant alterations in the in situ PL spectra take place within the first 120 seconds of Stage II, under an excitation power density of 1.5 W/cm^2 (Figure 18b). During this initial period, the normalized PL intensity undergoes a rapid decrease, followed by a gradual recovery approaching the original emission level (Figure 18a). Simultaneously, the PL peak shifts toward higher photon energies, transitioning from 546 nm to 529 nm, accompanied by a broadening of the emission band (Figure 18b). After the first two minutes, a redshift of the PL maximum is observed, reaching approximately 532 nm, along with a narrowing of the spectral width (Figure 18c). At the same time, the normalized PL increases by nearly a factor of five (Figure 18a).

In the final phase, Stage III ("post-treatment"), the PL spectrum continues to redshift and becomes further narrowed, while the normalized PL intensity rises by roughly an order of magnitude. Overall, the cumulative PL enhancement after the entire laser treatment reaches approximately two orders of magnitude. It is noteworthy that when Stage II is conducted at a reduced fluence of 0.75 W/cm^2, no substantial improvement in PL intensity is detected (Figure 19). This observation suggests that a threshold power density near 1.5 W/cm^2 is required to effectively initiate the passivation process in the SCs.

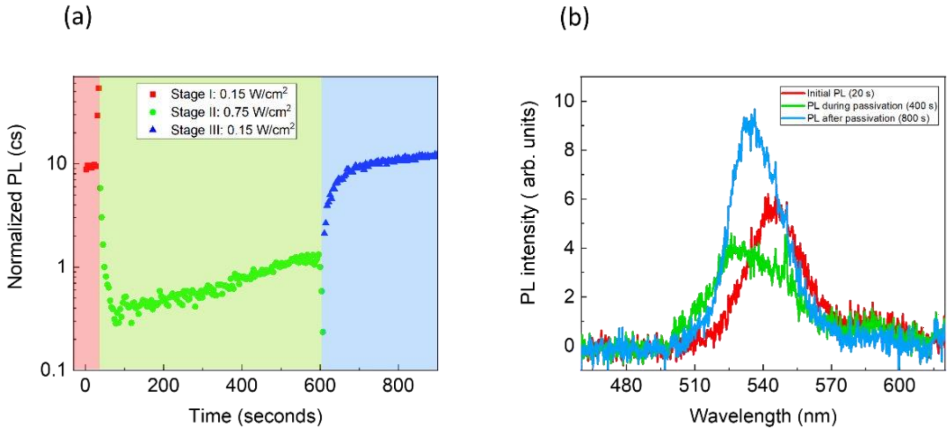

Figure 19. (a) Time evolution of the normalized PL intensity of a $MAPbBr_3$ SC measured in situ at 540 nm under 445 nm CW laser illumination: Stage I (red symbols) excitation fluence of 0.15 W/cm^2; Stage II (green symbols) excitation fluence of 0.75 W/cm^2; Stage III (blue symbols), excitation fluence of 0.15 W/cm^2. (b) In situ PL spectra recorded at different time intervals following the onset of Stage II laser treatment.

To gain deeper insight into the mechanisms at play during laser treatment, it is crucial to examine the evolution of the in situ PL spectra. We propose that the initial broadening and blue shift observed within the first two minutes of illumination arise from the emergence of an additional PL band, shifted toward shorter wavelengths. Our analysis reveals that the recorded spectra can be accurately represented as the superposition of two Gaussian components centered around 546 nm and 526 nm, respectively (Figure 18d). Importantly, the relative intensity of the 526 nm component increases steadily as the treatment progresses, as clearly illustrated in figure 18d and Figure 20.

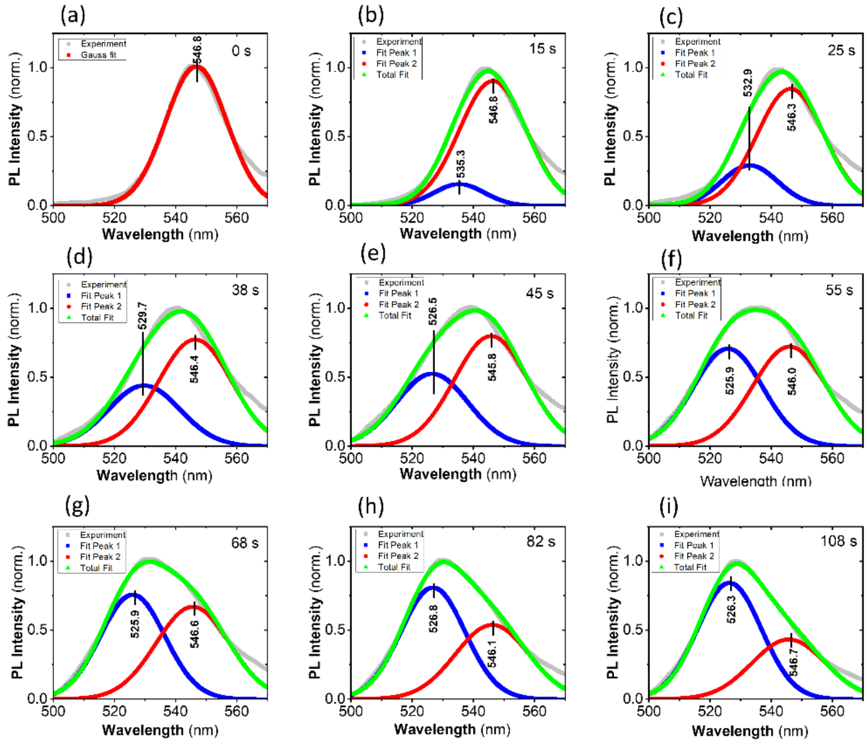

Figure 20. Deconvolution of the PL spectra acquired within the first 0–110 s of high-intensity laser irradiation, fitted as the sum of two Gaussian components.

It is important to emphasize that the observed modifications in the PL spectra cannot be attributed to thermal effects induced by laser irradiation. To assess the potential influence of temperature on the PL enhancement, we performed a thermal annealing experiment at 120 °C for 20 minutes. Contrary to the laser treatment results, this process led to a reduction rather than an increase in PL intensity (see Figure 21).

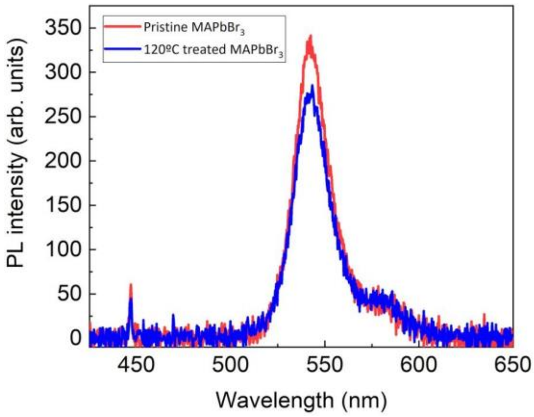

Figure 21. Photoluminescence (PL) spectra of a MAPbBr$_3$ SC recorded before (red line) and after (blue line) thermal annealing at 120 °C for 20 minutes.

Additionally, the potential contribution of CW laser-induced heating was previously investigated[189], where it was shown that in MAPbI$_3$ SCs, materials with similar blue-light absorption characteristics, a laser fluence as high as 10 W/cm^2 (six times greater than used in our study) resulted in a negligible temperature increase of less than 0.5 °C.

Subsequently, we investigated the PL behavior of MAPbBr$_3$ SCs before and after laser treatment using a commercial fluorimeter under ex situ measurement conditions. The results, comprising PL spectra, PLE spectra, and PL decay profiles, are shown in Figure 22. Notably, both the PL and PLE spectra exhibit a clear blue shift following the laser exposure (Figure 22a).

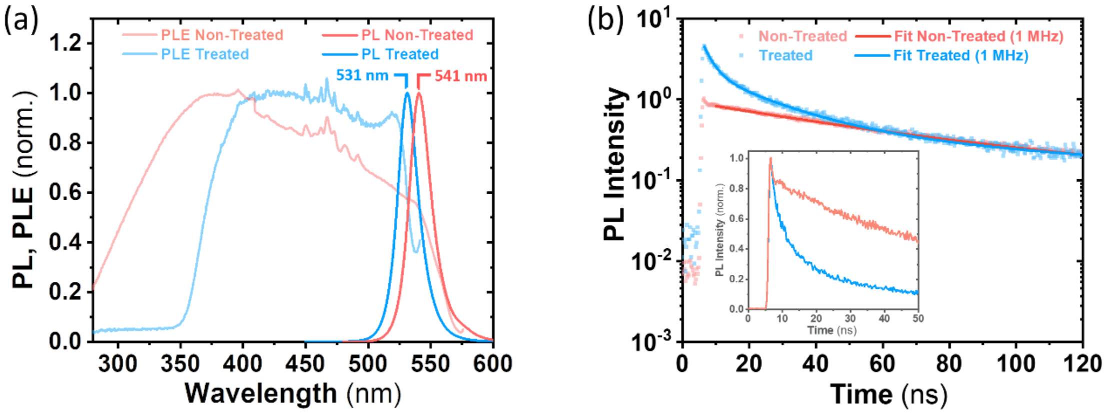

Figure 22. (a) PL and PLE spectra for MAPbBr$_3$ SC before (red) and after (blue) laser treatment. (b) PL decay kinetic for treated (blue) and untreated (red) MAPbBr$_3$ SC, normalized to the long-

lived component. The inset displays the same decay profiles on a linear scale, normalized to their respective peak intensities.

These observations indicate that the observed blue shift in emission is not the result of reabsorption effects but rather stems from a widening of the $MAPbBr_3$ band gap. The PL decay kinetic of the untreated $MAPbBr_3$ SCs features a low-intensity short-lived component with a decay time of approximately 1–2 ns, followed by a longer-lived component with a decay time close to 800 ns (Figure 22b). In laser-treated samples, a two-component decay is also observed, but with a significantly more intense short-lived component. Notably, the lifetime of the long-lived component remains essentially unchanged at around 800 ns. The longer decay can be attributed to bulk recombination processes in $MAPbBr_3$, while the faster component is associated with surface-related recombination[187], [191], [192]. As a result, nonradiative surface recombination (PL quenching) is more pronounced in untreated SCs compared to laser-treated ones (Figure 22b).

These findings support the conclusion that the enhancement in PL intensity after laser treatment originates from effective surface passivation. The potential passivation mechanisms are further explored below. To quantify the PL efficiency improvement, we compared the integrated areas under the short-lived region of the PL decay curves for both samples (Figure 23). The ratio of these integrals is approximately 50, which aligns well with the two orders of magnitude increase in relative PL intensity shown earlier in Figure 18a.

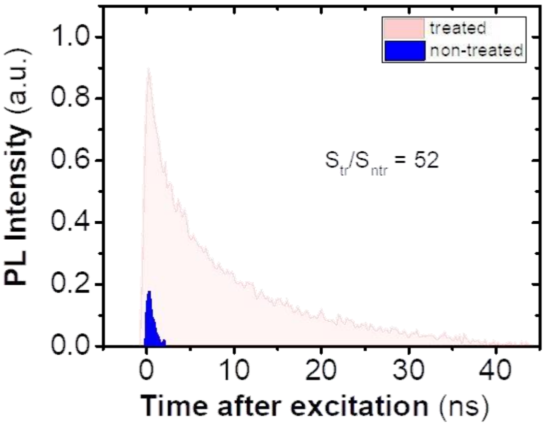

Figure 23. Evaluation of the S_{tr}/S_{ntr} ratio, defined as the ratio of the integrated areas under the surface-related components of the PL decay curves for laser-treated (rose) and untreated (blue) $MAPbBr_3$ SC.

Another noteworthy feature of the laser-treated $MAPbBr_3$ SCs is the presence of a broad dip below 350 nm in the PLE spectrum (Figure 22a). This phenomenon is attributed to the formation of a $PbBr_2$ layer, which exhibits an absorption edge near 350 nm. A similar ¨optical filtering¨ effect in the PLE response was previously reported for $MAPbI_3$ PC films, where it was linked to photoinduced PbI_2 formation[188].

To further investigate this aspect, we analyzed the XRD patterns of the crystals before and after laser exposure, as shown in Figure 24a. In the pristine state, the $MAPbBr_3$ SC displays diffraction peaks at 14.93°, 30.14°, and 45.90° (highlighted with green arrows), corresponding to the (111), (200), and (300) planes of the cubic phase, respectively. After laser treatment, grazing incidence XRD was employed to focus on surface features. New diffraction peaks emerge at $2\theta = 23.74°$, 28.80°, 30.52°, and 40.79° (gray arrows), which correspond to the (021), (022), (121), and (123) planes of orthorhombic $PbBr_2$. These results confirm that both the short-wavelength absorption dip in the PLE spectrum (Figure 22a) and the white surface layer seen after extended laser exposure (Figure 17) originate from the formation of $PbBr_2$. Meanwhile, residual peaks at $2\theta =$ 14.89°, 30.14°, and 33.89° (green arrows) are consistent with the (111), (200), and (210) reflections of the cubic $MAPbBr_3$ phase, respectively.

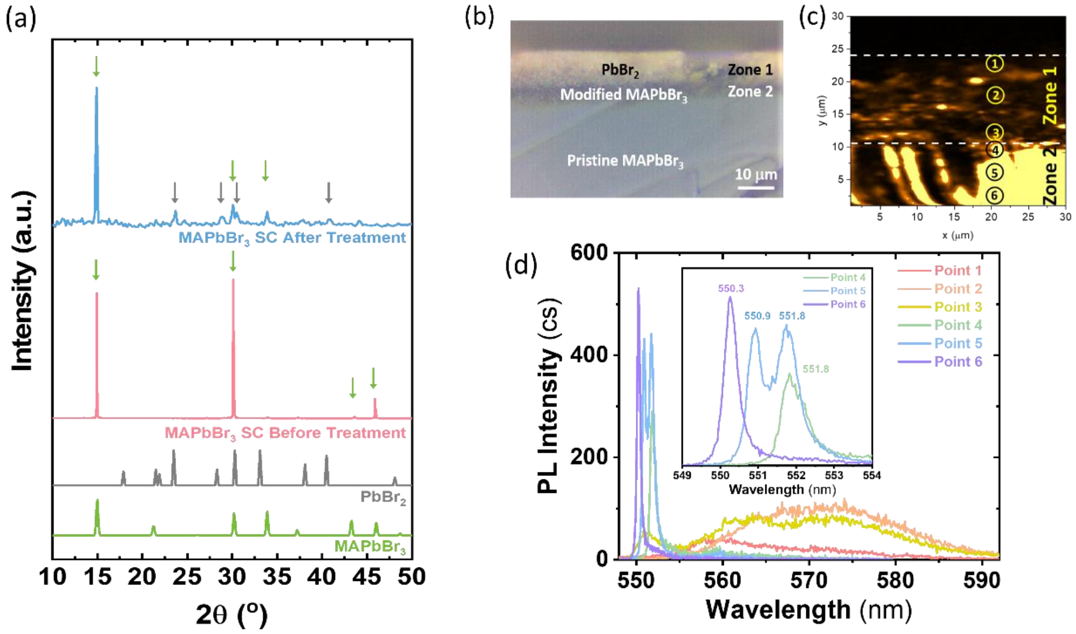

Figure 24. (a) XRD patterns of $MAPbBr_3$ SCs before and after laser exposure, shown alongside theorical patterns for $PbBr_2$ and $MAPbBr_3$. (b, c) Cross-sectional analysis of a laser-treated

$MAPbBr_3$ SC: (b) optical microscopy image and (c) μPL intensity map at 551 nm. (d) μPL spectra recorded at six specific locations labeled 1–6 in panel (b). The inset presents a magnified view of the excitonic region between 550 and 552 nm. Both (c) and (d) were acquired at a temperature of 4 K.

To evaluate the modifications occurring in the near-surface region of $MAPbBr_3$ SCs following laser treatment, we conducted a cross-sectional analysis using optical microscopy and μPL techniques. The optical image (Figure 24b) supports the hypothesis of a stratified structure induced by laser exposure. A bright superficial layer approximately 10 μm thick is clearly visible (designated as Zone 1) and is attributed to $PbBr_2$, as evidenced by its light-scattering behavior. Beneath this, a darker intermediate region roughly 7 μm in thickness (Zone 2) is observed, corresponding to a modified $MAPbBr_3$ phase with an expanded band gap and enhanced photophysical properties. Below Zone 2 lies the unmodified bulk of the $MAPbBr_3$ SC. Low-temperature (4 K) μPL mapping at 551 nm, displayed in Figure 24c, further illustrates the spatial distribution of PL across the cross-section. This emission wavelength aligns with the excitonic PL characteristic of the laser-treated SC at low temperatures, see above.

Additionally, μPL spectra were collected at six distinct locations along the cross-section of the crystal, as shown in Figure 24d and mapped in Figure 24c. In Zone 1, spectra 1 and 2 exhibit broad photoluminescence emission with a FWHM of approximately 20 nm, centered around 570 nm. At the interface between Zone 1 and Zone 2 (spectrum 3), a narrower emission band emerges near 552 nm. Deeper within Zone 2 (spectra 4 through 6), sharply defined emission peaks with FWHM values of about 0.4 nm are observed, with maxima ranging from 550 to 552 nm. These narrow bands are significantly more intense, by a factor of 5 to 10, compared to the broader emission from Zone 1.

To confirm that the narrow emission bands in the 550–552 nm range observed at 4 K originate from the laser-modified $MAPbBr_3$ in Zone 2, we performed ex situ photoluminescence measurements on both untreated and laser-treated samples at room temperature and under cryogenic conditions (Figure 25). As the temperature decreased from 300 K to 30 K, the PL peak of the treated crystal exhibited a redshift from 529 nm to 549 nm. This trend is consistent with the excitonic emission bands detected in the 550–552 nm range in our μPL experiments at 4 K, thereby validating their assignment to the modified $MAPbBr_3$ phase.

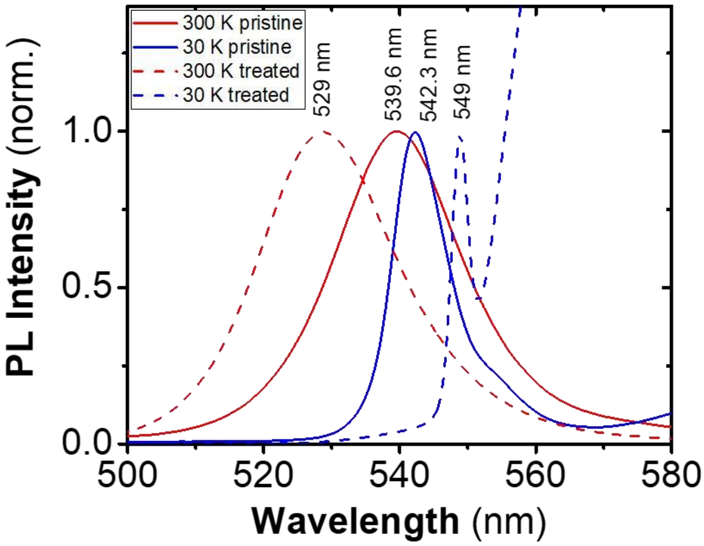

Figure 25. PL spectra of pristine (solid lines) and laser-treated (dashed lines) $MAPbBr_3$ SCs measured at 300 K (red) and 30 K (blue).

Based on the combined analysis of μPL mapping and optical microscopy, we can conclude that both the $PbBr_2$ surface layer (Zone 1 in Figure 24) and the underlying modified $MAPbBr_3$ layer (Zone 2 in Figure 24) each exhibit a thickness of approximately 10 μm. Moreover, these two regions appear to interpenetrate. Dark features originating from the $PbBr_2$ layer extend into the brighter domain of the modified $MAPbBr_3$, and isolated bright inclusions of the modified perovskite are also discernible within the darker $PbBr_2$ zone (Figure 24c). Additionally, variations in the peak position of the excitonic PL within Zone 2 are observed across different spatial locations, indicating a certain degree of structural and optical inhomogeneity in the modified $MAPbBr_3$ layer (Figure 24d).

Understanding the crystalline structure of the modified $MAPbBr_3$ region is crucial to elucidate the origin of the observed band gap widening after laser treatment. A comparison of the (100) diffraction peak before and after treatment (Figure 24a) reveals a shift from 14.93° to 14.89°. This displacement toward lower 2θ angles is indicative of lattice expansion. When tensile strain is introduced in a material, it modifies the atomic spacing within the lattice. Such strain-induced distortions can significantly influence the electronic band structure, often resulting in a variation of the band gap. Specifically, in the case of tensile strain, an increase in the band gap relative to the unstrained (pristine) crystal is typically observed. Numerous studies have reported a clear correlation between lattice deformation and band gap modulation in MHPs[193], [194], [195], [196], [197].

Moreover, Kelvin probe force microscopy (KPFM) measurements were carried out to further understand the changes at the crystal surface. Figure 26 displays 2 mm × 2 mm maps of both the topography (represented in xyz format) and the contact potential difference (CPD) using a color scale, comparing the untreated and laser-treated crystals.

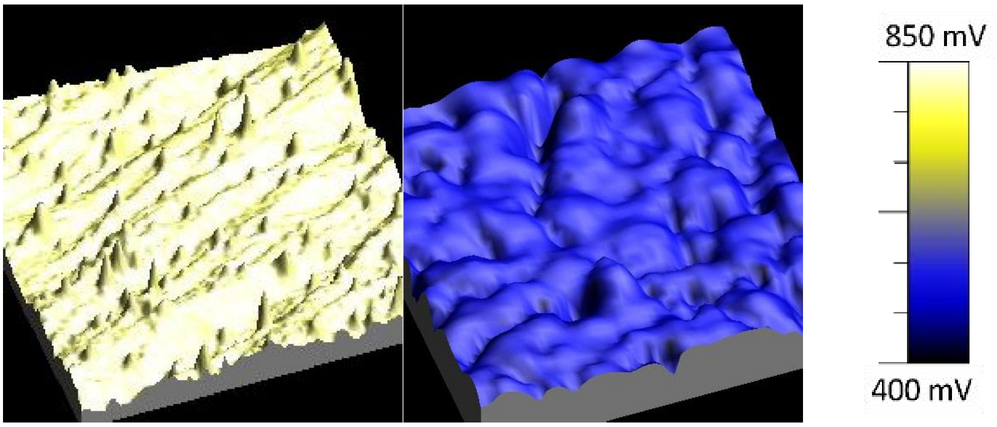

Figure 26. 3D maps illustrating the combined topography and CPD for (a) a pristine $MAPbBr_3$ single crystal (topography scale: 0–14 nm) and (b) a laser-treated crystal (topography scale: 0–380 nm). The CPD is defined as the difference between the work function of the tip and that of the sample, given by: $(eCPD_{sample}=\phi_{tip}—\phi_{sample})$. Since determining the tip's work function precisely is challenging, measurements are calibrated using a gold reference: $(eCPD_{ref} = \phi_{tip} — \phi_{ref})$. This allows calculation of the sample's work function as: $\phi_{sample}=\phi_{ref}+e(CPD_{ref}—CPD_{sample})$. Using this approach, the work function values obtained were: Passivated: CPD_{pass} = 470 mV ; Φ_{ref} = 5.27 eV ; CPD_{ref} = 220 mV and Pristine: $CPD_{pristine}$= 790 mV ; Φ_{ref} = 5.27 eV ; CPD_{ref} = 270 mV.

The pristine SC exhibits an exceptionally smooth surface, with a root-mean-square (RMS) roughness of 1.3 nm, whereas the treated sample displays a markedly rougher texture, reaching an RMS value of 40.6 nm. These findings are consistent with the SEM images provided in Figure 27. Regarding the CPD, which reflects the relative surface work function, the data reveal an average increase of approximately 300 mV following laser exposure. Using gold as a reference electrode, the estimated work functions of the untreated and laser-treated perovskite surfaces are 4.75 eV and 5.02 eV, respectively (Figure 26). The value obtained for the pristine SC aligns well with previously published ultraviolet photoelectron spectroscopy results[198]. In contrast, the elevated work function observed in the laser-treated sample supports the presence of a thin $PbBr_2$ layer at the crystal surface.

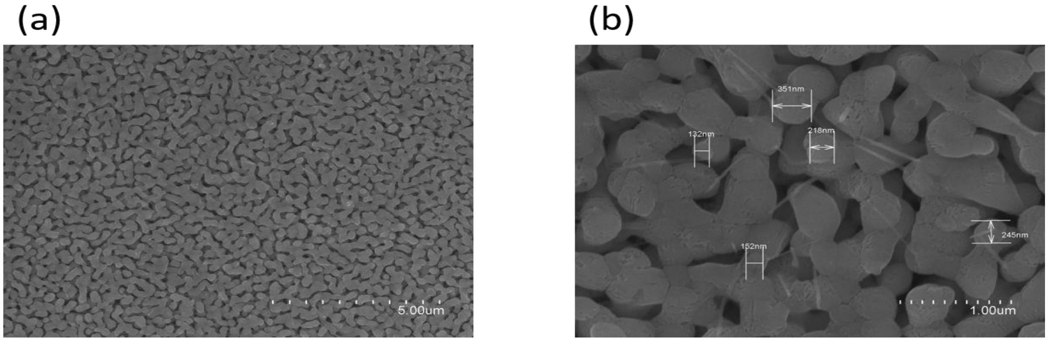

Figure 27. **S**EM top-view image of the $MAPbBr_3$ SC surface after laser treatment.

The key question that follows is how the $PbBr_2$ and the modified $MAPbBr_3$ layers originate during laser exposure. It is hypothesized that the $PbBr_2$ layer forms as a result of complete photoinduced decomposition of the methylammonium ($CH_3NH_3^+$, MA^+) under laser illumination. In contrast, the modified $MAPbBr_3$ region is likely produced through partial decomposition of MA^+, causing lattice distortions within the perovskite structure. A similar mechanism was previously proposed to explain the emergence of blue-shifted PL in $MAPbI_3$ nanocrystals subjected to blue laser irradiation at 10 W/cm^2[189]. In that study, decomposition of $CH_3NH_3^+$ led to a reduction in the Pb–I–Pb bond angle from approximately 170.8° in the tetragonal $MAPbI_3$ phase to 120° in PbI_2, accompanied by a band gap increase from ~1.6 eV to ~2.48 eV.

In general, it is well documented that decreasing the Pb–X–Pb bond angle (where X = I, Br) results in a widening of the band gap in metal halide perovskites[199], [200]. Moreover, light-induced decomposition of $CH_3NH_3^+$ in $MAPbX_3$ (X = I, Br) systems, particularly under oxygen-rich conditions, is a well-known phenomenon[201], [202]. However, this process can also proceed in oxygen-free environments, as demonstrated in $MAPbBr_3$[203]. In our experiments, the formation of the $PbBr_2$ surface layer and the associated enhancement in PL intensity were observed exclusively under laser exposure in the presence of atmospheric oxygen (see Figure 28).

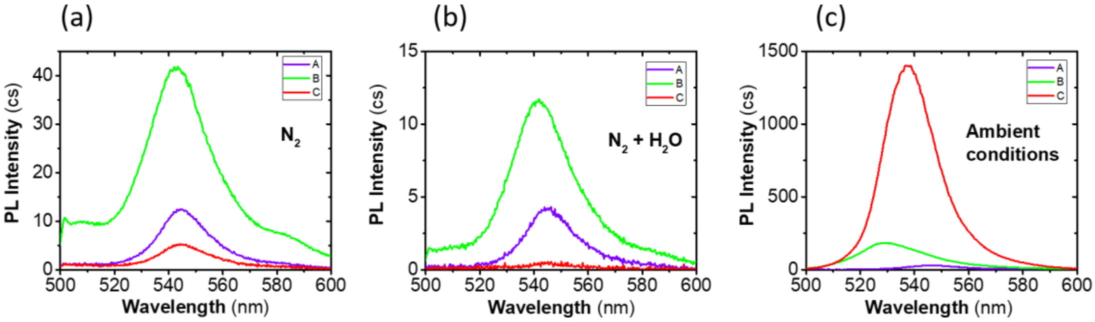

Figure 28. PL spectra of $MAPbBr_3$ SCs recorded before laser treatment (A, excitation fluence: 0.15 W/cm^2), after laser treatment (B, 1.5 W/cm^2 for 10 min), and following post-treatment (C, 0.15 W/cm^2 for 10 min), measured under different atmospheric conditions: (a) dry N_2, (b) N_2 with H_2O vapor, and (c) ambient air.

To evaluate the chemical composition of the $MAPbBr_3$ crystal surface after laser treatment, high-energy resolution XPS using synchrotron radiation was performed on both untreated and laser-exposed SCs. This synchrotron-based elemental XPS technique enables the selective probing of chemical changes in multicomponent systems at the atomic level, thereby allowing precise identification of the chemical species present at the outermost surface of the samples. The XPS measurements were conducted with an incident photon energy of 515 eV under grazing emission geometry, a configuration that enhances surface sensitivity and limits the effective probing depth to approximately 1–3 nm.

Figure 29 presents the core-level XPS spectra corresponding to Pb 4f, Br 3d, N 1s, and C 1s for both untreated and laser-treated $MAPbBr_3$ SCs. In the pristine samples, the binding energies of the Pb $4f_{7/2}$ (Figure 29a), Br $3d_{7/2}$ (Figure 29b), N 1s (Figure 29c), and C 1s (Figure 29d) signals are located at 138 eV, 68 eV, 401 eV, and 284.2 eV, respectively. These values are in full agreement with those reported in the literature for high-purity $MAPbBr_3$ SCs[201], [204]. The observed binding energies are consistent with a chemically clean perovskite surface. In addition, the Pb $4f_{7/2}$ spectrum reveals the presence of metallic lead (Pb^0), which is in line with previous photoemission studies[205], [206].

Following laser treatment, additional spectral features emerge in the Pb 4f and Br 3d core-level regions, indicating chemical modifications at the crystal surface. In the Pb 4f spectrum, a new Pb $4f_{7/2}$ component appears at a binding energy of 139 eV, which is characteristic of $PbBr_2$ formation. A complementary signal also arises in the Br $3d_{5/2}$ region, further corroborating the presence of this halide salt on the surface. Notably, the N 1s spectrum (Figure 29c) no longer exhibits any detectable signal, suggesting the complete decomposition of the methylammonium. In parallel, Figure 29d reveals the emergence of peaks corresponding to C–O and C=O chemical bonds. These features are attributed to the formation of formic acid (HCOOH), which can be associated to byproduct resulting from the breakdown of MA under photochemical conditions.

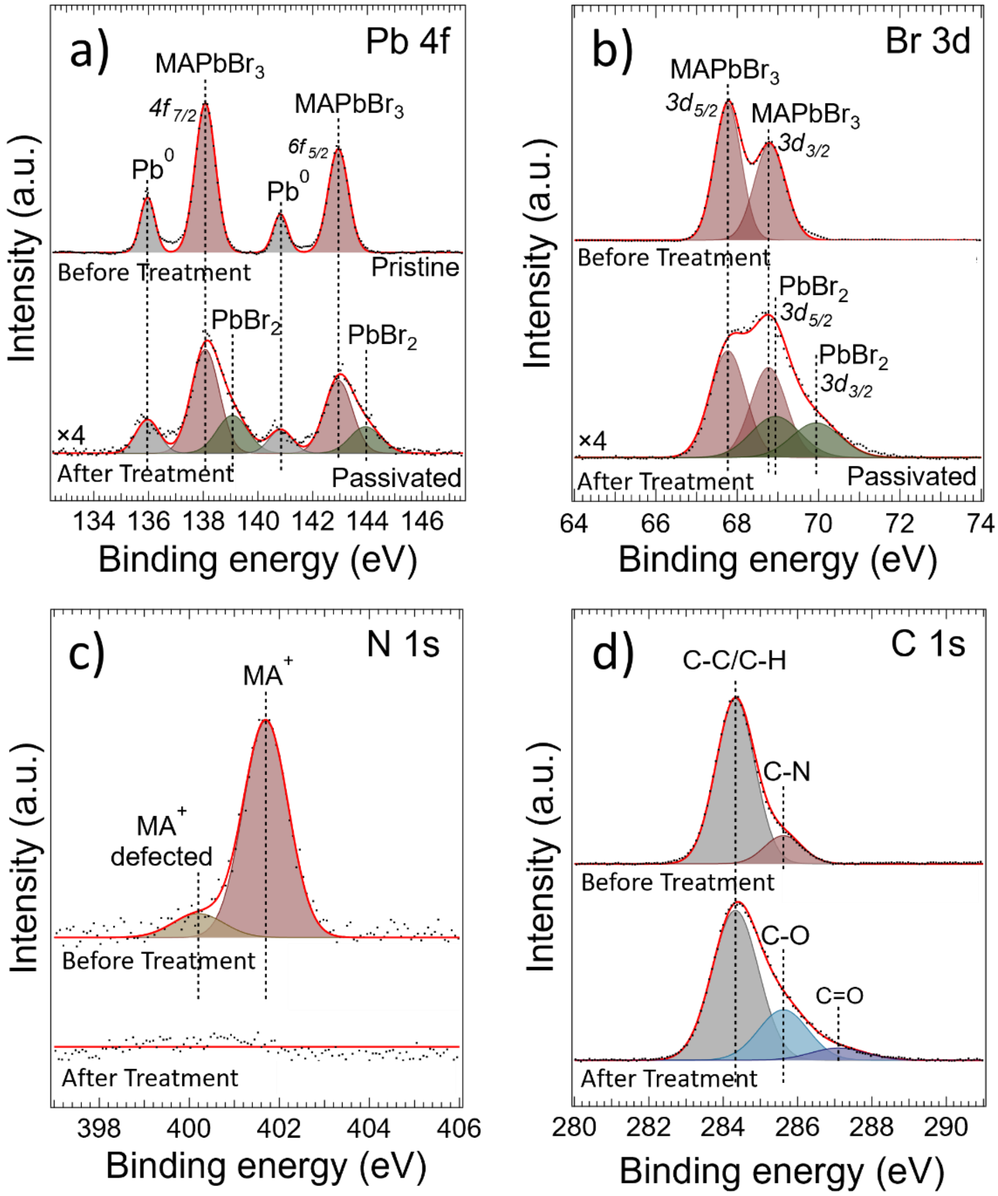

Figure 29. High-resolution XPS spectra obtained in grazing emission geometry for $MAPbBr_3$ SCs before and after laser treatment, showing core-level signals of (a) Pb 4f, (b) Br 3d, (c) N 1s, and (d) C 1s. Measurements were performed using synchrotron radiation with an incident photon energy of 515 eV. The experimental configuration involved normal photon incidence and photoelectron detection at a grazing emission angle of $\theta = 5°$, ensuring enhanced surface sensitivity.

An intriguing question that emerges is why the Pb 4f core level remains visible in the XPS spectrum of the laser-treated $MAPbBr_3$ SC, while the N 1s signal is absent. A plausible explanation lies in the kinetic energy (KE) of the photoelectrons emitted during the XPS measurement. The KE of these electrons is determined by subtracting the binding energy (BE) of the core level from the incident photon energy. For the current experimental conditions (hv = 515 eV), the kinetic energy of Pb 4f photoelectrons is approximately 375 eV (KE Pb 4f = 515 eV – 140 eV), whereas the N 1s photoelectrons have a much lower kinetic energy of about 113 eV (KE N 1s = 515 eV – 402 eV).

The marked different in kinetic energy between the Pb 4f and N 1s photoelectrons suggests that Pb 4f electrons, having higher energy, are capable of escaping from deeper within the crystal structure. In contrast, N 1s photoelectrons, with substantially lower kinetic energy, are less likely to reach the surface if they originate from subsurface regions. As illustrated in Figure 24, the $PbBr_2$ and modified $MAPbBr_3$ layers are interpenetrated, forming a mixed interface. Consequently, the absence of a detectable N 1s signal, combined with the persistent Pb 4f emission, supports the conclusion that partial decomposition of $CH_3NH_3^+$ has occurred within the $PbBr_2$ region. This process results in a distorted perovskite lattice embedded in the $PbBr_2$ layer, which is responsible for the observed band gap broadening.

Based on XPS analysis, we propose a plausible chemical mechanism underlying the $CH_3NH_3^+$ decomposition within the $MAPbBr_3$ lattice.

$CH_3NH_3PbBr_3 \rightleftharpoons CH_3NH_3^+ + Br^- + PbBr_2$ Equation 6

$CH_3NH_3^+ + Br^- \rightarrow HBr(g) + CH_3NH_2(g)$ Equation 7

$CH_3NH_2(ads) + O_2(g) \rightarrow HCOOH + NH_3(g)$ Equation 8

Equation 5 illustrates the dynamic equilibrium between $MAPbBr_3$ and its precursor compounds, $PbBr_2$ and MABr. This equilibrium can be disrupted by various external stimuli. It is widely recognized that both light and heat can promote the decomposition of $MAPbBr_3$, primarily due to the high mobility of halide ions[207]. As a result, a range of organic byproducts and metallic lead species may form. Specifically, bromide ions (Br^-) can interact with $CH_3NH_3^+$ to yield hydrogen bromide (HBr) and methylamine (CH_3NH_2) gas, as shown in equation 6.

Furthermore, CH_3NH_2 molecules adsorbed on the $MAPbBr_3$ surface can undergo reactions with molecular oxygen (O_2), leading to the formation of formic acid (HCOOH) and ammonia (NH_3), as described in equation 7. These chemical processes shift the equilibrium shown in equation 5 toward the formation of degradation products[208], [209], ultimately resulting in the development of a $PbBr_2$ surface layer approximately 10 µm thick. Concurrently, when the decomposition of $CH_3NH_3^+$ is incomplete, a modified $MAPbBr_3$ phase with a widened band gap is formed beneath the $PbBr_2$. Under such conditions, it is plausible that both methylamine and formic acid persist near the lattice-distorted $MAPbBr_3$, where they may contribute significantly to surface passivation by mitigating nonradiative recombination pathways and enhancing thermal stability[210], [211], [212].

The stabilization of $MAPbBr_3$ by formic acid and methylamine is likely driven by competitive adsorption phenomena involving various molecular species. As indicated in Ref. 213, water (H_2O) and carbon dioxide (CO_2) are adsorbed onto samples fabricated under ambient atmospheric conditions[213]. Among these, H_2O is particularly detrimental, as it is known to promote the chemical degradation of perovskite structures[214]. Therefore, minimizing the surface concentration of water, can enhance the long-term stability of the material by preventing the emergence of nonradiative recombination centers.

3.3 Conclusions

In summary, a comprehensive set of analyses, PL, µPL, grazing incidence X-ray diffraction, and XPS was conducted to elucidate the mechanisms underlying the laser-induced formation of a passivated, highly luminescent $MAPbBr_3$ layer exhibiting a band gap expansion of approximately 75 meV in $MAPbBr_3$ SCs . The results support the hypothesis that partial light-driven decomposition of the $CH_3NH_3^+$ cation leads to a structurally distorted crystalline phase with an enlarged band gap. Furthermore, the laser treatment promotes the generation of formic acid and methylamine, which contribute to the chemical passivation of the modified $MAPbBr_3$ surface and enhance its environmental resilience, particularly against moisture-induced degradation.

Chapter 4

Perovskite Thin Single Crystal for a High Performance and Long Endurance Memristors

Chapter 4 contains key results from the development of a perovskite SC-based memristors. In this chapter it is demonstrate that both endurance and LRS/HRS ratio can be significantly improved by the use of $MAPbBr_3$ TSCl based memristors compared to PC counterpart. The findings discussed throughout this chapter are derived from, and consistent with, those reported in a peer-reviewed published article; Adv. Electron. Mater. **10**, 2300475 (2024).

Everything detailed in this chapter aligns with the established data and conclusions within the original publication

Abstract

MHPs possess both electronic and ionic transport properties that make them well-suited for memristive applications. Nevertheless, memristors based on PC thin-film perovskites frequently face reliability limitations arising from grain boundary effects, while devices employing bulk SC perovskites often exhibit limited LRS/HRS resistance ratios. In this chapter, we present a memristive device fabricated from a wide-bandgap perovskite, $MAPbBr_3$, configured as a TSC with a high surface-to-thickness ratio. This architecture successfully addresses both challenges, achieving an impressive LRS/HRS ratio of up to 50 and demonstrating endurance over 10^3 switching cycles, among the highest values reported to date. The device's remarkable stability allows for detailed investigation of the electroforming process behavior via impedance spectroscopy, offering valuable insights into the underlying switching mechanism. To the best of our knowledge, this represents the first report of a memristor based on a thin SC-MHP, as well as the first time the electroforming dynamics have been characterized through impedance spectroscopy.

4.1 Introduction

Despite their exceptional performance as semiconductors, MHPs exhibit an intrinsic mixed electronic–ionic transport nature, which can significantly reduce their response times[215], [216], [217]. A direct manifestation of this duality is the frequent observation of hysteresis in I-V characteristics of perovskite solar cells, often leading to notable discrepancies between FS and RS. This phenomenon reflects a time-dependent lag in the material's response to external electric fields, resulting in dynamic resistive behavior[218], [219], [220]. In addition to ionic effects on resistance, perovskite materials have also been shown to exhibit substantial capacitive responses. These have been extensively characterized using frequency-domain techniques such as impedance spectroscopy[221], [222], as well as through time-domain[223].

Although phenomena such as hysteresis can represent an issue evaluating the photovoltaic performance, the ionic conductivity of MHPs, when combined with their outstanding optoelectronic characteristics, opens up opportunities for alternative device architectures beyond solar cells, including switchable diodes and memristors[138], [224], [225], [226], [227], [228]. Memristors operate based on the resistive switching mechanism that underlies the hysteresis effect: a reversible transition from a HRS to a LRS triggered by the application of a threshold voltage (ON state), which can subsequently be reset to HRS by applying a voltage of opposite polarity (OFF state). This reversible change in internal resistance enables the encoding and storage of information. For advanced computing applications such as spiking neural networks or artificial synapses, memory elements capable of operating over multiple temporal regimes are essential. These involve both drift-driven (non-volatile) and diffusion-based (volatile) resistive behaviors[229], [230], [231].

The rich interplay between electronic charge carriers and ionic migration in MHPs provides a diverse landscape of charge transport mechanisms, aligning well with the stringent requirements for high-performance memristive devices. Key performance metrics for such devices include non-destructive readout capability, a large current ratio between HRS and LRS states, low operating voltage, long retention times, high endurance over multiple switching cycles (set/reset operations), and rapid switching speeds[232], [233], [234], [235]. These criteria have driven significant progress in the development of perovskite-based memory technologies.

Despite the promising outlook of MHP-based memristors as potential alternatives to conventional oxide-based technologies[236], several critical challenges remain, as achieving sufficient endurance and reliability. To date, much of the research has focused on devices employing PC thin films[126], [237], bulk SCs[121], [238], or perovskite nanocrystals[239]. However, many of these systems suffer from unstable steady-state response, which hampers detailed analysis of their resistive switching mechanisms. Consequently, the fundamental operating principles of these devices remain a subject of ongoing investigation, and a comprehensive understanding of their electroforming process, the activation of a pristine device into a functional memristor, has yet to be clearly established.

For PC thin films, one of the main challenges lies in achieving high surface uniformity and smoothness, as the solution-based fabrication methods often introduce variability that hinders reproducibility across individual devices. The inherent presence of grain boundaries and frequent pinholes in these films contributes to parasitic leakage currents, which facilitate degradation mechanisms and undermine the stability and reliability of perovskite-based memristors for commercial applications. Furthermore, the nanometer-scale thickness typical of PC films leads to elevated intrinsic electronic currents, which in turn suppress the ionic migration processes required for resistive memory functionality.

To address some of these limitations, memristors based on SC-MHPs have been explored. SC perovskites offer superior ionic transport and reduced operating currents, owing to the absence of grain boundaries and a significantly lower density of structural defects. These features enable the development of memristive devices with fast switching dynamics, reduced power consumption, and enhanced endurance. However, the bulk SCs typically exhibit millimeter-scale thickness, which can adversely affect several of their optoelectronic properties. Parameters such as light absorption and emission, charge carrier mobility, surface recombination, and mechanical response are all strongly influenced by the increased thickness of the material[240], [241], [242].

Table 1 provides a comparative summary of various MHP-based memristive devices. In the case of devices with simple architectures, typically comprising basic electrodes and at most one buffer layer, high LRS/HRS resistance ratios are often achieved. However, these devices tend to suffer from elevated set/reset voltages and limited endurance. An exception to this trend is found in one outstanding device reported in Ref. 253, which combines excellent memristive behavior with a simple design. Overall, devices with simplified structures must still overcome the challenge of improving endurance without compromising the high LRS/HRS ratio. To address this limitation, more complex architectures incorporating multiple material layers, such as Pt, Pd, polymethylmethacrylate (PMMA), or SiO_2, have been employed. This multilayer approach enhances endurance while preserving adequate LRS/HRS ratio, though it also leads to increased fabrication complexity and cost. These additional expenses are compounded by the need for controlled environments (e.g., glove boxes) and device encapsulation. It is worth noting that the table does not include devices exhibiting LRS/HRS ratios below 10, as they fall outside the targeted performance criteria. This bottleneck is solved by adding several layers of different materials, such as Pt, Pd, polymethylmethacrylate PMMA, SiO_2, etc. This method improves the endurance time while maintaining a decent LRS/HRS ratio, but manufacturing costs increase significantly, adding the implicit costs of making the devices in glove boxes plus the encapsulation requirement. It is important to note that devices exhibiting an LRS/HRS ratio lower than 10 have been excluded from this table.

Table 1. Overview of different memristor devices based on polycrystal MHPs.

Structure	LRS/HRS ratio	V_{set} (V)	V_{reset} (V)	Endurance (cycles)	Retention (seconds)	Reference
FTO/$MAPbI_{3-x}Cl_x$/Au	10^4	1.47	-1.41	400	$4.68*10^4$	[243]
FTO/$CsPbBr_3$/Au	10^3	1.5	-1.2	100	10^3	[244]
Ag/$CsPbBr_3$/MoO_3/Ag	100	0.7	-0.8	50	10^4	[245]
ITO/$MAPbI_3$/Au	10	0.7	-0.61	500	10^4	[246]
ITO/PEDOT:PSS/$MAPbBr_3$/Al	$3.6*10^6$	-0.2	3	120	10^4	[247]
PET/ITO/$MAPbI_3$/Au	50	0.7	-0.5	400	10^4	[248]
PET/ITO/Cs_3Bi2I_9/Au	10^3	0.3	-0.5	10^3	10^4	[249]
FTO/c-TiO_2/$MAPbI_{3-x}Cl_x$/Al	$1.9*10^9$	1.10	-1.65	160	$2*10^3$	[126]
ITO/$MAPbI_3$/ZnO/Au	500	0.9	-1.5	100	10^4	[232]
ITO/PEDOT:PSS/$MAPbI_3$/Cu	10^4	-0.6	2	$3*10^3$	$3*10^4$	[250]
Si/SiO_2/Ti/Pt/$MAPbI_3$/Ag	10^6	0.13	-0.13	350	10^4	[251]
PET/ITO/PMMA/$CsPbBr_3$QDs/PMMA/Ag	$6*10^5$	2.6	-2.7	$5*10^3$	$4*10^5$	[252]
Ag/$MAPbI_3$/Au	10^8	1.16	0.46	10^3	10^4	[253]

In this study, we combine the favorable features of PC perovskite thin films with the inherent stability of SC materials by the synthesizing a perovskite TSC. We report the development of a highly stable TSC perovskite-based memristor that exhibits a simple device architecture along with exceptional endurance, while maintaining a balanced LRS/HRS resistance ratio. Notably, the fabrication process is carried out entirely under ambient conditions and does not require encapsulation. To enhance ionic transport, a wide bandgap perovskite, $MAPbBr_3$, is employed in the form of a TSC, serving as the active layer in the memristive device. The device exhibits exceptional long-term operational stability, maintaining consistent current levels over a duration of 10^4 seconds and achieving endurance across approximately 10^3 set/reset switching cycles. Notably, these values, obtained under ambient conditions, rank among the highest endurance performances reported thus far. The robust stability of the memristor allows the application of impedance spectroscopy as an effective technique to investigate the electroforming process that governs the resistive switching behavior. By analyzing the impedance spectra corresponding to both the electroforming stage and the LRS, we confirm the critical role played by ionic migration in the device’s switching mechanism.

4.2 Experimental

Materials:

Lead(II) bromide ($PbBr_2$) was purchased from TCI, and methylammonium bromide (CH_3NH_3Br) was supplied by GreatCell. PTAA was acquired from Ossila. DMF and DMSO were purchased from Thermo Scientific, while toluene was sourced from VWR. Graphite spray was procured from RS. All chemicals were used as received without further purification

Fabrication process:

TSC devices: The $MAPbBr_3$ precursor solution (1.8 M) was prepared by dissolving equimolar amounts of $PbBr_2$ and CH_3NH_3Br in a 10:1 volume ratio of DMF:DMSO. The mixture was vigorously shaken until fully dissolved. Separately, PTAA was dissolved in toluene at a concentration of 2 mg/mL. All solutions were filtered through 0.2 µm PTFE syringe filters prior to use. Glass substrates coated with indium tin oxide (ITO) were sequentially cleaned in acetone, detergent solution, deionized water, and absolute ethanol using an ultrasonic bath for 10 minutes per step. After drying with a high-pressure air stream, the substrates underwent UV–ozone treatment for 20 minutes. Subsequently, 60 µL of the PTAA solution was deposited onto the ITO substrate via spin coating at 4000 rpm for 30 seconds under ambient conditions. The coated substrates were then annealed at 100 °C for 10 minutes. Next, 40 µL of the $MAPbBr_3$ precursor solution was drop-cast onto the PTAA-coated surface and immediately enclosed with a second substrate also coated with PTAA. The resulting sandwich structure was subjected to a space-confined inverse temperature crystallization (ITC) process to grow thin single crystals. The temperature was gradually increased from 25 °C to 60 °C at a rate of 15 °C/h and maintained at 60 °C for 48 hours. After cooling to room temperature, the substrates were separated using a blade. Graphite electrodes were formed by depositing 10 µL of graphite suspension on both the $MAPbBr_3$ surface and the exposed ITO contact using a micropipette. The solvent evaporated within approximately 60 seconds, leaving behind a solid graphite film that served as the electrode. Notably, all fabrication steps were carried out under ambient conditions, without the use of a glovebox.

Polycrystal devices: A 1.4 M solution of $MAPbBr_3$ was prepared by dissolving the perovskite precursor in a DMF:DMSO solvent mixture with a 1:4 volume ratio. This solution was deposited onto ITO substrates previously coated with PTAA, following the same procedure described for

TSC devices. Perovskite solution was deposited via spin-coating by two sequential steps: an initial ramp at 1000 rpm for 10 seconds, followed by a second ramp at 4000 rpm for 40 seconds. During the second step, 1 mL of toluene was dripped onto the spinning substrate at the 12-second mark to induce antisolvent crystallization. The resulting films were subsequently annealed at 100 °C for 30 minutes to complete crystallization. Graphite electrodes were then deposited onto the $MAPbBr_3$ layer and the exposed ITO surface. All fabrication steps for the polycrystalline devices were performed entirely inside a nitrogen-filled glovebox.

Characterization:

The crystalline structure of the samples was analyzed using X-ray diffraction performed on a Bruker D8 Advance diffractometer equipped with a Cu Kα radiation source (λ = 1.5418 Å). Measurements were conducted in grazing incidence geometry at an angle of 1°, with a scan rate of 5°/min over a 2θ range from 12° to 40°. Surface morphology was examined via scanning electron microscopy using a HITACHI S-4800 instrument (Tokyo, Japan) operated at an accelerating voltage of 2 kV. Photoluminescence measurements were carried out using a confocal micro-photoluminescence spectroscopy system. Samples were placed in the cold finger of a vibration-isolated closed-cycle cryostat (AttoDRY800, Attocube AG). Excitation and collection were performed with a 50× long-working-distance microscope objective (NA = 0.42), positioned outside the cryostat. Emitted light was filtered using a long-pass filter, dispersed by a double 0.3 m focal length spectrograph (Acton SP-300i, Princeton Instruments), and detected using a cooled silicon CCD camera (Newton EMCCD, ANDOR) for spectral measurements. Electrical measurements and impedance spectroscopy were conducted using a Gamry Interface 1010E electrochemical workstation.

4.3 Results and Discussion

4.3.1 Crystallization Method and Design of Thin Single Crystal Perovskite Memristor

TSCs are monocrystalline structures grown within a confined space, allowing precise control over their thickness, and consequently, their physical and optoelectronic properties[254]. Thinner crystals tend to be more mechanically flexible than their thicker counterparts, offering the ability to bend or stretch without fracturing, a clear advantage for applications in flexible memristive devices.

In this confined growth approach, the crystals are synthesized from a precursor solution containing 1.8 M of $PbBr_2$ and MABr dissolved in a DMF:DMSO solvent mixture (10:1 vol:vol). The solution is enclosed between two ITO substrates coated with PTAA. The sandwiched sttructure is heated on a hot plate under ambient conditions using the inverse temperature crystallization technique, which exploits the retrograde solubility behavior of perovskite materials. The temperature is increased to 60 °C at a controlled rate of 15 °C/h to carefully regulate nucleation and crystal growth (see Figure 30).

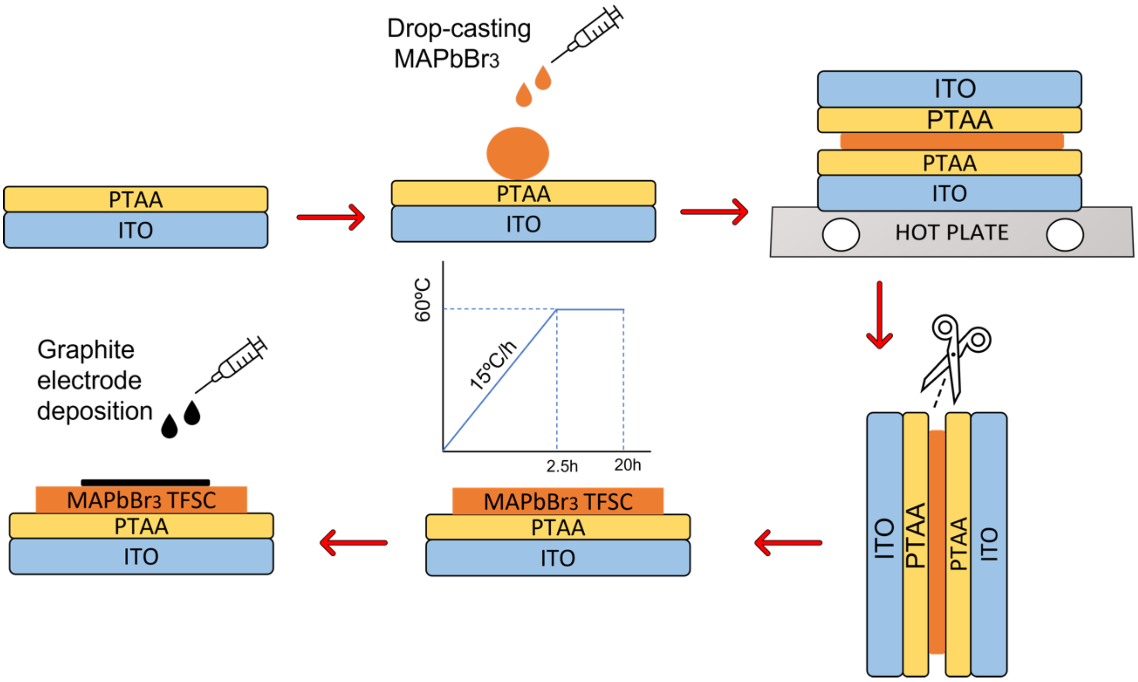

Figure 30: Schematic representation of the confined ITC method used for growing TSCs. Notably, this approach enables the formation of highly crystalline and reproducible $MAPbBr_3$

TSCs at relatively low temperatures. In contrast to conventional methods reported in the literature that operate at temperatures up to 80 °C, the optimized growth here is achieved at 60 °C.

This method reproducibly yields single crystals with thicknesses in the 20–30 μm range and areas of approximately 6 mm^2 (see Figure 31).

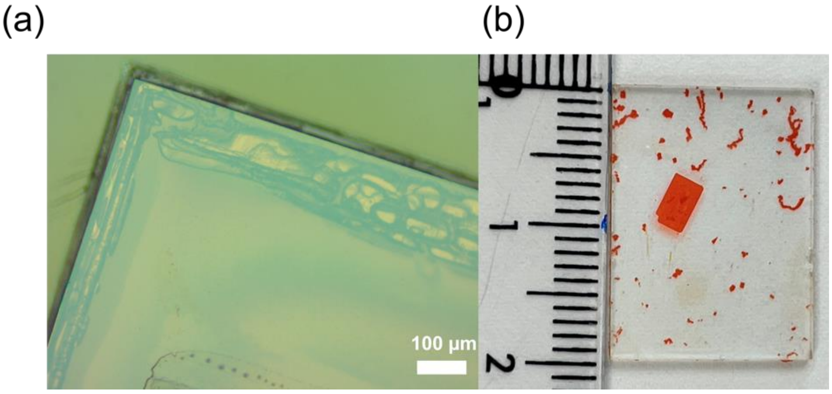

Figure 31: (a) Optical microscopy image of a $MAPbBr_3$ TSC grown via the confined ITC method, exhibiting sharp edges and a well-defined square geometry, indicative of high crystallinity. (b) Real photograph of a representative TSC synthesized by confined ITC method.

Compared to nanometer-thick PC films, these micrometer-scale TSCs offer lower defect densities, which can significantly reduce surface recombination and enable longer charge carrier lifetimes than bulk single crystals (Figure S32)[241].

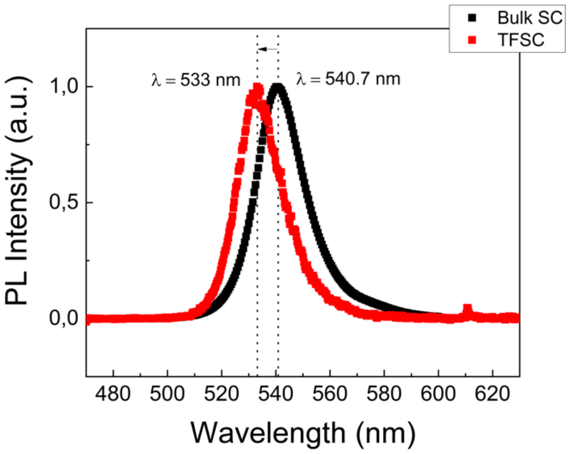

Figure 32: PL spectra comparison between a bulk $MAPbBr_3$ single crystal of 2 mm thickness

(black curve) and the PL emission of TSCs. The blue-shift in the emission peak for the TSCs is attributed to the reduced crystal thickness.

The perovskite composition selected for this study is $MAPbBr_3$, chosen for its inherent properties such as high ionic mobility and strong environmental and operational stability, which are advantageous for memristive applications. Following the crystallization step, the sandwich structure is carefully separated using a blade, leaving the crystal adhered to one of the PTAA coated substrates. For electrical characterization, a graphite spray is applied onto the exposed crystal surface and the ITO contact to complete the device assembly (Figure 33a). This carbon-based electrode offers multiple benefits over conventional metal contacts, including improved sustainability, lower cost, enhanced efficiency, and greater stability. Additionally, its compatibility with flexible substrates further supports its suitability for scalable device fabrication[255], [256].

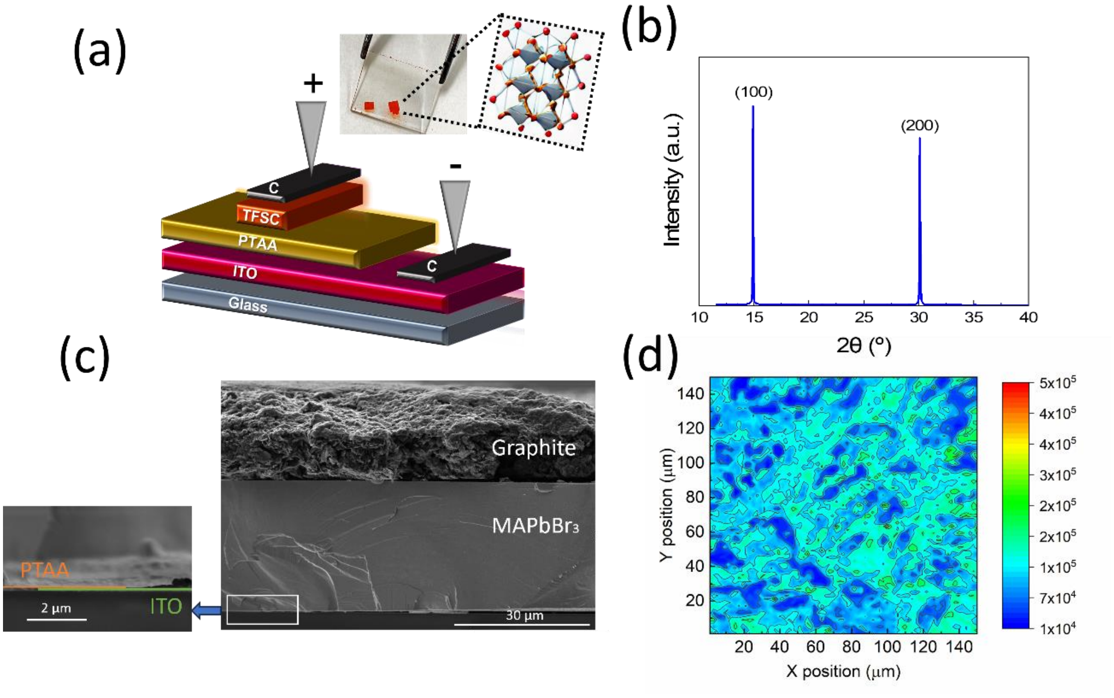

Figure 33. (a) Schematic representation of the complete memristor device structure employing graphite electrodes for electrical characterization. The inset displays a real image of a $MAPbBr_3$ TSC grown on a PTAA layer using the confined ITC method. (b) X-ray diffraction pattern showing diffraction peaks at 15° and 30°, corresponding to the (100) and (200) planes of the cubic $MAPbBr_3$ phase, respectively. (c) Cross-sectional SEM image of a representative device.

(d) Photoluminescence (PL) mapping of the TSC surface, demonstrating high spatial homogeneity in optical response.

To investigate the structural characteristics of the TSC, XRD analysis was conducted to confirm its monocrystalline nature. The presence of sharp and intense reflections corresponding to the (100) and (200) crystallographic planes verify the formation of a highly crystalline cubic perovskite phase (Figure 33). Representative SEM images of the fabricated device are shown in Figure 33c. These images confirm a perovskite crystal thickness of approximately 30 μm, while the top graphite electrode measures around 15 μm in thickness. The PTAA layer, with a thickness of 20 nm, along with the ITO substrate, is visible in the magnified region of the SEM image. To assess the surface uniformity of the TSC, PL mapping was performed to evaluate the homogeneity of its optical response (Figure 33d). The scan covered an area of 60 μm^2, serving as a representative region of the full TSC surface, which typically spans between 6 and 7 mm^2.

4.3.2 Memristor Performance of the Thin Single Crystal Perovskite Device.

A typical resistive switching memristor consists of a two-terminal configuration comprising a top electrode, a semiconducting active layer, and a bottom electrode. In the present device, the anode is connected to the carbon-based electrode deposited on the top surface of the perovskite crystal, while the cathode is established through the carbon layer coated onto the ITO substrate.

Most memristive devices require an initial step known as electroforming, which facilitates the formation of conductive filaments or pathways that enable the transition from the high-resistance state to the low-resistance state. Upon application of an external bias, the electroforming process induces the creation of a conductive channel, thereby switching the device into the LRS. When a voltage of opposite polarity is applied, the conductive path is disrupted in a RESET operation, returning the device to the HRS.

If the ions involved in the process do not fully return to their initial positions, the conductive filaments are only partially disrupted during RESET. As a result, subsequent transitions from HRS to LRS require lower activation energy, and the device progressively stabilizes its set/reset voltage thresholds. Although the precise mechanism governing this process remains under investigation, largely due to the challenges of capturing its rapid and abrupt dynamics in situ, we present a deeper understanding of it through the IS analysis described in the following sections.

Following activation of the device via the electroforming process (see Figure 34), we conducted cyclic voltammetry by applying a voltage sweep sequence of 0 V → +2 V → 0 V → −2.7 V → 0 V to assess the initial switching behavior of the memristor (Figure 35a). In addition to facilitating charge carrier injection and transport, the applied voltage induces a redistribution of ionic species or vacancies throughout the crystal thickness. This ionic migration plays a fundamental role in enabling the transition between different resistive states in the device.

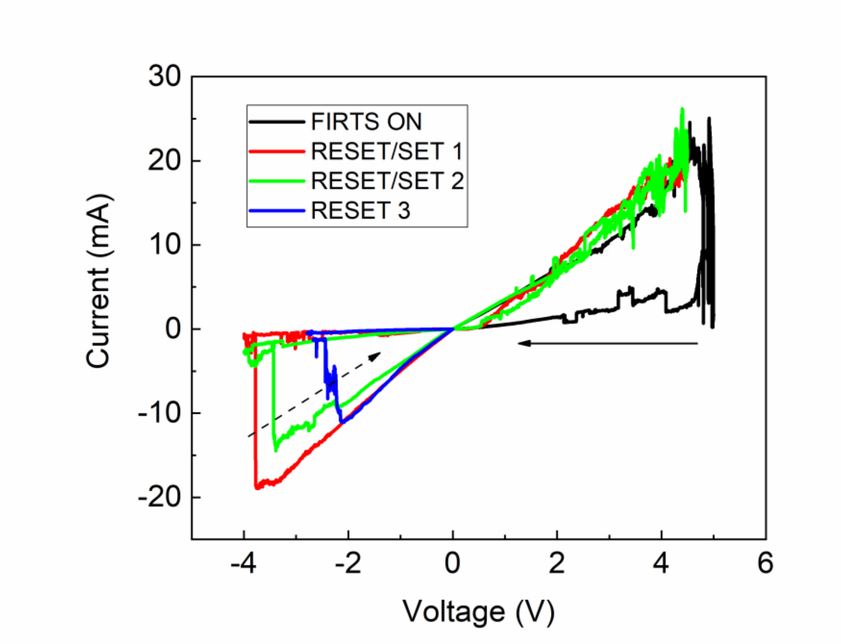

Figure 34: I-V curves illustrating the progressive reduction in the voltage required to switch the memristor device ON (solid black lines) and OFF (dashed black line); from red to blue.

Although the precise origin of this mechanism remains a subject of active research and is beyond the scope of this study, several hypotheses have been proposed in the literature, including the formation of conductive filaments or interfacil adjustments[233], [250] among others[45].

In our measurements, as the applied voltage increases from 0 to +2 V, a sharp rise in current is observed at approximately 0.6 V. This corresponds to the set voltage at which the device undergoes the transition from the HRS to the LRS, with current levels reaching the milliampere (mA) range. To verify the non-volatile behavior of the memristor, it is essential that the device retains its resistive state over a defined voltage window. For this purpose, a reverse voltage sweep from 0 to −2.7 V was applied. At −2.3 V, the transition from LRS back to HRS occurs, which is identified as the reset voltage, accompanied by a drop in current to the microampere (μA) range (Figure 35a).

To evaluate the stability of the device under repeated cycling, 100 consecutive I–V sweeps were conducted (Figure 35a). Selected cycles (1, 30, 50, 90, and 100) are displayed in solid colors, while the remaining traces are shown with translucent lines to provide a clearer visual comparison. The similarity between the first (black line) and final (yellow line) cycles demonstrates the operational robustness and repeatability of the device.

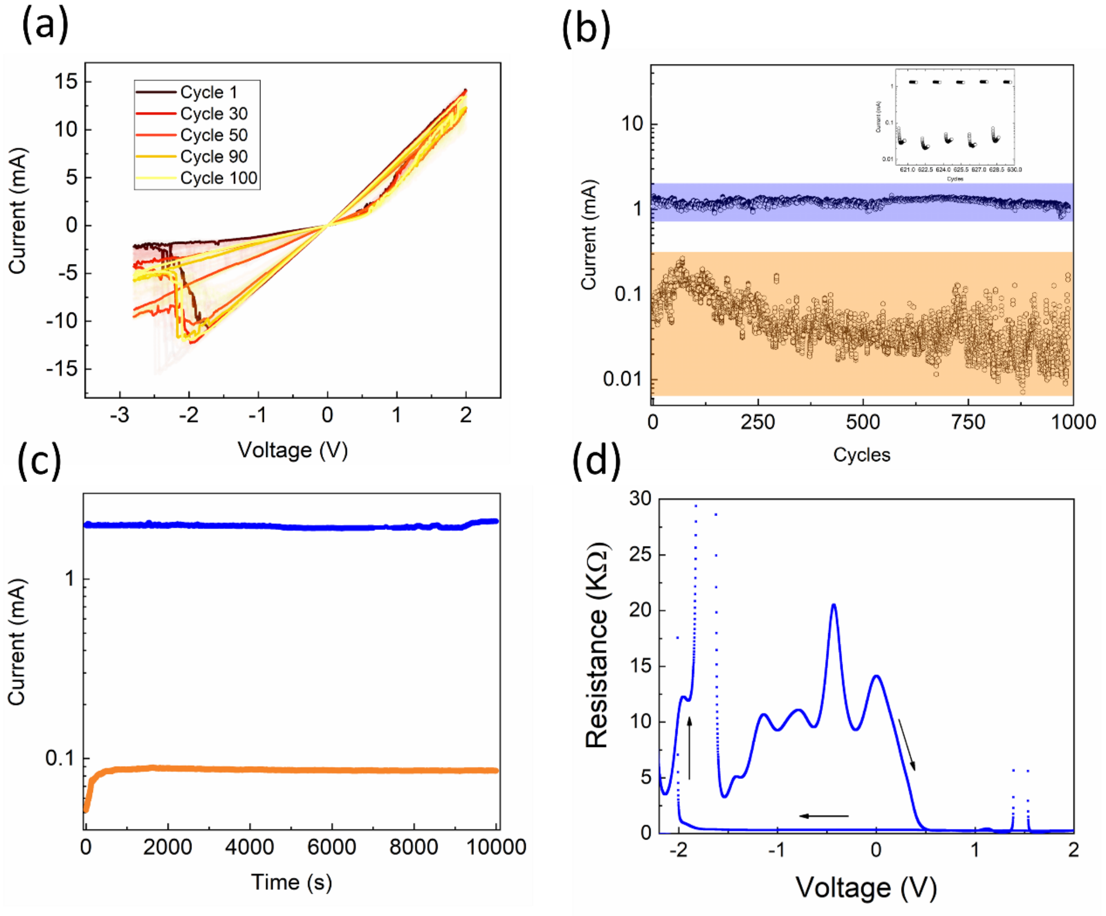

Figure 35. (a) I-V curves, in log scale, showing the SET and RESET over 100 cycles, recorded at a scan rate of 100 mV/s. (b) Endurance performance test under repeated voltage sweeps (+0.1 V → +1 V → +0.1 V → −2.5 V → +0.1 V). (c) Current stability monitored at a read voltage of 0.1 V for the LRS (blue line) and HRS (orange line). (d) Resistance evolution during the switching transitions between HRS and LRS.

To benchmark the cyclic voltammetry performance of the TSC-based memristor, we fabricated a reference device using a $MAPbBr_3$ PC thin film with the same architectural design. As shown in Figure 36, the TSC configuration clearly outperforms its PC counterpart, exhibiting a significantly higher LRS/HRS current ratio and overall enhanced current levels.

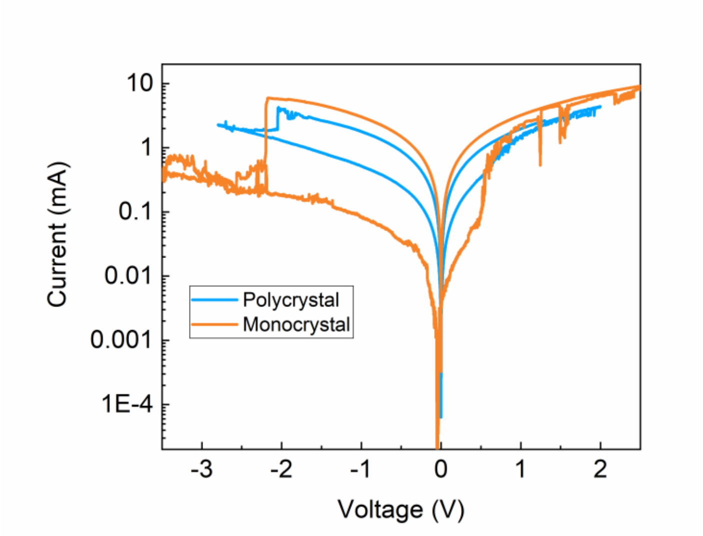

Figure 36: Comparison of cyclic voltammetry (CV) curves for the monocrystalline (orange curve) and polycrystalline (blue curve) $MAPbBr_3$ memristor devices.

One of the most critical challenges in the development of perovskite-based memristors is achieving high endurance while preserving their excellent performance characteristics within a simple device architecture. Endurance refers to the capability of a memristor to undergo repeated resistive switching cycles without experiencing significant degradation or performance loss. This parameter is crucial, as continual cycling can trigger a range of physical effects, including electromigration, thermal stress, material fatigue, and overall structural degradation[257], that may alter the device’s resistance or conductance, ultimately leading to instability in its switching behavior or complete failure.

Figure 35b presents the endurance test, performed through a sequence of voltage steps: +0.1 V → +1 V → +0.1 V → −2.5 V, where +0.1 V serves as the reading voltage, +1 V as the set voltage, and −2.5 V as the reset voltage. The current is measured at +0.1 V while alternating between the HRS and LRS. During the initial 250 seconds, the HRS current increases from 0.1 to 0.3 mA. Subsequently, the HRS current decreases and exhibits greater variability, fluctuating between

0.01 and 0.1 mA. The LRS/HRS current ratio varies from approximately 10 (in the first 250 s) to 80 for the remainder of the test. In contrast, the LRS remains highly stable throughout the 10^3 cycles, maintaining its current magnitude. These results are on par with some perovskite-based devices featuring more complex architectures[258].

Figure 35c shows the retention time test, where continuous current is monitored at +0.1 V for both resistance states: first the LRS (blue line), followed by the HRS (orange line), over a period of 10^4 seconds. The HRS current initially increases from 50 to 80 μA within the first 500 s and remains stable at 80 μA for the rest of the measurement. Meanwhile, the LRS current exhibits exceptional stability along the entire test. The resulting LRS/HRS ratio of approximately 25 further supports the device's reliable memory performance[259].

Finally, Figure 35d illustrates the resistance switching behavior, with a sharp transition from HRS to LRS occurring at approximately +0.5 V and the reverse transition (RESET) at −2.0 V. The slope closes to unit indicates a rapid transition between resistive states, as expected for high-performance memory devices[260]. Additionally, Figure 37 shows the time response for the HRS-to-LRS transition, measured at 15 ms. To the best of our knowledge, response time is rarely reported for MHP memristors, limiting the possibility for direct comparison.

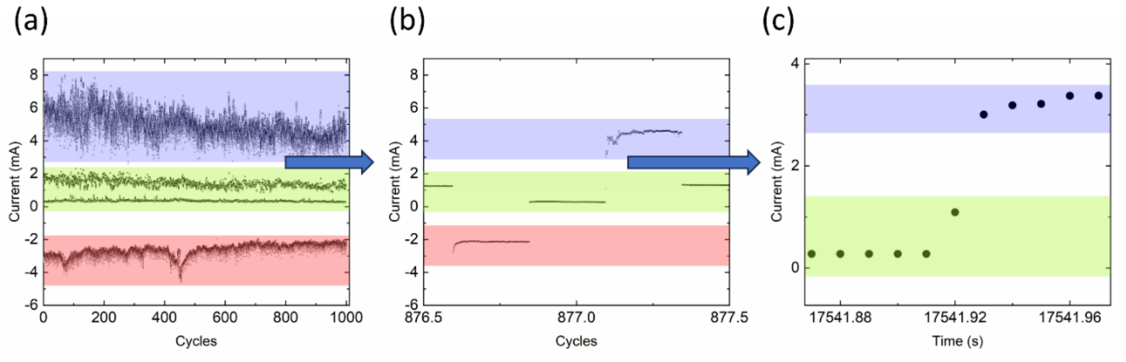

Figure 37: (a) Endurance test over 10^3 switching cycles for a representative $MAPbBr_3$ TSC memristor device. (b) Zoomed view of cycle 877. (c) Time-resolved measurement of cycle 877, showing the transition from the LRS at the read voltage to the LRS state under a fixed voltage of 1 V. The red, blue, and red-shaded regions indicate the HRS, LRS, and read voltage intervals, respectively.

4.3.3 Impedance Spectroscopy Characterization of the Electroforming Process

As previously discussed, memristive devices undergo resistive switching through an electroforming process in which a conductive pathway is established within the perovskite layer, resulting in the transition to the low-resistance state. Gaining insight into this process is essential for understanding the parameters that govern switching kinetics, endurance, and retention times, key factors for unlocking the full potential of perovskite memristors in memory and computing technologies. However, deciphering this mechanism is particularly challenging due to the complex interaction between ionic and electronic processes, which occur on different time scales[133], [137], [250], [261].

Despite these complexities, two principal switching mechanisms have been proposed in the literature: (i) the electrochemical metallization mechanism (ECM), which involves the migration of metal cations, and (ii) the valence change mechanism (VCM), which relies on the formation and movement of halide vacancies. In the context of halide perovskite-based memristors, the change in conductivity may thus arise from either migrating metal ions ECM) or halide vacancy dynamics (VCM)[126], [132], [132].

IS involves the measurement of the I-V response of a device at a fixed steady-state potential (V_{dc}), superimposed with a small AC perturbation (V_{ac}) over a range of frequencies (ω). The resulting data are expressed as the complex impedance exhibited by the system in response to the frequency-dependent perturbation. Interpretation of these results is typically carried out by fitting the experimental spectra to an appropriate equivalent circuit model.

In MHP devices, the capacitance observed in IS measurements, particularly in the low-frequency regime[262], [263], is closely linked to the type of I-V hysteresis displayed. This hysteresis can generally be classified as either normal (NH) or inverted (IH), with the latter characterized by higher current in the forward scan than in the reverse scan. IH behavior has been associated with the phenomenon of negative capacitance, a distinctive feature that also appears in certain neuronal system models[264], [265]. As such, IS emerges as a powerful tool for identifying and distinguishing the electrochemical processes occurring during the HRS and LRS states.

IS can also be employed to probe the electroforming stage by applying incremental V_{dc} values, effectively reconstructing an I-V curve from low to high bias conditions. When applied to a pristine, untreated device, voltage is gradually increased from 0 to 4.5 V. The corresponding Nyquist plots reveal a single arc in the high- and intermediate-frequency (HF, IF) regions, typically attributed to bulk-related processes, and a distinctive loop directed toward the fourth quadrant at low frequencies (LF). This reduction of Im(Z) to values below zero is can be observed in various halide perovskite device configurations, both in experimental studies and in drift-diffusion simulations[266], [267].

This behavior is often referred to as an "inductive loop" or manifestation of "negative capacitance,"[268] and can be represented in circuit models using a chemical inductor element[269], [270]. Unlike classical electromagnetic inductance, which primarily influences the high-frequency region of the impedance spectrum, this chemical inductive effect arises from the interaction between charge carriers and ionic species moving at different time scales. The resulting dynamic mismatch can delay the system's electrical response and modulate charge injection at the electrode interfaces[75], [269].

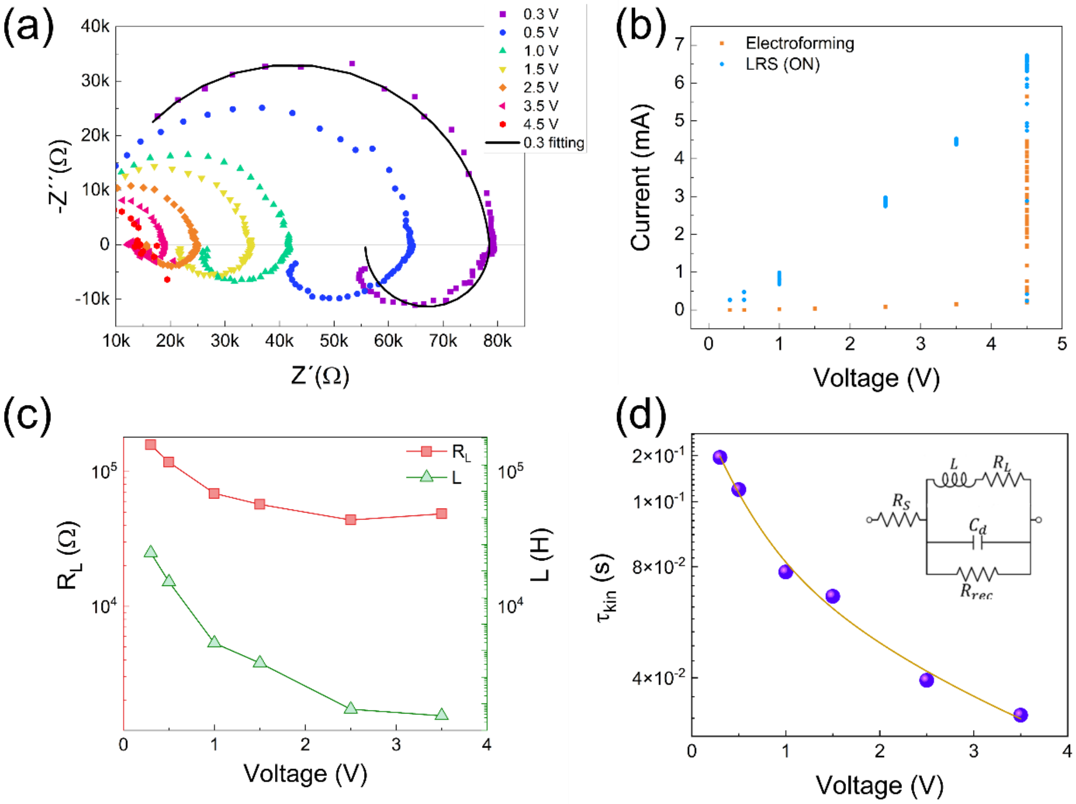

Figure 38. (a) Impedance spectra illustrating the evolution of the device response under

increasing applied bias, leading to the electroforming process. For clarity, only the fitting at 0.3 V is shown. (b) Corresponding DC current values recorded during the electroforming process (orange dots) and after reaching the low-resistance state (LRS, blue dots). (c) Quantification of the R_L and L components obtained from equivalent circuit fitting (circuit shown in the inset of panel d) using the surface polarization model (SPM)[75]. (d) Kinetic relaxation times (τ_{kin}) extracted from the negative capacitance features observed during the electroforming process.

A clear evolution in the impedance response is observed with increasing applied V_{dc}, as shown in figure 38a. As the bias voltage rises, both the high-frequency semicircles and the low-frequency inductive features progressively decrease, ultimately leading to a more distorted impedance spectrum at 4.5 V. To ensure the stability of the sample throughout the IS measurements, the corresponding I_{dc} values were simultaneously recorded.

Figure 38b displays the evolution of I_{dc}. Starting from approximately 10^{-6} A at low V_{dc}, the current increases linearly, reaching values on the order of 10^{-3} A as the voltage approaches 4.5 V. This pronounced increase, highlighted by the orange data points in figure 38b, confirms that the electroforming process is actively occurring during the impedance measurement. The combination of a current rise exceeding two orders of magnitude and the accompanying changes in the impedance spectra provides strong evidence for the onset of the ON state or LRS in the device.

Figure 38b illustrates an initial I_{dc} current of approximately 10^{-6} A under low V_{dc} conditions, followed by a linear increase as the applied voltage rises, reaching around 10^{-3} A as the bias approaches 4.5 V. This behavior, particularly highlighted by the orange data points in the figure, provides direct evidence that the electroforming process is taking place during the impedance measurement. The increase in current by more than two orders of magnitude, coupled with the concurrent evolution of the impedance spectra, strongly indicates the initiation of a conductive mechanism associated with the transition to the ON state or low-resistance state.

Subsequently, the applied bias was decreased from 4.5 V to 0 V. During this voltage sweep, the I_{dc} remains in the milliampere range across all V_{dc} values (blue points in figure 38b), indicating that the device persists in the LRS. The presence of an inductive component in the impedance spectra leads to a slow kinetic time constant, τ_{kin} (see below for further details), which offers insight into ionic motion within the LF domain. Figure 38c, exhibits the R_L and L values obtained during the IS at different voltages. Both, R_L and L tend to decrease as the applied voltage increases.

To analyze this behavior, the impedance data were fitted using the equivalent circuit (EC) model shown in the inset of figure 38d, which includes an R_L–L elements (displayed in figure 38c) used to extract τ_{kin}. Recent studies have highlighted the value of this approach for elucidating the behavior of MHP-based memristors, proposing a generalized "neuron-inspired" model that incorporates a slow time constant largely independent of the applied voltage[270], [271], [272].

In our analysis, the calculated τ_{kin} decreases as the applied bias increases, revealing that the electroforming process is associated with a shift in the characteristic timescale, from approximately 10^{-1} s to 10^{-2} s, as the LRS is established. These time constants are consistent with mechanisms such as ionic accumulation and halide vacancy diffusion, respectively, as previously documented in the literature[273]. This suggests that electroforming is initiated by the gradual accumulation of ionic species, which subsequently transitions to faster ionic diffusion processes. A comparable sequence of events has been reported in memristors based on metal oxides, supporting the hypothesis that similar physical mechanisms may be at play here, as evidenced by our IS data[274].

This finding not only reinforces the critical role of ionic dynamics in the operation of perovskite memristors but also represents, to the best of our knowledge, the first in situ observation of the electroforming process via impedance spectroscopy.

R_L-L line effect on the functioning of the EC established by the SPM:

In conventional electronic circuits, an inductor typically consists of a coiled wire that generates a magnetic field in response to changes in voltage, thereby opposing variations in the electric current. This opposition, known as inductance, is denoted by the symbol L.

In the present model, a similar effect arises from surface ionic accumulation, which introduces a temporal delay analogous to the inductive response observed in classical systems. This delay, governed by the kinetic relaxation time (τ_{kin}), manifests as low-frequency arcs and negative capacitance in the impedance spectrum, effectively represented by an equivalent inductive element.

The AC impedance response associated with this model can be mathematically described by the following expression:

$$Z = \frac{\hat{\mathrm{V}}}{\hat{\mathrm{j}}} = \left[\mathrm{i}\omega C_d + \frac{1}{R_L + \mathrm{i}\omega \mathrm{L}} + \frac{1}{R_L} + \frac{1}{R_C - \frac{1}{\mathrm{i}\omega C_1}} \right] \qquad \text{Equation 9}$$

$$R_{rec} = \frac{\beta K_B \mathrm{T}}{q j_{rec}} \qquad \text{Equation 10}$$

$$R_L = \frac{\gamma K_B \mathrm{T}}{q j_{rec}} \qquad \text{Equation 11}$$

$$L = \frac{R_L}{\tau_{kin}} \qquad \text{Equation 12}$$

$$R_c = \frac{b \tau_{kin}}{C_1} \qquad \text{Equation 13}$$

Here j_{rec} represent the recombination current at steady state, β and γ exponents are constants with values ≤ 1 and *b* parameter serves a correction factor for the fitting, and $k_B T$ denotes the thermal energy.

4.4 Conclusions

In this work, we report the successful fabrication of the first TSC perovskite memristor, effectively integrating the beneficial properties of both monocrystalline materials and polycrystalline thin-film perovskites. Utilizing a CITC approach, with ITO and PTAA serving as bottom electrodes and a graphite spray as the top contact, we developed a highly stable memristive device exhibiting outstanding performance. The resulting device achieved an LRS/HRS current ratio of approximately 10 and demonstrated endurance over 10^3 switching cycles, positioning it among the most robust perovskite-based memristors reported to date. Its operational stability under ambient conditions, without requiring encapsulation, enabled detailed impedance spectroscopy studies. Importantly, we were able to monitor the electroforming process in situ, providing valuable insights into the switching mechanism that governs the behavior of perovskite memristive systems.

By quantitatively analyzing the evolution of the kinetic time constant (τ_{kin}) associated with the low-frequency impedance response, we identified significant changes in ionic motion occurring during the electroforming process. These modifications correlate with a three-order-of-magnitude increase in current, highlighting the dynamic transformation of the device's internal conduction state. The observed decrease in τ_{kin} indicates a transition from slower to faster processes, which can be attributed to a shift from ionic accumulation to diffusion-driven dynamics. These insights offer a meaningful contribution to the fundamental understanding of resistive switching mechanisms in perovskite-based memristors. Furthermore, the fabrication strategy presented here provides a straightforward and scalable route for producing efficient and highly reliable perovskite memristive devices.

Overall, this study represents a substantial advancement in the field of perovskite memristor technology, paving the way for the development of high-performance and stable devices suited for next-generation memory and neuromorphic computing applications.

Chapter 5

Compositional Engineering of Monocrystalline Metal Halide Perovskite Memristors for Multistate Non-Volatile Operation

Chapter 5 is an extension of the previous Chapter 3 by offering a broader study in perovskite TSC-based memristors. In particular, various compositionally engineered devices are fabricated, focusing on the influence of different halides and mixed-halide compositions on memristor performance. The findings presented in this chapter are derived from and aligned with those reported in an article currently in under revision.

Abstract

MHP memristors hold great promise for next-generation memory and neuromorphic computing. However, challenges such as stability and endurance hinder both their performance and a deeper understanding of their working mechanisms. Advances in thin TSC-MHP memristors have demonstrated improved endurance due to absence of grain boundaries, which make them an ideal platform for systematically identifying key factors influencing device performance. Thus, evaluating the compositional effect on TSC-MHP memristors using a consistent device architecture demonstrates significant potential for enabling the development of application-oriented devices. In particular, this approach is used to fabricate the first memristor based on a mixed-halide thin perovskite TSC, which enable multistate non-volatile memristive operation. Furthermore, precise compositional engineering allows control over defect density, that affects the materials' ionic properties and determines key device performance parameters. This study unlocks multistate properties in non-volatile memristors and provides critical insights into defect density effects, paving the way for long-term storage in neuromorphic computing.

5.1 Introduction

As explained in chapter 1, the increasing demand for data computing and the associated power consumption highlight the necessity to explore new technologies utilizing innovative materials that can overcome additional challenges such as the von Neumann bottleneck or the Moore's law limitations[275], [276]. In this scenario, MHPs emerge as promising candidates to tackle these questions, due to the significant potential of these materials in advancing the next generation of data computing[277].

Resistive switching memory devices, also known as *memristors*, are inspired by neural synapses and are being explored as a foundation for next-generation computing technologies[282].In these systems, information is typically encoded through transitions between a high resistance state and a low resistance state induced by an external voltage stimulus Among their most promising applications is the development of ReRAMs, which offer non-volatile data storage capabilities, retaining information even when powered off[283], [284].

Beyond binary switching, ReRAMs are also capable of operating in multistate mode, where devices can exhibit multiple stable resistance levels rather than just two. These multistate memristors are particularly attractive because they allow for higher data storage density and the implementation of analog (multistate) signal processing, essential for emerging paradigms such as neuromorphic computing[283], [285]. In such systems, the gradual modulation of resistance states can emulate synaptic weight changes, supporting more sophisticated and energy-efficient learning algorithms[285], [286]. However, few multistate ReRAM devices based on perovskite materials have been reported, and the mechanisms underlying multistate behavior in such devices are still not fully understood[287], [288].

The excellent synergy between the requirements for ideal resistive switching memory devices and the MHPs properties, strongly defined by their ionic mobility, positions this material family as a highly promising platform for next-generation resistive switching technologies. Since the first reports of resistive switching behavior in MHP-based memristors, ReRAM devices using MHPs have shown remarkable progress in both performance and versatility, confirming their potential in advanced memory applications[282]. Several formulations of MHPs, including polycrystalline films, nanocrystals, and thin monocrystals, have been explored to optimize the device performance. Each of these systems presents unique complexities, and the limited understanding of the fundamental processes that drive resistive switching behavior in MHPs remains a significant hurdle in their development. Due to the intricate ionic-electronic dynamics involved, the exact mechanisms of RS are still under debate[289], [290]. As is explained in the pervious chapter, current literature primarily discusses two mechanisms: the ECM, driven by metal cations[291], and the VCM, which relies on halide vacancies[292]. While conclusive evidence for either mechanism is still pending, advancing our understanding of these processes is likely essential for the progress of multistate device technology. Additional challenges arise from the inherent characteristics of MHPs and the unique properties of each system. Notably, material instability presents critical issues that directly impact essential parameters like the endurance of resistive switching devices. For instance, PC-MHPs offer scalability but are susceptible to degradation at grain boundaries[293], while nanocrystals provide enhanced tunability but suffer from increased surface reactivity[294], adding further sources of instability. Alternatively, TSC perovskites have demonstrated to enhance memristor endurance and stability by reducing grain boundaries and defects[283], making TSC materials an ideal approach to developing memristors despite the most precise synthesis conditions.

In chapter 4 we demonstrated that, due to suppression of grain boundaries, the use of $MAPbBr_3$ TSC to fabricate memristors can also increase key performance parameters such as LRS/HRS ratio or endurance[283] respect to PC counterpart. Moreover, the robustness of the TSC enabled us to successfully monitoring of the electroforming process using IS, allowing *in-situ* observation of species movement within the material, marking the first time direct tracking of this phenomenon during the electroforming process. In this way, the ionic and electronic dynamics were thoroughly investigated, enhancing the understanding of memristive behaviors in these systems[283].

In this work, we perform a comprehensive comparison of three TSC single-halide MHP using a consistent device architecture. This systematic analysis is carried out due to the lack of such direct comparisons in the literature, with the goal of identifying which halide composition provides the most favorable properties for memristive applications. Additionally, we extend our analysis by developing TSC memristors with mixed halide perovskites to better understand how halide composition influences memristor properties. We confirm that different halide compositions in TSC forms can serve as a tool to modulate defect density within the material[295], [296], directly impacting the mobility of vacancies and ions, as previously reported[297], [298]. Here, we demonstrate that defect density directly affects the key properties of memristor devices. Key performance parameters, such as LRS/HRS ratio and endurance, can be significantly improved by reducing defect density in the active material. Notably, our results suggest that the emergence of multistate behavior in ReRAM memristors is directly influenced by the defect density in MHPs, in conjunction with the effects introduced by mixed-halide compositions, paving the way for a new generation of memristors with high-density data storage and neuromorphic processing capabilities.

5.2 Experimental section

Materials: Lead chloride ($PbCl_2$), lead bromide ($PbBr_2$) and lead iodine (PbI_2) were purchased from TCI. Methylammonium chloride (CH_3NH_3Cl, MACl), methylammonium bromide (CH_3NH_3Br, MABr) and methylammonium iodine (CH_3NH_3I, MAI) was purchased from GreatCell. PTAA was purchased from Ossila. DMF and DMSO were purchased from Thermo Scientific. GBL was purchased from TCI. Toluene was purchased from VWR. Graphite spray was purchased from RS. All the reagents were directly used without any further purification.

Device fabrication process:

TSC memristor devices: The precursor solutions for 1 M $MAPbX_3$ (X=Cl, Br, I) perovskites were prepared by dissolving a 1:1 molar ratio of PbX_2 and MAX in an appropriate solvent. For the $MAPbCl_3$ precursor solution, the precursors $PbCl_2$ and MACl were solved by DMF:DMSO (1:1, vol:vol), followed by vigorous shaking to ensure complete dissolution. The $MAPbBr_3$ precursor solution was prepared by dissolving $PbBr_2$ and MABr in vigorous shaking. Similarly, the $MAPbI_3$ precursor solution was prepared by dissolving PbI_2 and MAI in GBL under the same shaking conditions. The $MAPb(Br_{0.8}Cl_{0.2})_3$ precursor solution was prepared by mixing the pure solutions $MAPbCl_3$:$MAPbBr_3$ in a 1:4 volume ratio. The $MAPb(Br_{0.9}I_{0.1})_3$ precursor solution was prepared by mixing the pure solutions of $MAPbI_3$:$MAPbBr_3$ in a 1:4 volume ratio. All the solutions were filtrated using 0.2 μm PTFE syringe filter before deposition.

Glass/ITO substrates were cleaned sequentially using acetone, detergent, deionized water, and absolute ethanol, with each step performed in an ultrasonic bath for 10 min. After drying with air flow, the substrates were treated in a UV-O_3 cleaner for 20 min. Subsequently, 40 μL of the prepared PTAA solution (2mg mL^{-1} solved in toluene) was deposited onto the ITO substrate by spin-coater at 4000 rpm for 30 s under room conditions. Immediately, the substrates were annealed at 100 °C for 10 min.

The space-confined inverse temperature crystallization method was used for growing thin monocrystals. The temperature was gradually increased from 25 to 80 °C at a rate of 12 °C h^{-1} for the all the compositions except $MAPbI_3$. For $MAPbI_3$, the temperature ramp started from 50 ºC and increased to 120 ºC at a rate of 8 ºC h^{-1}. The substrates were held at 80 °C and 120 ºC, respectively for 24 h. After cooling at room temperature, the substrates were separated with a blade. Finally, the graphite electrodes were added on the top of the perovskite monocrystals by depositing 10 µL of the graphite solution with a micropipette. The solution evaporates in 60 s after deposition, approximately, forming a solid graphite that acts as an electrode. It is important to underline that the device is fabricated outside of the glovebox.

Polycrystal memristor devices: All solutions used for the preparation of polycrystalline perovskites are the same as those used for the synthesis of monocrystal perovskites. The solutions were added to the ITO substrates treated with PTAA, as previously described. Subsequently, the solutions were spinning with a ramp of 1000 rpm for 10 s and 4000 rpm for 40 s, adding 300 µL of toluene at 12 s of the second ramp for all the compositions except $MAPbI_3$, whose toluene addition time is 22 s. Then, the device is annealed for 30 min. Finally, the graphite electrodes were deposited on the $MAPbBr_3$. All the device experimental processes were fabricated inside of a glovebox.

Characterization: Profilometer measurements was performed with Dektak 150 Surface Profiler from Veeco equipment. The crystalline structure was assessed by a XRD collected on a Bruker D8 Advanced X-ray diffractometer with copper K_a radiation (1 = 1.5418 A˚) and a scan rate of 5 ° min^{-1} for 2θ angles ranging from 12º to 40º. EDX analysis were performed by an S-4800 instrument from HITACHI (Tokyo, Japan) operating at 10 kV. Electrical characterizations were measured using a Gamry inter-face 1010E. Photoluminescence measurements on the single crystals were carried out using an inverted microscope, Nikon (Tokyo, Japan) Ti2-U, equipped with a XY motorized stage. The emission signal was transmitted through optical fibers to an Edinburgh Instruments (Livingston, UK) FLS1100 spectrofluorometer, which was coupled to a cooled photomultiplier (PMT-980). The measurements were performed at room temperature, utilizing a 405 nm excitation wavelength provided by a picosecond (ps) laser diode incorporated into the microscope.

5.3 Results and Discussion

5.3.1 Structural and optical characterization

As in chapter 2 is mentioned, the confined inverse temperature crystallization method[299] is an effective approach to grow thin monocrystals. These TSC, with surface areas exceeding tens of square millimeters and thicknesses in the micrometer range, are ideal for fabricating devices where efficient charge extraction or injection is critical, such as solar cells or memristors[300], [301]. The control of the initial precursor solution, as detailed in the experimental section, enables the growth of $MAPbX_3$ monocrystals, where X refers to chloride, bromide and iodine, and two mixed halide perovskite compounds, $MAPb(Br_{0.8}Cl_{0.2})_3$ and $MAPb(Br_{0.9}I_{0.1})_3$. The lack of reports of TSC with such mixed halide compositions makes it essential to confirm their properties and structure. Special attention should be paid to ensuring that the halide ratio in the final materials accurately reflects the nominal composition.

XRD patterns of the prepared crystals, Figure 39a, show sharp and intense XRD reflections along (100) and (200) planes confirming the presence of a highly crystalline perovskite cubic phase in the case of $MAPbCl_3$ and $MAPbBr_3$. Regarding $MAPbI_3$, the abrupt reflections corresponding to the (200) and (400) planes confirm the high crystallinity of the samples[302], [303]. The (100) peak of $MAPb(Br_{0.8}Cl_{0.2})_3$ shifts by 0.2° to higher compared to $MAPbBr_3$, while the same peak in $MAPb(Br_{0.9}I_{0.1})_3$ shifts by 0.09° to smaller angles (inset Figure 39a). Such displacements are consistent with Vegard's law[304], [305]: substituting the smaller Br^- anion with the larger I^- anion expands the lattice constant, whereas replacing Br^- with the smaller Cl^- anion results in further contraction [306].

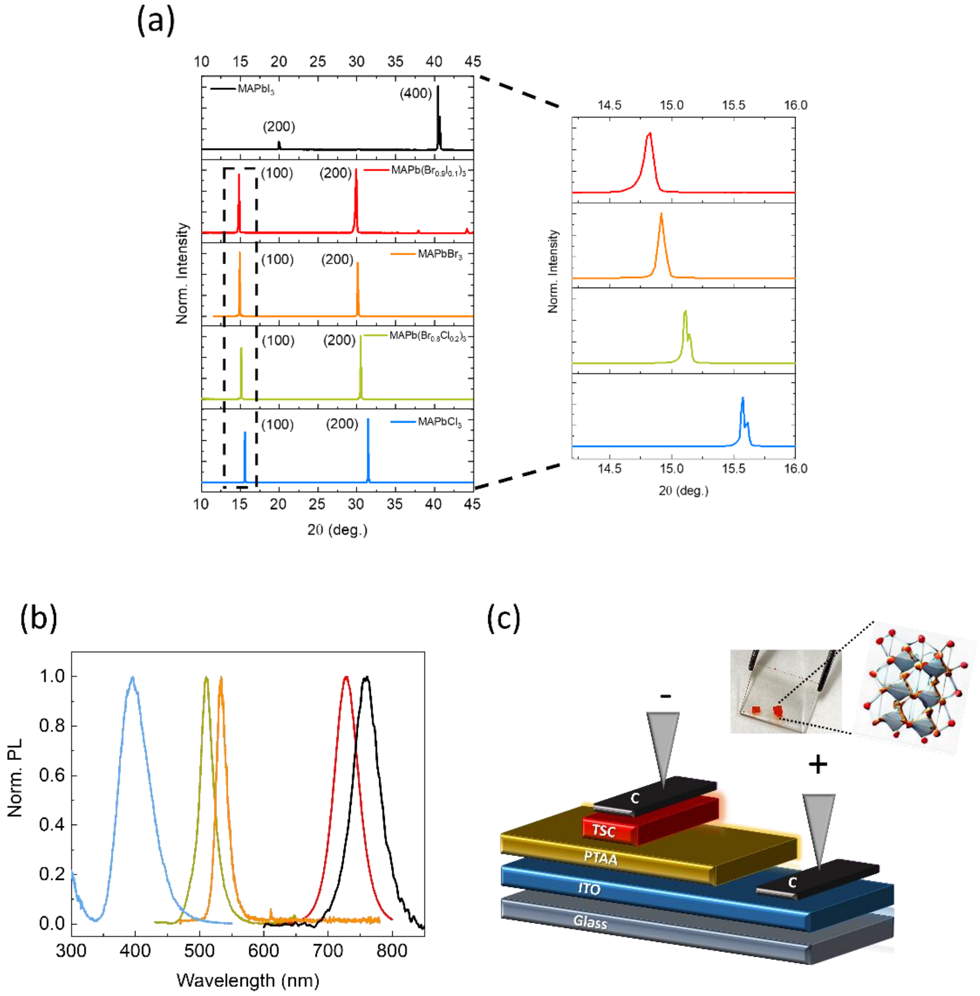

Figure 39: (a) XRD patterns, (b) PL emission of MAPbCl$_3$ (blue line), MAPbBr$_3$ (orange line), MAPbI$_3$ (black line), MAPb(Br$_{0.9}$I$_{0.1}$)$_3$ (red line), and MAPb(Br$_{0.8}$Cl$_{0.2}$)$_3$ (green line) TSC, and (c) Device architecture of perovskite memristor devices

Energy dispersive X-ray (EDX) analysis (Figure 40) confirms that the actual compositions are MAPb(Br$_{0.8}$Cl$_{0.2}$)$_3$ and MAPb(Br$_{0.9}$I$_{0.1}$)$_3$ which closely match their respective nominal compositions.

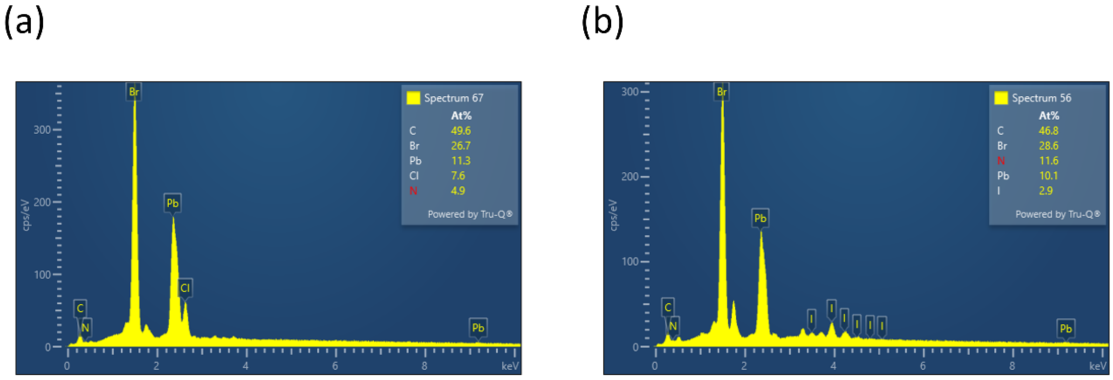

Figure 40: EDX analysis of (a) $MAPb(Br_{0.8}Cl_{0.2})_3$ and (b) $MAPb(Br_{0.9}I_{0.1})_3$ TSC perovskites.

The thickness of the different TSC is measured by profilometry, Figure 41, confirming a thickness of 20-25 µm in all the cases.

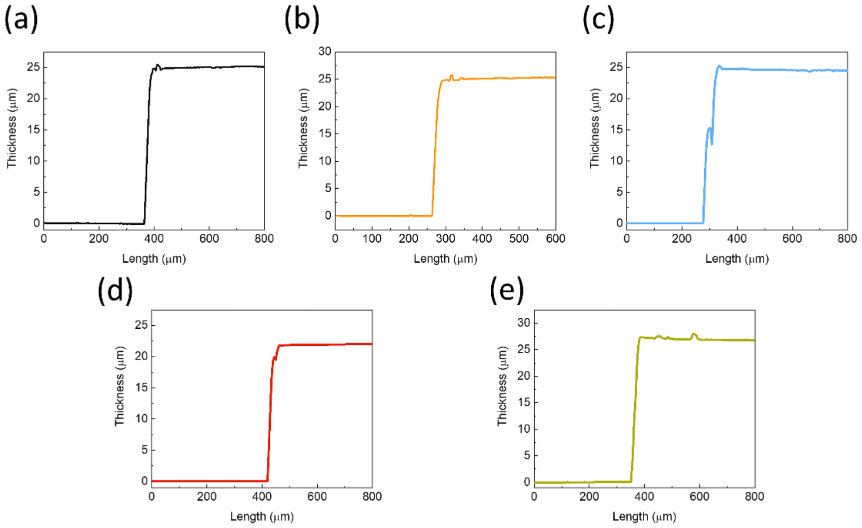

Figure 41: Profilometer measurements of (a) $MAPbCl_3$, (b) $MAPbBr_3$, (c) $MAPbI_3$, (d) $MAPb(Br_{0.9}I_{0.1})_3$, and (e) $MAPb(Br_{0.8}Cl_{0.2})_3$ TSCs.

PL (Figure 39b) can be used as a tool for evaluating qualitatively the optoelectrical quality and composition of the TSC. The pure halide compositions, $MAPbCl_3$, $MAPbBr_3$, and $MAPbI_3$, exhibit sharp and narrow emission peaks, with maximum emission wavelengths at 395 nm, 533 nm, and 760 nm, respectively, in accordance with previous literature reports[307], [308]. In contrast, the mixed halide TSC, $MAPb(Br_{0.9}I_{0.1})_3$ and $MAPb(Br_{0.8}Cl_{0.2})_3$, display maximum emission peaks at 510 nm and 728 nm, respectively. Notably, no phase segregation is observed during the measurements, which is a common issue in mixed halide compositions, particularly in their polycrystalline forms[309], [310], [311].

5.3.2 Characterization of monocrystalline pure halide memristor devices.

The TSC perovskites were implemented in memristor devices in a simple architecture, as represented in Figure 39c, where, PTAA, is selected as buffer layer, and graphite is used as low-reactive electrode. Due to their improved stability resulting from the suppression of grain boundaries, TSC perovskites are an ideal platform to accomplish high endurance memristor devices. This enables a more exhaustive analysis of the device's working mechanisms. Thus, here we extend the study to the different halides compositions to better understand the dynamics of the RS mechanisms.

Cyclic-voltammetry measurements of the pure halide memristors (see Figure 42a) were performed to compare the behavior of TSC based on different halides. The $MAPbCl_3$ memristor exhibited the highest set voltage (at which the device transitions from LRS to HRS) at 0.75 V, and the lower reset voltage (transition from HRS to LRS) at -1.1 V. In contrast, the $MAPbBr_3$ memristor showed a set voltage of 0.52 V and a reset voltage of -1.29 V. Similarly, the $MAPbI_3$ memristor demonstrated a set voltage of 0.43 V and a reset voltage of -1.34 V. It is worth remarking that the transitions from LRS to HRS (Figures 42a) occur abruptly for the three pure halide compositions, and no clear correlation is observed between the set/reset potentials and the materials' bandgap.

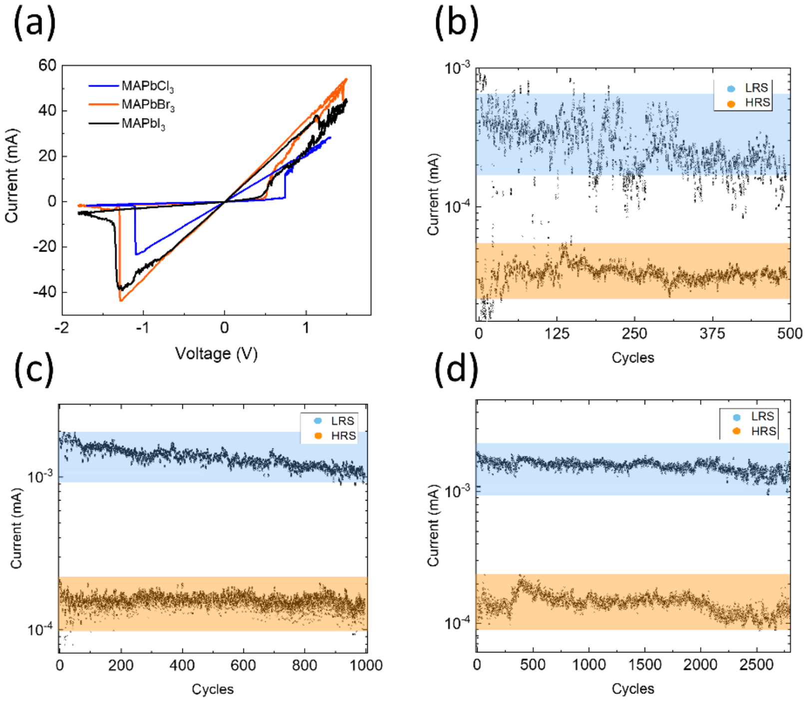

Figure 42: (a) Cyclic-voltammetry of $MAPbCl_3$ (blue line), $MAPbBr_3$ (orange line), $MAPbI_3$ (black line) TSC memristor devices. Endurance performance test conducted by applying cyclic sweep voltages in the sequence of +1.5 V, +0.07 V, −2 V, and +0.07 V on (b) $MAPbCl_3$, (c) $MAPbBr_3$, and (d) $MAPbI_3$ TSC memristor devices.

Additionally, an endurance test was conducted to examine the stability of the memristors. A sequence of voltage steps was applied in the following order: +1.5 V, +0.07 V, -2 V, and finally +0.07 V. Specifically, +0.07 V was used as the read voltage, +1.5 V as the set voltage, and -2 V as the reset voltage. Figure 42b presents the endurance test results for the $MAPbCl_3$ device. A significant dispersion in the LRS is clearly observed during the measurement, and the device eventually fails after 500 cycles. The LRS/HRS ratio remains close to 100 for the first 125 cycles, but gradually stabilizes at around 10 for the rest of the measurement. In contrast, the endurance analysis of $MAPbBr_3$ (see Figure 42c) shows no significant dispersion over 1000 cycles, maintaining an LRS/HRS ratio exceeding 10. The $MAPbI_3$ endurance test, displayed in Figure 42d, demonstrates one of the highest endurance values reported in the literature, with more than 2800 cycles without significant dispersion, and a stable LRS/HRS ratio above 10. Notably, the endurance performance varies significantly depending on the halide composition, with ~500 cycles for $MAPbCl_3$, ~1000 cycles for $MAPbBr_3$ and ~2800 cycles for $MAPbI_3$.

Long-term retention time of the LRS and the HRS is another key parameter for ReRAM devices, as this determines how long the device can reliably store information. To characterize retention times, a chronoamperometry is measured in which the current is continuously measured at +0.07 V, the read voltage, for both states, first the LRS and subsequently, the HRS along 10^4 s. The retention time analysis for $MAPbCl_3$ (Figure 43a) shows that the LRS/HRS ratio reaches 100 during the first 250 s. However, after this period, the current in the HRS increases from 10 μA to 100 μA, exhibiting high instability in the HRS. Nevertheless, the LRS remains stable throughout the measurement, achieving a retention time of 3000 s for Cl-based composition. In contrast, the $MAPbBr_3$ device (Figure 43b) demonstrates high stability in both LRS and HRS states throughout the entire measurement period of 10^4 s, maintaining an LRS/HRS ratio of 30. Similarly, the $MAPbI_3$ device (Figure 43c) exhibits a retention time of 10^4 s, with the HRS showing no significant fluctuations, while the LRS decreases slightly over time. Despite this minor variation, the LRS/HRS ratio remains consistently around 30 for the entire measurement duration.

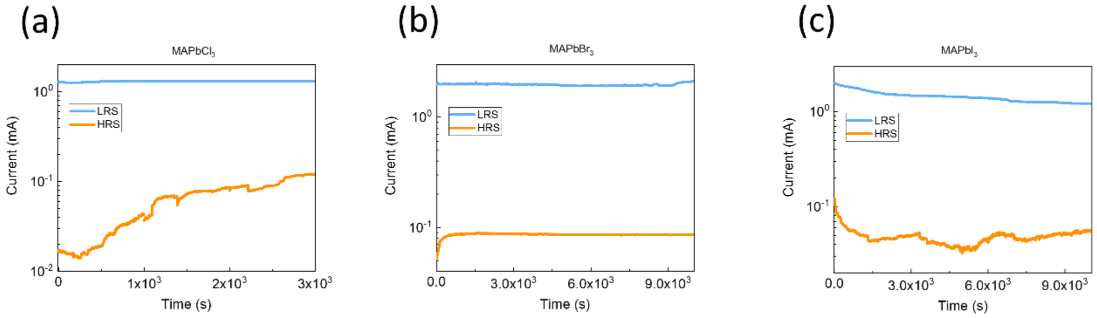

Figure 43: Chronoamperometry of (a) $MAPbCl_3$, (b) $MAPbBr_3$, and (c) $MAPbI_3$, where blue line corresponds to LRS, and orange line refer to HRS state.

5.3.3 Characterization of monocrystalline mixed halide memristor devices.

Memristors based on mixed halide perovskite TSC facilitate a deeper analysis of ionic-electronic dynamics and device mechanisms. The study focuses on $MAPb(Br_{0.9}I_{0.1})_3$ and $MAPb(Br_{0.8}Cl_{0.2})_3$ memristor devices. Figure 44a illustrates the performance of the $MAPb(Br_{0.9}I_{0.1})_3$ device during cyclic-voltammetry measurements, showing a set voltage of +0.55 V. Notably, the reset voltage transition is gradual, beginning at -1 V and progressing up to -2 V, at which the device fully transitions to the HRS. This gradual transition, unlike the abrupt switching observed in pure halide memristors (Figure 42a), enables the operation of multistate devices using mixed halide TSC perovskites. By selecting a reset voltage within the transition range, one can determine the HRS resistance, allowing for multiple resistance states.

Figure 44b displays a retention time test of the $MAPb(Br_{0.9}I_{0.1})_3$ device, where the read voltage is fixed to +0.07 V. The HRS obtained at -2 V, with a response of 0.2 mA. The LRS set by a +1.5 V and defined by a 2 mA response. Intermediate states are achieved when the reset voltage is set within the range of -2 V (corresponding to the HRS) and -1.1 V. Up to seven clearly differentiable states can be achieved by changing the reset voltages. The retention time reaches 500 s for each state, for a total retention time of 3500 s. Nevertheless, to assess the device's practical application, it is crucial to maintain the multistate configuration during endurance testing without any dispersion among the states. The dispersion in endurance measurements of a memristor causes variations in resistance states, leading to read errors and unreliable data processing. In neuromorphic computing, this variability can cause weight drift, affecting neural network performance, while in memory applications, it shortens device lifespan and requires error correction mechanisms to maintain reliability[312], [313].

The endurance test for the $MAPb(Br_{0.9}I_{0.1})_3$ device (see Figure 44c) was performed using a specific sequence of voltage steps, starting at set voltage of +1.5 V, followed by +0.07 V, then a reset voltage that varied between -2 V, -1.8 V, -1.5 V, -1.3 V and -1.1 V, and finally returning to the reading voltage of +0.07 V. For clarity, this sequence is visually represented in Figure 45: the sequence begins with a reset voltage of -2 V, followed by -1.8 V, and gradually decreases to -1.1 V. At this point, the entire sequence is repeated 30 times for each reset voltage. As shown in Figure 3b, up to six distinct states are achieved during 30 cycles for each voltage, resulting in a total of 150 cycles of stability. As is mentioned above, although seven states are achieved during retention test, the functional application is defined by six states without dispersion which is performed in the endurance test.

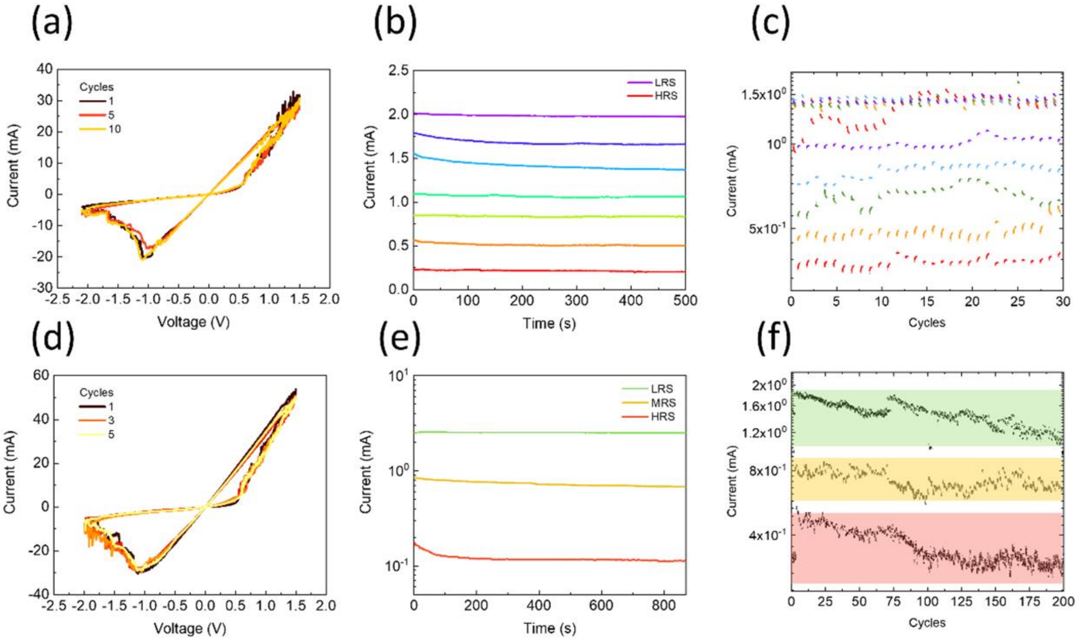

Figure 44: (a) Cyclic-voltammetry, (b) chronoamperometry, and (c) endurance test performance of the MAPb(Br$_{0.9}$I$_{0.1}$)$_3$ TSC memristor device. (d) Cyclic-voltammetry, (e) chronoamperometry, and (f) endurance test performance of the MAPb(Br$_{0.8}$Cl$_{0.2}$)$_3$ TSC memristor device.

The cyclic-voltammetry of the MAPb(Br$_{0.8}$Cl$_{0.2}$)$_3$ device (Figure 44d) is similar to MAPb(Br$_{0.9}$I$_{0.1}$)$_3$. The set voltage occurs at +0.55 V and the reset voltage ranges between -1 V and -2 V, when the device fully reaches the HRS. Figure 44e displays the retention time for three different states obtained within that range where the read voltage is +0.07 V. The three states remain stable for 900 s each one with an LRS/HRS ratio of 30 between the extremes. The endurance test (see Figure 44f) was performed using a specific sequence of voltage steps, starting at a set voltage of +1.5 V, followed by a read voltage of +0.07 V, then a reset voltage that varied between -2 V and -1.5 V, and finally returning to +0.07 V. In the case of MAPb(Br$_{0.8}$Cl$_{0.2}$)$_3$ devices, three different states can be achieved reaching 200 cycles for each one.

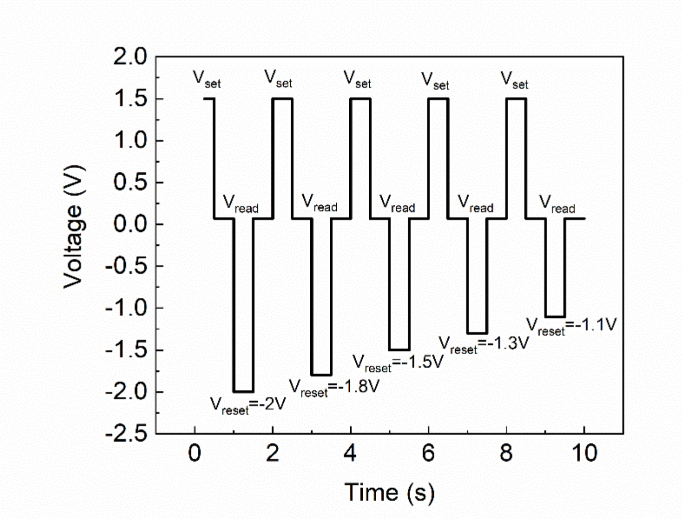

Figure 45. Endurance sequence of the multistate setup for $MAPb(Br_{0.9}I_{0.1})_3$ memristor.

While the three states are completely differentiable, the high dispersion observed during the endurance cycles prevents the achievement of additional states, as observed in $MAPb(Br_{0.9} I_{0..1})_3$ device. Up to 9 states can be distinguishable in the retention test for $MAPb(Br_{0.8}Cl_{0.2})_3$, Figure 46, but these must be differentiated along an endurance test to enable a functional multistate device, as mentioned above.

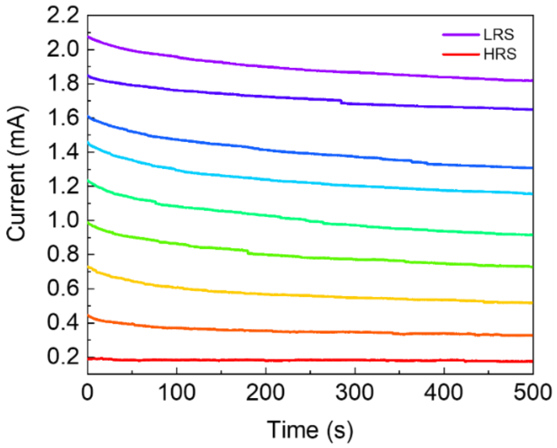

Figure 46. Multistate chronoamperometry of $MAPb(Br_{0.8}Cl_{0.2})_3$ memristor device, transitioning from HRS (red line) to LRS (purple line), with intermediate states representing transitional colors.

5.4 Switching Mechanism.

With these results, the use of mixed halide perovskite TSC devices instead of pure halide ones, unlocks new potential for the fabrication of multistate memristor devices. Considering this comprehensive range of compositions, the relation between the defect density of each perovskite and the dynamics of the memristive mechanism can be used to gain insights on their working mechanisms. Here, it is worth highlighting that a low-reactivity electrode such as graphite is used to mitigate the role of the electrode in the operation of the device. Moreover, the devices can be operated without such electrode, with a direct contact from the measuring tip on the surface, see the cyclic voltammetry shown in Figure 47. There are no qualitative changes in the behavior of the device when graphite is not used. This fact discards the relevant role of graphite in memristive behavior.

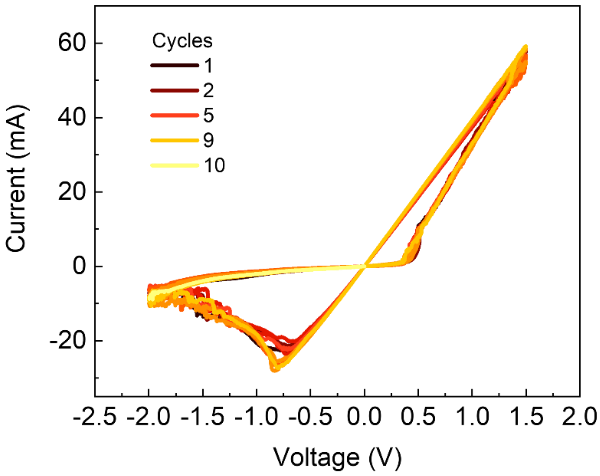

Figure 47. Cyclic-voltammetry of $MAPb(Br_{0.8}Cl_{0.2})_3$ memristor device without graphite as top electrode.

The SCLC regime of hole-only devices was measured for all analyzed monocrystalline perovskite compositions (Figure 48) and compared to their polycrystalline counterparts (Figure 49).

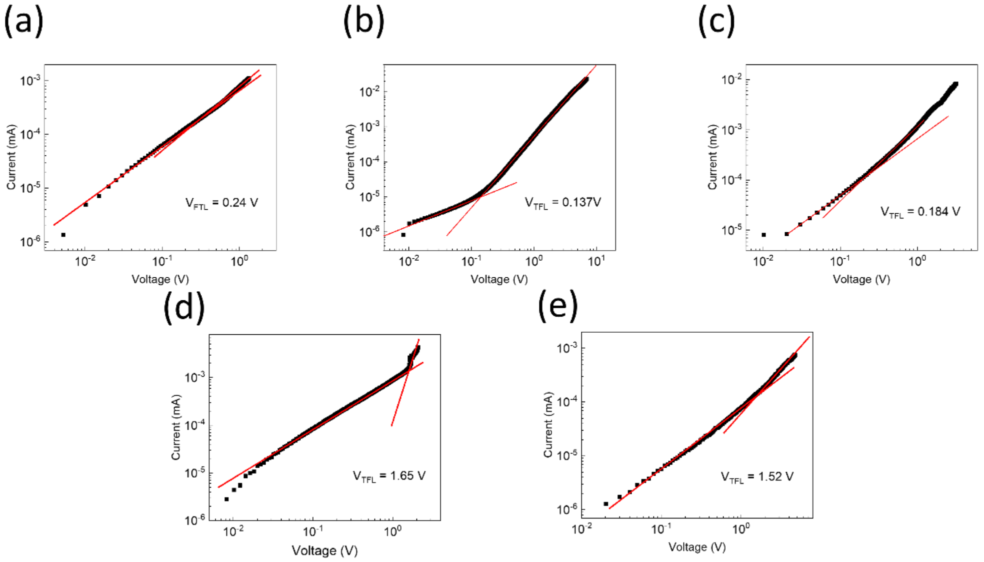

Figure 48. Space-charge limited current measurement of (a) $MAPbCl_3$, (b) $MAPbBr_3$, (c) $MAPbI_3$, (d) $MAPb(Br_{0.8}Cl_{0.2})_3$, and (e) $MAPb(Br_{0.9}I_{0.1})_3$monocrystal memristor devices.

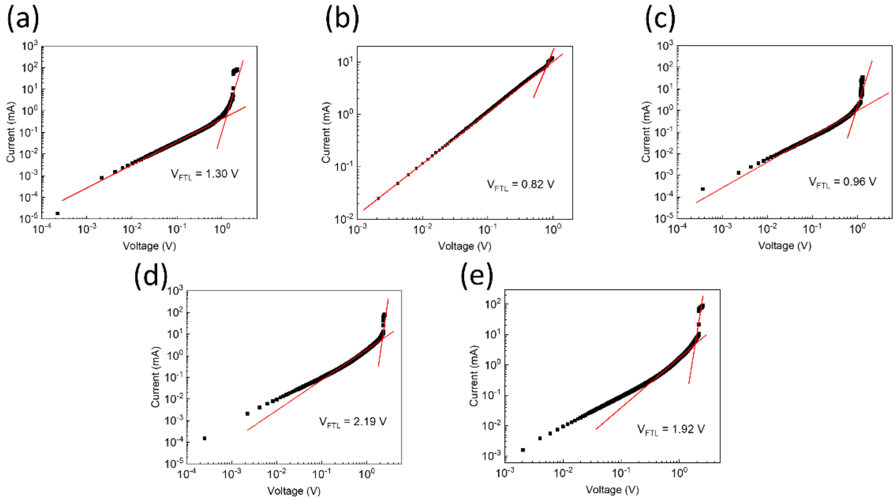

Figure 49. Space-charge limited current measurement of (a) $MAPbCl_3$, (b) $MAPbBr_3$, (c) $MAPbI_3$, (d) $MAPb(Br_{0.8}Cl_{0.2})_3$, and (e) $MAPb(Br_{0.9}I_{0.1})_3$ polycrystal memristor devices.

SCLC measurement was conducted using a symmetric sandwiched structure, using PTAA as selective layer, while avoiding graphite as the contact electrode. The most common approach to determine the trap density based on the so-called trap-limit voltage, see equation 5[314], [315]:

The obtained values for the monocrystal and polycrystal devices are summarized in table 2 and table 3, respectively, and represented in Figure 50a.

Table 2. Calculation of defect density for monocrystal memristor devices. The V_{FTL} is extracted from the SCLC measurement.

Monocrystal	$MAPbCl_3$	$MAPb(Br_{0.8}Cl_{0.2})_3$	$MAPbBr_3$	$MAPb(Br_{0.9}I_{0.1})_3$	$MAPbI_3$
L (µm)	27	26.6	24.7	21.9	2.50
ε	23.9	25	25.5	25	18
V_{FTL} (V)	0.24	1.65	0.137	1.52	0.184
n_t	$8.72 \cdot 10^{11}$	$6.44 \cdot 10^{12}$	$6.33 \cdot 10^{11}$	$8.76 \cdot 10^{12}$	$5.86 \cdot 10^{11}$

Table 3. Calculation of defect density for polycrystal memristor devices. The V_{FTL} is extracted from the SCLC measurement.

Polycrystal	$MAPbCl_3$	$MAPb(Br_{0.8}Cl_{0.2})_3$	$MAPbBr_3$	$MAPb(Br_{0.9}I_{0.1})_3$	$MAPbI_3$
L (µm)	450	505	500	512	458
ε	23.9	25	25.5	25	18
V_{FTL} (V)	1.3	2.18	0.82	1.92	0.96
n_t	$1.70 \cdot 10^{16}$	$2.36 \cdot 10^{16}$	$9.25 \cdot 10^{15}$	$2.12 \cdot 10^{16}$	$9.34 \cdot 10^{15}$

In the case of TSC devices, the use of mixed halide compositions (10^{13} cm^{-3}) increases one order of magnitude the defect density compared to pure halide memristors (10^{12} cm^{-3}). Regarding PC devices, their defects density are around 10^{16} cm^{-3} for the single halide compositions, and the mixed halide compositions exhibit values slightly higher, yet within the same order of magnitude, figure 50a. All the defect density values of PC perovskite and pure halide TSC perovskite are in agreement with those reported in the literature[316]. Mixed halide perovskite TSC have been studied far less extensively, and our results suggest that incorporating mixed halides may increase the defect density in these materials[298].

Defect density plays a crucial role in determining the ionic properties of SCs. Therefore, it is important to assess its impact on key parameters of memristive devices. Figure 50b displays the reset voltage of the TSC memristive devices as a function of the materials' defect density. $MAPbI_3$ exhibits the lower defect density and the most negative reset voltage of the pure halide devices. $MAPbBr_3$ displays marginally more defect density and lower reset voltage than $MAPbI_3$. Following that trend, $MAPbCl_3$ presents slightly higher defect density, and also the lowest reset voltage compared to pure halide devices. As mentioned above, memristive devices based on mixed halide TSC compositions show a gradual reset. In both cases, the reset voltage start approximately at -1 V and finishes at -2 V, although $MAPb(Br_{0.8}Cl_{0.2})_3$ exhibits slightly lower defect density than MAPb($Br_{0.9}I_{0.1}$)$_3$ composition. We tentatively relate the gradual reset to the higher defect density, almost one order of magnitude compared to single halide TSC devices.

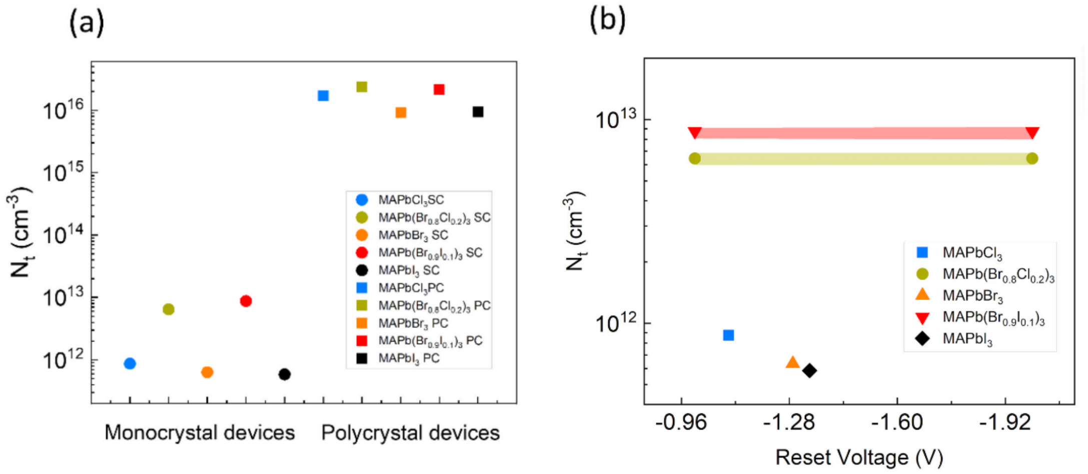

Figure 50: (a) Defect density of TSC (circle points) and PC (square points) memristor devices. (b) Reset voltage dependence of TSC devices respect to defect density.

Figure 51 compares the TSC devices' cyclic voltammetry with their PC counterpart. Remarkably, the HRS in PC devices is close to the LRS in all cases of TSC devices, exhibiting an LRS/HRS ratio of 2 for the PC memristors, contrasting with a ratio of 30 of TSC devices. A clear correlation between high LRS/HRS ratio and low defect density is evident when comparing the performance of TSC and PC devices. Lower defect densities of TSC translates to an LRS/HRS of ~10. In contrast, polycrystalline devices, with four orders of magnitude higher defect densities, present an LRS/HRS ratio of 2.

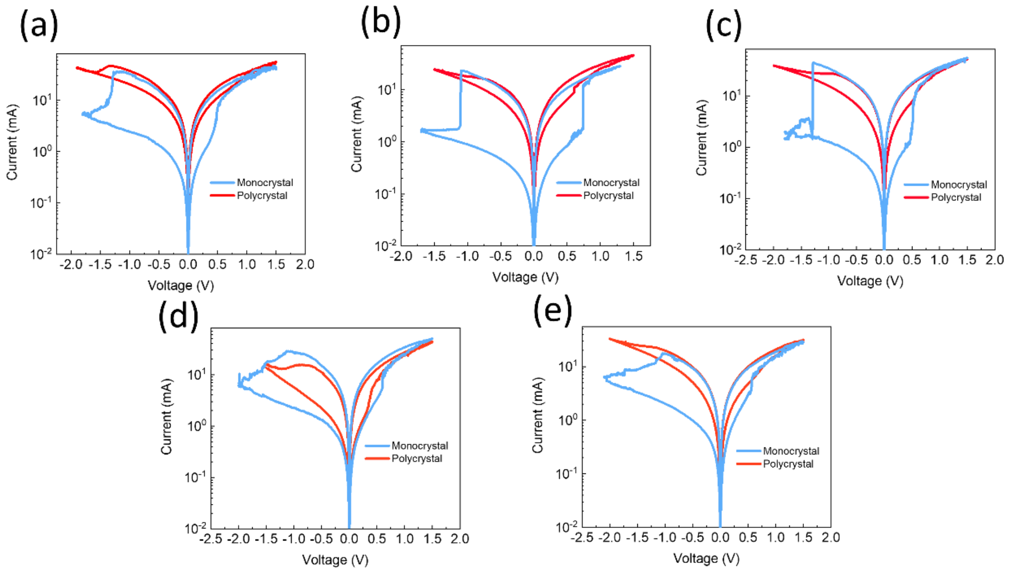

Figure 51: Cyclic voltammetry comparison of the TSC (blue line) and PC (red line) to the a) MAPbCl$_3$, (b) MAPbBr$_3$, (c) MAPbI$_3$, (d) MAPb(Br$_{0.8}$Cl$_{0.2}$)$_3$, and (e) MAPb(Br$_{0.9}$I$_{0.1}$)$_3$ perovskite compositions.

Finally, the electroforming voltage (visible in the electroformation cyclic voltammetry processes, represented in Figure 52), also displays a strong dependence on the materials' defect density. In the case of pure halide TSC, the electroforming voltage occurs at around 4.5 V, while mixed halide TSC is around 2.5 V. Regarding the PC devices, their electroforming voltage is around 1.2 V.

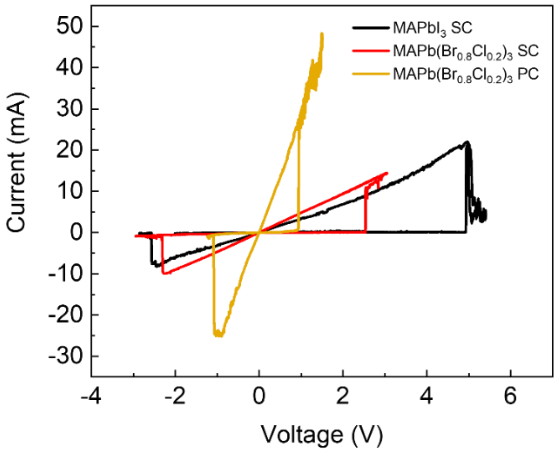

Figure 52: Electroforming process of MAPbI$_3$ TSC device (black line), MAPb(Br$_{0.8}$Cl$_{0.2}$)$_3$ TSC device (orange line), and MAPb(Br$_{0.8}$Cl$_{0.2}$)$_3$ PC device (yellow line).

The effects of defect density on various memristive device parameters can be understood in terms of its correlation with lower migration energy[317], [318]. The regulation of ionic mobility by defect density directly impacts device performance. Our results suggest that memristors with optimal properties exhibit low defect densities ($<10^{-12}$ cm^{-3}), while multistate memristors can be achieved at 10^{-13} cm^{-3}. In contrast, higher defect densities obtained with PC films, $>10^{-15}$ cm^{-3}, degrade device performance, reducing the LRS/HRS ratio by more than an order of magnitude compared to lower-defect-density counterparts.

XRD measurement that confirm the different polycrystal structures are display in figure 53.

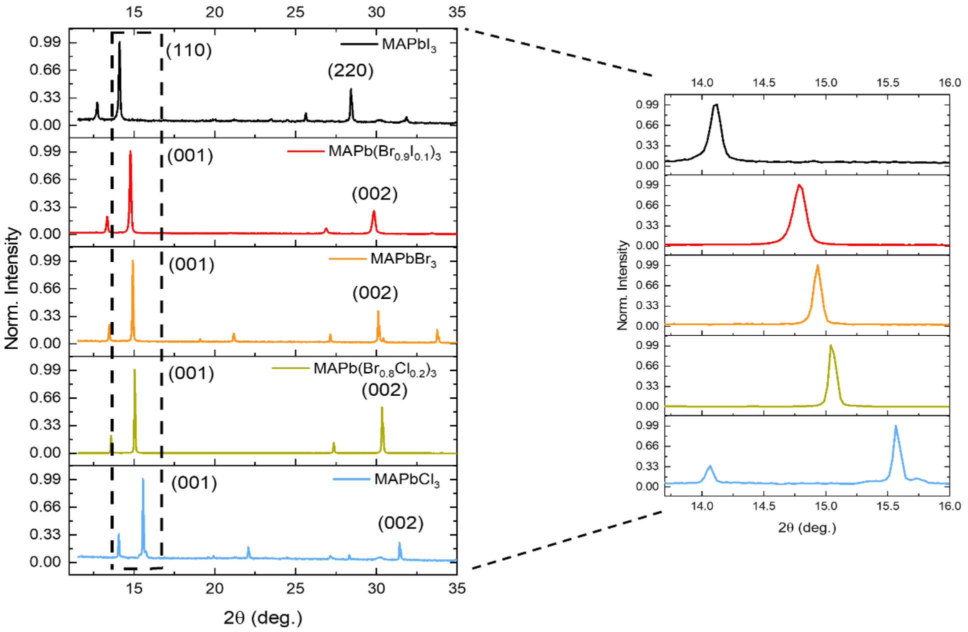

Figure 53: X-ray diffraction analysis of MAPbCl$_3$ (blue line), MAPbBr$_3$ (orange line), MAPbI$_3$ (black line), MAPb(Br$_{0.8}$Cl$_{0.2}$)$_3$ (green line), and MAPb(Br$_{0.9}$I$_{0.1}$)$_3$ (red line) of PC perovskites.

5.4 Conclusions

In summary, the performance of TSC-MHP devices varies significantly with changes in halide composition. MAPbCl$_3$ exhibited the poorest performance, with an endurance of 500 cycles, an LRS/HRS ratio of 10, and a retention time of 3000 s. In contrast, MAPbBr$_3$ demonstrated stable performance over 1000 cycles, with an LRS/HRS ratio of up to 30 and a retention time of 10^4 s. MAPbI$_3$, with its iodine-based composition, proved to be the most suitable for memristor fabrication, showing an endurance of 2500 cycles while maintaining a consistent LRS/HRS ratio over 10^4 s of retention. Furthermore, we prove that the control over defect density has been shown to influence key properties, such as the LRS/HRS ratio when compared TSC versus PC by cyclic-voltammetry. Finally, we have successfully synthesized mixed halide TSC, revealing that mixed halide perovskites enable a gradual resistive switching that can be used to operate multi-state devices. MAPb(Br$_{0.9}$I$_{0.1}$)$_3$ composition exhibits superior multistate performance, achieving six distinct conductance states during the endurance test, whereas MAPb(Br$_{0.8}$Cl$_{0.2}$)$_3$ shows lower performance, with only three conductance states observed. We conclude that multistate ReRAM memristors can be closely linked to the defect density of the MHPs, particularly when combined with the use of mixed-halide compositions, without implying that defect density is the only determining factor. These findings open the door to the development of next-generation memristors with high-density data storage capabilities and enhanced operational efficiency.

Chapter 6

Conclusions and Future Outlook

This thesis has explored the development, functional characterization, and application potential of SC-MHP and TSC for use in memristive devices, with particular emphasis on their suitability for neuromorphic computing. Through a comprehensive experimental approach, the work demonstrates that the integration of morphological and compositional engineering strategies allows for the rational tuning of the resistive switching behavior in metal halide perovskite-based memristors.

Chapter 2 of the thesis focused on the passivation of bulk $MAPbBr_3$ SCs via CW blue laser irradiation. The study revealed that this treatment induces a localized and controllable decomposition of methylammonium bromide, resulting in the formation of a $PbBr_2$-rich surface layer. This modification leads to a dramatic increase in photoluminescence intensity, up to two orders of magnitude, along with a bandgap widening of approximately 75 meV. A wide array of complementary techniques, including X-ray diffraction, X-ray photoelectron spectroscopy, micro-photoluminescence, photoluminescence excitation , and time-resolved photoluminescence , were employed to verify the structural, optical, and chemical modifications induced by the laser. In particular, is reported the formation of a bilayer structure: an upper layer composed of $PbBr_2$ and a lower layer consisting of modified $MAPbBr_3$ lattice, with both interfaces interpenetrating. This bilayer architecture results from the laser-induced partial decomposition of $CH_3NH_3^+$, generating a passivated surface that reduces non-radiative defects. The $PbBr_2$ layer functions as a protective barrier, while the extended-bandgap $MAPbBr_3$ region exhibits enhanced photoluminescence. These findings indicate that photonic-induced morphological and compositional modification contributes to the increased photoluminescence efficiency and stability of the SC, demonstrating the relevance of surface chemistry in tailoring the optoelectronic behavior of bulk SCs.

Chapter 4 introduced TSC perovskite memristors fabricated using a CITC approach. This strategy enabled the growth of micrometer-thick SCs, combining the superior crystallinity structure and defect suppression of SCs with device-compatible thicknesses. The resulting memristors exhibited excellent performance metrics: a high LRS/HRS current ratio (up to 50), stable resistive switching with endurance surpassing 10^3 cycles, and robust long-term retention under ambient conditions without encapsulation. These properties were validated through cyclic voltammetry, endurance and retention tests, and current–voltage characterizations. Furthermore, the use of impedance spectroscopy allowed, for the first time, the in situ observation of the electroforming process in a perovskite-based memristor. The IS results revealed a shift in the kinetic relaxation time (τ_{kin}) during the electroforming process, correlating with ionic redistribution phenomena and providing mechanistic insight into the resistive switching behavior of the TSC device.

In chapter 5 the effect of compositional engineering is studied on TSC-MHP memristors. It is demonstrated that the memristive performance of TSC-MHPs is strongly influenced by the halide composition. Devices based on $MAPbCl_3$ showed the least favorable characteristics, with endurance limited to 500 cycles, an LRS/HRS ratio of approximately 10, and a retention time of 3000 seconds. In contrast, $MAPbBr_3$ devices displayed improved stability, maintaining an LRS/HRS ratio of up to 30 across 1000 switching cycles and sustaining performance for up to 10^4 seconds. Among the compositions tested, $MAPbI_3$ emerged as the most promising candidate for memristor applications, withstanding 2500 switching cycles and exhibiting stable resistance states throughout 10^4 seconds of operation. Additionally, we demonstrated that the density of defects plays a crucial role in defining device performance, as revealed by cyclic voltammetry comparisons between TSC and PC architectures.

Moreover, we successfully fabricated TSC with mixed-halide compositions, showing their potential for enabling gradual resistive switching, essential for multi-state memory functionality. Specifically, the $MAPb(Br_{0.9}I_{0.1})_3$ formulation achieved six discrete resistive states in endurance measurements, outperforming the $MAPb(Br_{0.8}Cl_{0.2})_3$ variant, which only reached three distinguishable states. These results indicate that the combination of defect management and halide mixing is a viable strategy for engineering multistate resistive behavior. This study paves the way toward the development of advanced ReRAM devices with enhanced storage density and improved operational robustness.

Overall, the thesis underscores the unique potential of SC-MHPs as a versatile platform for next-generation memristive electronics. The combination of:

1. **Surface passivation strategies** for defect minimization and bandgap engineering,
2. **Morphological control and device integration** via CITC for TSC,
3. **Mechanistic insight** through impedance spectroscopy, and
4. **Compositional engineering** for multistate tuning and enhanced performance.

represents a significant advancement in the rational design of perovskite memristors. These results establish critical design principles for integrating SC-MHP into low-cost, and high-performance memory systems. Furthermore, the demonstrated tunability and reliability of these devices open promising avenues for their application in neuromorphic computing, where multilevel memory elements, stability, and low-energy operation are essential.

This work thus offers experimental validation of TSC perovskite memristors and establishes a solid foundation for future research into the design and optimization of hybrid memory devices, highlighting the potential of halide perovskites for stable, tunable, and energy-efficient neuromorphic systems.

Resumen en castellano

Capítulo 1: Introducción

Este capítulo sienta las bases conceptuales y tecnológicas de la tesis doctoral, introduciendo el marco de la computación neuromórfica como una alternativa necesaria ante los crecientes desafíos de la computación tradicional basada en la arquitectura de von Neumann. Esta arquitectura, que ha sido la base de la informática moderna durante décadas, se enfrenta actualmente a limitaciones fundamentales en cuanto a eficiencia energética, velocidad de procesamiento, escalabilidad y sostenibilidad. Estas limitaciones se han vuelto especialmente relevantes ante el crecimiento exponencial del uso de inteligencia artificial, procesamiento de grandes volúmenes de datos y dispositivos conectados a Internet.

En este contexto, la computación neuromórfica surge como una vía prometedora para lograr arquitecturas más eficientes y adaptativas, capaces de operar con bajo consumo energético y realizar tareas de procesamiento paralelo, aprendizaje y reconocimiento de patrones. Los memristores, dispositivos capaces de modificar su resistencia según el historial de voltaje aplicado, constituyen el pilar básico para implementar sinapsis electrónicas. Su capacidad de retener estados de memoria de manera no volátil los convierte en candidatos ideales para sustituir los dispositivos tradicionales en hardware neuromórfico.

En paralelo, el capítulo introduce las perovskitas de haluro metálico como materiales emergentes de gran interés para este tipo de aplicaciones. Las perovskitas destacan por su facilidad de síntesis en disoluciones a bajas temperaturas, sus propiedades optoelectrónicas ajustables, su dualidad electrónica-iónica y su bajo coste. Especial atención se dedica a los monocristales, cuya ausencia de límites de grano y baja densidad de defectos permite obtener propiedades electrónicas superiores, mayor estabilidad estructural y mejor rendimiento general frente a los policristales. Dichas propiedades se describen detalladamente y comparándolas con sus análogos policristales. Además, se incluye un apartado de métodos de síntesis de monocristales, así como de casos prácticos de aplicaciones en distintos dispositivos.

Propiedades optoelectrónicas de los monocristales:

1. Propiedades ópticas

La energía de banda prohibida (*bandgap*) de las perovskitas controla su absorción óptica, y puede ser sintonizada mediante sustitución de haluros y cationes. Por ejemplo, los cristales de $MAPbX_3$ presentan bandas prohibidas que varían desde 1.53 eV (X = I) hasta 2.97 eV (X = Cl), permitiendo así una cobertura espectral ajustable. La mezcla de haluros facilita una sintonización continua del *bandgap*, lo que es crucial para aplicaciones específicas. Además, los monocristales tienden a mostrar bordes de absorción más extendidos y desplazamientos al rojo respecto a las películas, debido a su menor densidad de defectos y mayor espesor.

2. Transporte de carga

Los monocristales poseen movilidades de portadores de carga mucho mayores que las películas policristalinas, alcanzando valores superiores a 500 $cm^2V^{-1}s^{-1}$ en $CsPbBr_3$. Esto, combinado con tiempos de vida largos (cientos de microsegundos), da lugar a longitudes de difusión superiores a 175 μm. Estas propiedades se evalúan mediante técnicas como TRPL, SCLC, Hall, ToF o SPV. En monocristales también se observa transporte anisotrópico, dependiendo de la orientación cristalina (por ejemplo, las caras (110) pueden tener menos defectos que las (100)).

3. Migración iónica

Aunque los monocristales no tienen límites de grano, no están exentos de migración iónica. Vacantes e intersticiales de haluros y cationes orgánicos son móviles bajo estímulos eléctricos o lumínicos. Esta migración, facilitada por la iluminación, puede inducir histéresis e inestabilidad. Para su supresión se han propuesto estrategias como la modificación composicional, reducción dimensional y pasivación.

4. Defectos de red cristalina

La densidad de defectos en monocristales es mucho menor (10^8–10^{11} cm^{-3}) que en películas (10^{14}–10^{18} cm^{-3}). Sin embargo, las superficies de los monocristales son más vulnerables, siendo foco de vacantes de haluro o defectos por humedad. La densidad de trampas puede cuantificarse mediante la técnica SCLC, que revela el voltaje de transición desde régimen óhmico a límite de llenado de trampas (V_{TFL}).

5. Estabilidad

Los monocristales son más estables frente al aire, humedad y temperatura que sus contrapartes policristalinas. Algunos han mostrado estabilidad durante más de 14 meses sin encapsulación. No obstante, la exposición prolongada a la luz puede generar trampas superficiales, que degradan el rendimiento con el tiempo.

Métodos de síntesis de monocristales

Para aprovechar plenamente sus propiedades, es fundamental sintetizar monocristales de alta calidad. A diferencia del *spin-coating* utilizado en películas, el crecimiento de monocristales requiere un control riguroso de temperatura, composición y sobresaturación. Los métodos de síntesis más comunes son:

1. Cristalización por enfriamiento (TCC)

Requiere enfriar lentamente una solución saturada, lo que permite crecimiento controlado pero lento (varios días o semanas). Se emplea principalmente con soluciones ácidas.

2. Cristalización asistida por vapor de anti-disolvente (AVC)

Usa difusión de un anti-disolvente en fase vapor (como tolueno) en una solución con alta solubilidad. Es efectiva a baja temperatura, pero necesita control preciso de la velocidad de difusión.

3. Cristalización por temperatura inversa (ITC)

Aprovecha la solubilidad inversa de ciertos haluros en disolventes como GBL o DMF. Al aumentar la temperatura, disminuye la solubilidad, generando sobresaturación y crecimiento rápido (horas). Ideal para monocristales del orden de los centímetros.

4. Cristalización confinada por temperatura inversa (CITC)

Modificación del ITC que restringe el crecimiento en el eje vertical, permitiendo obtener monocristales delgados (de pocos μm). Es útil para integrar monocristales en estructuras planas como celdas solares o memristores.

En esta tesis, se han elegido los métodos ITC y CITC por su rapidez y alta cristalinidad de dispositivos obtenidos y integración de dispositivos, descartando otros como AVC por sus largos tiempos de síntesis o ausencia de control de espesor.

Dispositivos basados en perovskitas monocristalinas

1. Celdas solares

Los monocristales permiten eliminar límites de grano, lo que mejora el transporte de cargas y reduce la recombinación. Además, muestran menor migración iónica, aumentando la estabilidad operativa. Ya se han alcanzado eficiencias del 24% en dispositivos monocristalinos de células solares.

2. Fotodetectores

Los monocristales permiten detenciones superiores a 10^{12} Jones y tiempos de respuesta inferiores a 1 µs. Su bajo nivel de corriente oscura y alta calidad óptica los hacen ideales para sensores de imagen, comunicaciones ópticas, etc.

3. LEDs y láseres

Gracias a su ganancia óptica, bajos defectos y alto rendimiento cuántico de luminiscencia, los SCs son excelentes para tecnologías de emisión. En LEDs se han conseguido EQEs >10% y estabilidad operativa de más de 30 h. En láseres, monocristales como $MAPbBr_3$ permiten emisión continua con umbrales bajos y líneas de emisión estrechas (<0.2 nm).

4. Memristores

Los monocristales ofrecen alta movilidad, baja densidad de defectos y mayor robustez estructural. Estas propiedades se traducen en ratios de baja y alta resistencia (LRS/HRS) altos, mayor resistencia y bajo consumo energético. Aunque aún están en fases tempranas, los memristores basados en monocristales muestran un gran potencial para memorias de alta densidad y computación neuromórfica. Esta tesis busca profundizar en estos dispositivos, abordando parámetros clave como retención, mecanismos de conmutación y estabilidad.

El capítulo finaliza estableciendo los objetivos principales de la tesis. El primero es mejorar las propiedades ópticas y electrónicas de monocristales *bulk* mediante tratamientos superficiales basados en láser. El segundo es desarrollar y optimizar dispositivos memristivos fabricados a partir de monocristales delgados que permita obtener un mayor rendimiento memrsitivo con respecto a los memristores fabricados usando perovskitas policristalinas.

Capítulo 2: Métodos

Este capítulo detalla los métodos experimentales utilizados a lo largo de la tesis para la síntesis de materiales, la fabricación de dispositivos y su posterior caracterización estructural, óptica y eléctrica. El enfoque metodológico está centrado en lograr reproducibilidad, control sobre las propiedades estructurales de los monocristales y obtener datos comparables entre diferentes composiciones y morfologías de perovskitas.

En cuanto a la síntesis de monocristales, se emplea el método de cristalización por temperatura inversa, basado en la solubilidad inversa de las perovskitas en disolventes orgánicos. Este método permite obtener cristales con baja densidad de defectos y buena calidad óptica. Para la fabricación de monocristales delgados, se aplica una variante confinada del ITC, en la que la solución precursora se encapsula entre dos sustratos recubiertos de PTAA. El control preciso de la temperatura y del volumen de solución permite obtener cristales con grosores entre 20 y 30 µm y áreas del orden de mm^2. Este procedimiento se realiza completamente fuera de la *glovebox*, subrayando la viabilidad de la técnica en condiciones estándar de laboratorio.

La fabricación de dispositivos se completa mediante la aplicación de electrodos de grafito en la superficie superior del monocristal y sobre el óxido de estaño e indio (ITO) inferior, utilizando un spray comercial. Este tipo de contacto, además de ser económico y fácil de aplicar, proporciona buena estabilidad y es compatible con sustratos flexibles, lo que lo hace ideal para futuros dispositivos portátiles o implantables.

Para el estudio estructural, se utilizan técnicas como la difracción de rayos X (XRD) en geometría de incidencia rasante para analizar tanto la fase cristalina como la orientación preferente de los cristales. La microscopía electrónica de barrido (SEM) permite obtener imágenes en vista superior y sección transversal de los dispositivos, proporcionando información sobre la uniformidad de la película, la integridad del contacto y el grosor efectivo de las capas.

En la caracterización óptica se utilizan espectroscopía de fotoluminiscencia (PL), fotoluminiscencia resuelta en el tiempo (TRPL) y mapeo por micro-PL a bajas temperaturas. Estas técnicas permiten identificar la homogeneidad de emisión, la presencia de defectos superficiales y el tiempo de vida de los portadores excitados, parámetros clave para evaluar la calidad del material y su idoneidad para aplicaciones optoelectrónicas o memristivas.

Finalmente, se describe la caracterización eléctrica mediante curvas corriente-voltaje (I-V) y espectroscopía de impedancia. Esta última se emplea para evaluar fenómenos relacionados con migración iónica, capacitancia negativa e inductancia química, que son críticos para entender los mecanismos de conmutación resistiva y electroformación en dispositivos memristivos.

El capítulo concluye posicionando este conjunto de técnicas como una "caja de herramientas" que permite correlacionar estructura, composición, morfología y rendimiento eléctrico en dispositivos basados en perovskitas.

Capítulo 3: Mejora de las propiedades optoelectrónicas de monocristales *bulk* mediante tratamientos superficiales

Este capítulo aborda el primer objetivo experimental de la tesis: la mejora de las propiedades optoelectrónicas de monocristales *bulk* de $MAPbBr_3$ mediante tratamientos de pasivación láser. La motivación principal parte del hecho de que, aunque los monocristales presentan propiedades intrínsecamente superiores a las películas policristalinas, su superficie sigue estando afectada por defectos y recombinaciones no radiativas que limitan su rendimiento optoelectrónico.

Para afrontar esta limitación, se propone un tratamiento con láser continuo azul que induce una modificación superficial del monocristal, generando una capa delgada de $PbBr_2$ cristalino en su superficie. El proceso consiste en una irradiación láser en tres etapas: estabilización, tratamiento y postratamiento. Se observa una notable mejora de la intensidad de la PL, que aumenta en dos órdenes de magnitud tras el tratamiento, junto con un ensanchamiento del gap óptico de $\approx$75 meV.

El estudio espectroscópico revela que el incremento de PL no es atribuible a un simple efecto térmico, como se demuestra mediante experimentos de recocido térmico que no reproducen el mismo resultado. Mediante PL y PLE (espectroscopía de excitación de fotoluminiscencia), se verifica una emisión desplazada hacia el azul, lo que confirma la modificación estructural superficial del monocristal. La microscopía óptica y la micro-PL a 4 K permiten observar una doble capa: una superior compuesta por $PbBr_2$ y una inferior constituida por $MAPbBr_3$ modificado, donde ambas interfases se interpenetran. Esta estructura bicapa resulta de la descomposición parcial del $CH_3NH_3^+$ inducida por láser, generando una superficie pasivada que reduce defectos no radiativos. La capa de $PbBr_2$ actúa como barrera protectora, mientras que la región de $MAPbBr_3$ con banda prohibida extendida muestra una fotoluminiscencia intensificada y estable. Estos resultados indican que la modificación morfológica y composicional inducida fotónicamente contribuye al aumento de eficiencia fotoluminiscente y estabilidad del monocristal.

Además, e lleva a cabo una caracterización química de la superficie mediante espectroscopía de fotoelectrones (XPS) con radiación sincrotrón. Se identifican nuevos picos correspondientes a $PbBr_2$ y a la ausencia de señales del grupo metilamonio, lo cual sugiere una descomposición parcial de la perovskita original. El análisis de la energía de unión permite explicar por qué se observa Pb pero no N en la superficie: la baja energía cinética de los electrones del nitrógeno impide que escapen desde capas más profundas, mientras que los electrones del plomo, con mayor energía cinética, logran ser detectados incluso si se encuentran a mayor profundidad. Esto refuerza el modelo de una estructura bicapa donde una capa rica en $PbBr_2$ recubre una zona de $MAPbBr_3$ estructuralmente distorsionada pero aún activa ópticamente, con el grupo metilamonio parcialmente descompuesto. La combinación de estos hallazgos apoya la hipótesis de que la interacción con el láser en presencia de oxígeno induce una transformación química superficial que mejora la estabilidad y las propiedades optoelectrónicas del monocristal.

Además, se propone un mecanismo químico para esta transformación, en el que $CH_3NH_3^+$ se descompone bajo la acción combinada de luz y oxígeno, formando compuestos como CH_3NH_2 y HCOOH. Estos compuestos, lejos de ser únicamente productos residuales, pueden contribuir a la estabilización de la superficie del monocristal, disminuyendo la concentración de agua y evitando la formación de defectos no radiativos.

Este capítulo demuestra que es posible modificar de forma localizada y controlada la superficie de monocristales de perovskita mediante irradiación láser, mejorando su emisión opticaelecrtronic y su estabilidad. Estos hallazgos abren la puerta a nuevas estrategias de ingeniería superficial para dispositivos optoelectrónicos de alto rendimiento.

Capítulo 4: Desarrollo y caracterización de memristores basados en monocristales delgados

Este capítulo aborda el segundo gran objetivo de la tesis: la implementación y estudio funcional de memristores fabricados a partir de monocristales delgados de $MAPbBr_3$. A diferencia de los monocristales *bulk* tratados en el capítulo anterior, que abarcan un espesor del orden de los milímetros, aquí se sintetizan cristales de entre 20 y 30 μm de espesor mediante una variante confinada del método ITC. Esta configuración permite preservar las ventajas estructurales del monocristal, al tiempo que se mejora la aplicabilidad en dispositivos funcionales por su delgado espesor, que facilita la integración en arquitecturas planas y reduce las barreras de transporte de carga. Esta aproximación permite combinar la baja densidad de defectos y la alta movilidad de portadores típica de los monocristales, con una mejor compatibilidad para la fabricación de dispositivos electrónicos compactos y reproducibles.

Además, el uso de monocristales delgados permite una caracterización más precisa del mecanismo de electroformación, ya que, debido a la robustez, el sistema permite registrar con mayor fidelidad las respuestas eléctricas asociadas al proceso de electroformación mediante espectroscopía de impedancia. El capítulo presenta tanto la síntesis controlada como la implementación de dispositivos memristivos con electrodos de grafito y contactos ITO, sin encapsulado y bajo condiciones ambientales, lo que subraya su viabilidad para aplicaciones reales. Se incluyen estudios de voltametría cíclica, test de resistencia LRS/HRS, retención temporal, análisis de respuesta rápida y, de manera inédita, espectroscopía de impedancia para registrar in situ el proceso de electroformación del dispositivo, proporcionando una visión profunda del rol de la migración iónica en monocristales de perovskita.

Se describe en detalle la arquitectura del dispositivo: una estructura de tipo *sandwich* con ITO/PTAA como electrodo inferior y grafito como electrodo superior. Esta configuración no solo reduce los costes de fabricación, sino que también mejora la compatibilidad con futuras aplicaciones flexibles. La fabricación se realiza íntegramente fuera de *glovebox*, demostrando la viabilidad en condiciones ambientales.

El rendimiento eléctrico de los dispositivos se evalúa mediante curvas de voltamperometría cíclica. Se observa un comportamiento de conmutación resistiva claro, con transición entre estados de alta y baja resistencia al aplicar voltajes específicos. El voltaje de SET se estabiliza en torno a 0.6 V, mientras que el RESET ocurre aproximadamente a −2.3 V. Se reporta una relación LRS/HRS de hasta 50, acompañada de una estabilidad por encima de 10^3 ciclos de escritura/borrado bajo condiciones ambientales, sin encapsulado. Esta resistencia al estrés cíclico evidencia la robustez del monocristal delgado como medio activo en memristores, superando significativamente a dispositivos basados en películas policristalinas equivalentes.

Asimismo, se realiza una prueba de retención temporal, en el que se demuestra que el dispositivo mantiene su estado resistivo durante más de 10^4 segundos sin decrecimiento significativo de corriente, lo que confirma su naturaleza no volátil.

Una de las contribuciones clave de este capítulo es el uso de espectroscopía de impedancia para estudiar en detalle el proceso de electroformación. A través de medidas a distintos V_{dc}, se identifican cambios en el espectro de impedancia compatibles con la formación de rutas conductivas inducidas por migración y acumulación iónica. Aparece una componente inductiva negativa atribuida a la acumulación superficial de iones, modelada mediante un circuito equivalente que incluye una inductancia química.

El análisis detallado de los tiempos de relajación cinética (τ_{kin}) derivados del ajuste del modelo revela una evolución desde procesos lentos (acumulación iónica) hacia procesos más rápidos (difusión de vacancantes), a medida que el dispositivo pasa de un estado prístino a un estado activado. Este seguimiento del electroformado in situ mediante IS representa una novedad significativa en el estudio de memristores de perovskita.

Además, se comparan dispositivos monocristalinos y policristalinos con la misma arquitectura, evidenciando un rendimiento claramente superior en los primeros: mayor estabilidad, mejor ratio LRS/HRS. Esta comparación refuerza la hipótesis de que la morfología monocristalina es clave para optimizar el funcionamiento de memristores basados en perovskitas.

En conjunto, este capítulo no solo demuestra la viabilidad técnica de fabricar dispositivos memristivos con monocristales delgados, sino que también establece un marco experimental completo para su caracterización eléctrica, con énfasis en la identificación del mecanismo de conmutación resistiva y su relación con la migración iónica. Los resultados obtenidos sientan las bases para futuras aplicaciones en computación neuromórfica, donde la estabilidad y un alto ratio LRS/HRS son parámetros críticos. La posibilidad de registrar el proceso de electroformación mediante IS en condiciones reales de funcionamiento, permiten una comprensión más profunda del comportamiento dinámico de estos dispositivos. Además, se abre la puerta al diseño racional de nuevas arquitecturas basadas en perovskitas monocristalinas con propiedades ajustadas mediante ingeniería morfológica, elemento clave para el desarrollo de hardware neuromórfico eficiente y de bajo costo.

Capítulo 5: Ingeniería composicional de memristores de perovskita monocristalina: hacia dispositivos multistate estables

Este capítulo se plantea como una continuación directa del capítulo anterior, donde se exploraba la viabilidad funcional de los memristores fabricados a partir de monocristales delgados de $MAPbBr_3$. En esta nueva sección se amplía el estudio hacia el empleo de estrategias de ingeniería composicional, introduciendo mezclas de haluros (Br/Cl y Br/I) como herramienta para modificar de forma sistemática las propiedades electrónicas e iónicas del material activo y, con ello, obtener dispositivos multistate estables.

El objetivo central es doble: por un lado, comparar de manera controlada dispositivos basados en monocristales de haluros puros, $MAPbX_3$ (X = Cl, Br, I) bajo una arquitectura homogénea; y por otro, introducir perovskitas de haluro mixto, $MAPb(Br_{0.8}Cl_{0.2})_3$ y $MAPb(Br_{0.9}I_{0.1})_3$, para estudiar el efecto de la composición sobre la densidad de defectos y su impacto en las propiedades memristivas.

5.1 Caracterización estructural y óptica

Se emplea el método de cristalización por CITC para crecer monocristales delgados (20–25 µm) de $MAPbX_3$ y sus versiones mixtas. Mediante difracción de rayos X, se confirma la alta cristalinidad de todas las composiciones y, especialmente, la coherencia estructural de las mezclas halogenadas, que presentan desplazamientos en los picos del plano (100) según lo predicho por la ley de Vegard.

Los espectros de PL muestran emisiones características para cada haluro, sin evidencia de segregación de fases en los compuestos mixtos, lo que valida la estabilidad composicional de los cristales sintetizados.

5.2 Dispositivos memristivos basados en monocristales puros

Los monocristales de $MAPbCl_3$, $MAPbBr_3$ y $MAPbI_3$ se integran en una arquitectura sencilla con capa de PTAA como interfase y electrodo superior de grafito. La conmutación resistiva se evalúa mediante curvas de voltamperometría cíclica, mostrando transiciones abruptas entre los estados HRS y LRS, sin correlación directa con el *bandgap*.

Los ensayos de resistencia de ciclado (escritura y borrado) revelan un comportamiento altamente dependiente del haluro: el dispositivo $MAPbCl_3$ falla tras 500 ciclos mostrando una elevada dispersión en el LRS, $MAPbBr_3$ se mantiene estable durante más de 1000 ciclos, y $MAPbI_3$ supera los 2800 ciclos, siendo uno de los valores más altos reportados.

3. Dispositivos memristivos con perovskitas mixtas: *multistate* y defectos

La introducción de haluros mixtos produce un cambio fundamental en el mecanismo de conmutación. Los dispositivos basados en $MAPb(Br_{0.8}Cl_{0.2})_3$ y $MAPb(Br_0.9I_{0.1})_3$ presentan transiciones graduales desde el estado LRS al HRS, en lugar de abruptas, permitiendo así operar en modo *multistate*. Al variar cuidadosamente el voltaje de reset, se pueden obtener múltiples niveles de resistencia estables.

En el caso de $MAPb(Br_0.9I_{0.1})_3$, se logran seis estados bien diferenciados con retención de 500 segundos por estado y una estabilidad total de 150 ciclos. Por otro lado, $MAPb(Br_{0.8}Cl_{0.2})_3$ alcanza hasta nueve estados en retención, pero solo tres logran estabilidad suficiente en ensayos de estabilidad, con hasta 200 ciclos por estado.

Estos resultados indican que la mezcla de haluros no solo altera la transición resistiva, sino que también introduce una mayor densidad de defectos que afecta el mecanismo iónico subyacente, permitiendo la aparición del comportamiento *multistate*.

5.4 Estudio del mecanismo de conmutación y densidad de defectos

Se emplea el método de corriente limitada por carga espacial (SCLC) para cuantificar la densidad de defectos en todos los dispositivos. Los monocristales puros presentan densidades en torno a 10^{11} cm^{-3}, mientras que los mixtos alcanzan valores del orden de 10^{13} cm^{-3}. En comparación, los dispositivos policristalinos muestran densidades de 10^{16} cm^{-3} o más.

La densidad de defectos se correlaciona fuertemente con el comportamiento de la conmutación: defectos elevados facilitan la migración iónica y generan transiciones graduales (*multistate*), mientras que defectos reducidos favorecen transiciones abruptas y alta relación LRS/HRS.

Además, se observa que la tensión de electroformación disminuye a medida que aumenta la densidad de defectos: 4.5 V para monocristales puros, 2.5 V para los mixtos, y tan solo 1.2 V para los policristales. Esto refuerza la idea de que los defectos actúan como facilitadores de la migración iónica y, por tanto, del mecanismo de conmutación resistiva.

5. Conclusión del capítulo

Este capítulo confirma que la ingeniería composicional en perovskitas monocristalinas permite ajustar la densidad de defectos y, con ello, controlar las propiedades fundamentales de los memristores. En particular, se demuestra que que los dispositivos de $MAPbI_3$ ofrecen el mejor rendimiento entre las composiciones puras, con excelente estabilidad, alta relación HRS/LRS y larga retención. Además se observa que la introducción de haluros mixtos posibilita conmutación *multistate*, una propiedad clave para el desarrollo de memristores neuromórficos y almacenamiento de datos en alta densidad. Finalmente, se establece que existe una relación directa entre la composición, la densidad de defectos y el tipo de conmutación resistiva, lo que permite utilizar esta propiedad como parámetro de diseño funcional.

En conjunto, esta sección refuerza la hipótesis de que mediante una combinación estratégica de control morfológico (monocristal frente a policristal) y composicional (haluros simples o mixtos), es posible diseñar dispositivos memristivos con propiedades a medida. La demostración de operación *multistate* en monocristales delgados marca un avance importante hacia la implementación práctica de perovskitas como plataforma central en tecnologías de computación neuromórfica de alta densidad de procesado.

Capítulo 6: Conclusiones y perspectivas

El capítulo final de la tesis presenta un análisis integrador de los resultados obtenidos y destaca las contribuciones más relevantes del trabajo, estructurado en torno a dos ejes fundamentales: la mejora de las propiedades ópticas de monocristales *bulk* de perovskita y el desarrollo de memristores basados en monocristales delgados.

En primer lugar, se ha demostrado que es posible modificar la superficie de monocristales *bulk* de $MAPbBr_3$ mediante irradiación con láser azul continuo, lo que da lugar a la formación controlada de una capa superficial de $PbBr_2$. Esta modificación genera un aumento notable en la intensidad de fotoluminiscencia (≈100 veces) y una ampliación del *bandgap* de ≈75 meV. A través de una batería de técnicas estructurales (XRD), químicas (XPS) y ópticas (PL, TRPL, PLE), se ha verificado el mecanismo de formación inducido por el láser, asociado a la descomposición parcial del catión metilamonio en presencia de oxígeno. Esta descomposición genera una nueva capa de estructura cristalina distorsionada y subproductos como ácido fórmico y metilamina, los cuales juegan un papel clave en la pasivación de defectos superficiales, estabilizando la nueva capa extendida de perovskita.

En segundo lugar, se ha desarrollado por primera vez un memristor funcional basado en monocristales delgados de perovskita. Mediante un método de cristalización confinada a baja temperatura (60 °C), se han producido dispositivos con espesores entre 20 y 30 µm que presentan relaciones LRS/HRS de hasta 50, tiempos de retención superiores a 10^4 s, y más de 1000 ciclos de escritura/borrado sin pérdida de rendimiento. Todo ello, sin encapsulación y fabricado completamente fuera de *glovebox*.

Una de las aportaciones más relevantes ha sido el uso pionero de la espectroscopía de impedancia como técnica para registrar in situ el proceso de electroformación, revelando la evolución dinámica de los mecanismos resistivos y la participación de procesos iónicos. La identificación de tiempos de relajación cinética decrecientes ha permitido correlacionar directamente los estados de conmutación con dinámicas de acumulación y difusión de iones, lo cual representa un acercamiento nobel al estudio del electroformado para esclarecer el mecanismo de dicho proceso.

Finalmente, se ha demostrado que la incorporación de ingeniería composicional en monocristales de perovskita permite controlar de manera precisa el comportamiento resistivo de dispositivos memristivos. Mediante la fabricación de monocristales mixtos con diferentes proporciones de haluros, se ha conseguido modular no solo el *set/reset voltage* y la relación LRS/HRS, sino también inducir comportamientos *multistate* estables y reproducibles. Este resultado es especialmente relevante en el contexto de computación neuromórfica, donde la existencia de múltiples estados de resistencia con memoria no volátil permite emular con mayor fidelidad sinapsis biológicas.

Estos trabajos no solo refuerzan el papel de las perovskitas como materiales funcionales emergentes más allá de la optoelectrónica tradicional, sino que proporciona un conjunto de herramientas experimentales y conceptos fundamentales para su integración en dispositivos de memoria neuromórfica. Se ha demostrado que es posible combinar estrategias de ingeniería composicional y control morfológico para habilitar el comportamiento *multistate* y la estabilidad operativa, aspectos claves en el camino hacia dispositivos neuromórficos de alto rendimiento.

Como líneas futuras de investigación, se sugiere la optimización de los dispositivos mediante el estudio del impacto que tienen el uso de distintas interfases de naturaleza variada (óxido, polímeros, capas selectoras de huecos y electrones) que acompañan al material activo en el dispositivo, así como la integración de estos dispositivos en arquitecturas de red neuromórfica. Además, podría ser de gran interés explorar estrategias de sinapsis plástica y modulación conductiva a múltiples niveles que imiten de forma más realista las funciones cognitivas del cerebro humano.

En suma, esta tesis ha sentado una base sólida para el desarrollo integral de monocristales de perovskita como plataformas versátiles para nuevas generaciones de dispositivos memristivos, destacando su potencial para dar forma al futuro de la computación eficiente, adaptable y sostenible.

Appendix A: Index of figures, tables and equations

Index of figures

Figure 12. Schematic diagram of perovskite SCs growth via AVC method[111].

Figure 13**.** (a) Schematic illustration of the (ITC setup, where the vial containing the precursor solution is immersed in a temperature-controlled heating bath. The solution is gradually heated from room temperature to elevated setpoints, approximately 80 °C for $MAPbBr_3$ and 110 °C for $MAPbI_3$, to induce crystallization. (b, c) Time-resolved growth of $MAPbI_3$ and $MAPbBr_3$ single crystals, showing progressive enlargement and facet development at various intervals[112].

Figure 14. Scheme of the CITC method to fabricate thin perovskite single crystals.

Figure 15. (a) Filament[143], and (b) interfacial[138] mechanism resistive switching scheme in perovskite-based memristors.

Figure 16. (a) Inverse temperature crystallization process[112], and (b) confined inverse crystallization scheme.

Figure 17. Optical images of (a) a pristine and (c) a laser over-treated $MAPbBr_3$ single crystal. (b) Schematic diagram of the experimental setup: S, sample; PL, photoluminescence; F1 and F2, optical filters used to adjust the excitation power and block scattered excitation light, respectively; OF, optical fiber; SP, spectrograph; PC, computer.

Figure 18. (a) Temporal evolution of the normalized photoluminescence (PL) intensity of $MAPbBr_3$ single crystals monitored in situ at 540 nm under continuous illumination with a 445 nm CW laser: stage I (red line) corresponds to an excitation fluence of 0.15 W/cm^2, stage II (green line) to 1.5 W/cm^2, and stage III (blue line) to 0.15 W/cm^2; (b) normalized PL spectra acquired in situ at different time points during stage II of the laser treatment; (c) normalized PL spectra recorded with varying delays from the start of stage II; (d) spectral deconvolution of the PL signal measured 110 s after the initiation of stage II, revealing two Gaussian components centered at 526 nm and 546 nm.

Figure 19. (a) Time evolution of the normalized photoluminescence (PL) intensity of a $MAPbBr_3$ single crystal measured in situ at 540 nm under 445 nm CW laser illumination: Stage I (red symbols) excitation fluence of 0.15 W/cm^2; Stage II (green symbols) excitation fluence of 0.75 W/cm^2; Stage III (blue symbols), excitation fluence of 0.15 W/cm^2. (b) In situ PL spectra recorded at different time intervals following the onset of Stage II laser treatment.

Figure 20. Deconvolution of the PL spectra acquired within the first 0–110 s of high-intensity laser irradiation, fitted as the sum of two Gaussian components.

Figure 21. Photoluminescence (PL) spectra of a $MAPbBr_3$ single crystal recorded before (red line) and after (blue line) thermal annealing at 120 °C for 20 minutes.

Figure 22. (a) PL and PLE spectra for $MAPbBr_3$ single crystals before (red) and after (blue) laser treatment. (b) PL decay kinetic for treated (blue) and untreated (red) $MAPbBr_3$ single crystals, normalized to the long-lived component. The inset displays the same decay profiles on a linear scale, normalized to their respective peak intensities.

Figure 23. Evaluation of the S_{tr}/S_{ntr} ratio, defined as the ratio of the integrated areas under the surface-related components of the PL decay curves for laser-treated (rose) and untreated (blue) $MAPbBr_3$ single crystal.

Figure 24. (a) XRD patterns of $MAPbBr_3$ single crystals before and after laser exposure, shown alongside theorical patterns for $PbBr_2$ and $MAPbBr_3$. (b, c) Cross-sectional analysis of a laser-treated $MAPbBr_3$ single crystal: (b) optical microscopy image and (c) µPL intensity map at 551 nm. (d) µPL spectra recorded at six specific locations labeled 1–6 in panel (b). The inset presents a magnified view of the excitonic region between 550 and 552 nm. Both (c) and (d) were acquired at a temperature of 4 K.

Figure 25. PL spectra of pristine (solid lines) and laser-treated (dashed lines) $MAPbBr_3$ single crystals measured at 300 K (red) and 30 K (blue).

Figure 26. 3D maps illustrating the combined topography and contact potential difference (CPD) for (a) a pristine $MAPbBr_3$ single crystal (topography scale: 0–14 nm) and (b) a laser-treated crystal (topography scale: 0–380 nm). The CPD is defined as the difference between the work function of the tip and that of the sample, given by: ($eCPD_{sample}=\phi_{tip}—\phi_{sample}$). Since determining the tip's work function precisely is challenging, measurements are calibrated using a gold reference: ($eCPD_{ref} = \phi_{tip} — \phi_{ref}$). This allows calculation of the sample's work function as: $\phi_{sample}=\phi_{ref}+e(CPD_{ref}—CPD_{sample})$. Using this approach, the work function values obtained were: Passivated: CPD_{pass} = 470 mV ; Φ_{ref} = 5.27 eV ; CPD_{ref} = 220 mV and Pristine: $CPD_{pristine}$= 790 mV ; Φ_{ref} = 5.27 eV ; CPD_{ref} = 270 mV.

Figure 27. SEM top-view image of the $MAPbBr_3$ single crystal surface after laser treatment.

Figure 28. PL spectra of $MAPbBr_3$ single crystals recorded before laser treatment (A, excitation fluence: 0.15 W/cm^2), after laser treatment (B, 1.5 W/cm^2 for 10 min), and following post-treatment (C, 0.15 W/cm^2 for 10 min), measured under different atmospheric conditions: (a) dry N_2, (b) N_2 with H_2O vapor, and (c) ambient air.

Figure 29. High-resolution XPS spectra obtained in grazing emission geometry for $MAPbBr_3$ single crystals before and after laser treatment, showing core-level signals of (a) Pb 4f, (b) Br 3d, (c) N 1s, and (d) C 1s. Measurements were performed using synchrotron radiation with an incident photon energy of 515 eV. The experimental configuration involved normal photon incidence and photoelectron detection at a grazing emission angle of $\theta = 5°$, ensuring enhanced surface sensitivity.

Figure 30: Schematic representation of the confined ITC method used for growing TSCs. Notably, this approach enables the formation of highly crystalline and reproducible $MAPbBr_3$ single crystals at relatively low temperatures. In contrast to conventional methods reported in the literature that operate at temperatures up to 80 °C, the optimized growth here is achieved at 60 °C.

Figure 31: (a) Optical microscopy image of a $MAPbBr_3$ TSC grown via the confined ITC method, exhibiting sharp edges and a well-defined square geometry, indicative of high crystallinity. (b) Real photograph of a representative TSC synthesized by confined ITC method.

Figure 32: Photoluminescence spectra comparison between a bulk $MAPbBr_3$ single crystal of 2 mm thickness (black curve) and the PL emission of thin single crystals (TSCs). The blue-shift in the emission peak for the TSCs is attributed to the reduced crystal thickness.

Figure 33. (a) Schematic representation of the complete memristor device structure employing graphite electrodes for electrical characterization. The inset displays a real image of a $MAPbBr_3$ TSC grown on a PTAA layer using the confined ITC method. (b) X-ray diffraction pattern showing diffraction peaks at 15° and 30°, corresponding to the (100) and (200) planes of the cubic $MAPbBr_3$ phase, respectively. (c) Cross-sectional SEM image of a representative device. (d) Photoluminescence (PL) mapping of the TSC surface, demonstrating high spatial homogeneity in optical response.

Figure 34: Cyclic voltammetry (CV) curves illustrating the progressive reduction in the voltage required to switch the memristor device ON (solid black lines) and OFF (dashed black line); from red to blue.

Figure 35. (a) Cyclic voltammetry curves, in log scale, showing the SET and RESET over 100 cycles, recorded at a scan rate of 100 mV/s. (b) Endurance performance test under repeated voltage sweeps (+0.1 V → +1 V → +0.1 V → −2.5 V → +0.1 V). (c) Current stability monitored at a read voltage of 0.1 V for the LRS (blue line) and HRS (orange line). (d) Resistance evolution during the switching transitions between HRS and LRS.

Figure 36: Comparison of cyclic voltammetry (CV) curves for the monocrystalline (orange curve) and polycrystalline (blue curve) $MAPbBr_3$ memristor devices.

Figure 37: (a) Endurance test over 10^3 switching cycles for a representative $MAPbBr_3$ TSC memristor device. (b) Zoomed view of cycle 877. (c) Time-resolved measurement of cycle 877, showing the transition from the low-resistance state (LRS) at the read voltage to the ON state under a fixed voltage of 1 V. The red, blue, and red-shaded regions indicate the OFF, ON, and read voltage intervals, respectively.

Figure 38. (a) Impedance spectra illustrating the evolution of the device response under increasing applied bias, leading to the electroforming process. For clarity, only the fitting at 0.3 V is shown. (b) Corresponding DC current values recorded during the electroforming process (orange dots) and after reaching the low-resistance state (LRS, blue dots). (c) Quantification of the R_L and L components obtained from equivalent circuit fitting (circuit shown in the inset of panel d) using the surface polarization model (SPM)[75]. (d) Kinetic relaxation times (τ_{kin}) extracted from the negative capacitance features observed during the electroforming process.

Figure 39: (a) XRD patterns, (b) PL emission of $MAPbCl_3$ (blue line), $MAPbBr_3$ (orange line), $MAPbI_3$ (black line), $MAPb(Br_{0.9}I_{0.1})_3$ (red line), and $MAPb(Br_{0.8}Cl_{0.2})_3$ (green line) thin monocrystalline perovskites, and (c) Device architecture of perovskite memristor devices

Figure 40: EDX analysis of (a) $MAPb(Br_{0.8}Cl_{0.2})_3$ and (b) $MAPb(Br_{0.9}I_{0.1})_3$ perovskite monocrystals.

Figure 41: Profilometer measurements of (a) $MAPbCl_3$, (b) $MAPbBr_3$, (c) $MAPbI_3$, (d) $MAPb(Br_{0.9}I_{0.1})_3$, and (e) $MAPb(Br_{0.8}Cl_{0.2})_3$ MHPs monocrystal.

Figure 42: (a) Cyclic-voltammetry of $MAPbCl_3$ (blue line), $MAPbBr_3$ (orange line), $MAPbI_3$ (black line) monocrystal memristor devices. Endurance performance test conducted by applying

Figure 53: X-ray diffraction analysis of $MAPbCl_3$ (blue line), $MAPbBr_3$ (orange line), $MAPbI_3$ (black line), $MAPb(Br_{0.8}Cl_{0.2})_3$ (green line), and $MAPb(Br_{0.9}I_{0.1})_3$ (red line) of polycrystal perovskites.

Equations

$M(q) = \frac{d\Phi}{dq}$ equation 1

$\sigma = \frac{I}{VL}$ equation 2

$n_t = \frac{2\varepsilon\varepsilon_0 V_{TFL}}{qL^2}$ equation 3

$\mu = \frac{8L^3 J_D}{9\varepsilon\varepsilon_0 V_b^2}$ equation 4

$V_{TFL} = \frac{e n_t L^2}{2\varepsilon\varepsilon_0}$ equation 5

$CH_3NH_3PbBr_3 \rightleftharpoons CH_3NH_3^+ + Br^- + PbBr_2$ equation 6

$CH_3NH_3^+ + Br^- \rightarrow HBr(g) + CH_3NH_2(g)$ equation 7

$CH_3NH_2(ads) + O_2(g) \rightarrow HCOOH + NH_3(g)$ equation 8

$Z = \frac{\hat{V}}{\hat{J}} = \left[i\omega C_d + \frac{1}{R_L + i\omega L} + \frac{1}{R_L} + \frac{1}{R_C - \frac{1}{i\omega C_1}} \right]$ equation 9

$R_{rec} = \frac{\beta K_B T}{q j_{rec}}$ equation 10

$R_L = \frac{\gamma K_B T}{q j_{rec}}$ equation 11

$L = \frac{R_L}{\tau_{kin}}$ equation 12

$R_c = \frac{b\tau_{kin}}{C_1}$ equation 13

Tables

Table 1. Overview of different memristor devices based on polycrystal MHPs.

Structure	LRS/HRS ratio	V_{set} (V)	V_{reset} (V)	Endurance (cycles)	Retention (seconds)	Reference
FTO/MAPbI$_{3-x}$Cl$_x$/Au	10^4	1.47	-1.41	400	$4.68*10^4$	[243]
FTO/CsPbBr$_3$/Au	10^3	1.5	-1.2	100	10^3	[244]
Ag/CsPbBr$_3$/MoO$_3$/Ag	100	0.7	-0.8	50	10^4	[245]
ITO/MAPbI$_3$/Au	10	0.7	-0.61	500	10^4	[246]
ITO/PEDOT:PSS/MAPbBr$_3$/Al	$3.6*10^6$	-0.2	3	120	10^4	[247]
PET/ITO/MAPbI$_3$/Au	50	0.7	-0.5	400	10^4	[248]
PET/ITO/Cs$_3$Bi2I$_9$/Au	10^3	0.3	-0.5	10^3	10^4	[249]
FTO/c-TiO$_2$/MAPbI$_{3-x}$Cl$_x$/Al	$1.9*10^9$	1.10	-1.65	160	$2*10^3$	[126]
ITO/MAPbI$_3$/ZnO/Au	500	0.9	-1.5	100	10^4	[232]
ITO/PEDOT:PSS/MAPbI$_3$/Cu	10^4	-0.6	2	$3*10^3$	$3*10^4$	[250]
Si/SiO$_2$/Ti/Pt/MAPbI$_3$/Ag	10^6	0.13	-0.13	350	10^4	[251]
PET/ITO/PMMA/CsPbBr$_3$QDs/PMMA/Ag	$6*10^5$	2.6	-2.7	$5*10^3$	$4*10^5$	[252]
Ag/MAPbI$_3$/Au	10^8	1.16	0.46	10^3	10^4	[253]

Table 2. Calculation of defect density for monocrystal memristor devices. The V_{FTL} is extracted from the SCLC measurement.

Monocrystal	MAPbCl$_3$	MAPb(Br$_{0.8}$Cl$_{0.2}$)$_3$	MAPbBr$_3$	MAPb(Br$_{0.9}$I$_{0.1}$)$_3$	MAPbI$_3$
L (µm)	27	26.6	24.7	21.9	2.50
ε	23.9	25	25.5	25	18
V_{FTL} (V)	0.24	1.65	0.137	1.52	0.184
n_{t}	$8.72\cdot10^{11}$	$6.44\cdot10^{12}$	$6.33\cdot10^{11}$	$8.76\cdot10^{12}$	$5.86\cdot10^{11}$

Table 3. Calculation of defect density for polycrystal memristor devices. The V_{FTL} is extracted from the SCLC measurement.

Polycrystal	MAPbCl$_3$	MAPb(Br$_{0.8}$Cl$_{0.2}$)$_3$	MAPbBr$_3$	MAPb(Br$_{0.9}$I$_{0.1}$)$_3$	MAPbI$_3$
L (µm)	450	505	500	512	458
ε	23.9	25	25.5	25	18
V_{FTL} (V)	1.3	2.18	0.82	1.92	0.96
n_{t}	$1.70\cdot10^{16}$	$2.36\cdot10^{16}$	$9.25\cdot10^{15}$	$2.12\cdot10^{16}$	$9.34\cdot10^{15}$

Appendix B: List of constant and abbreviations

Abbreviations

Alternating Current AC

Ammonia NH_3

Antisolvent Vapor-assisted Crystallization AVC

Artificial Intelligence AI

Atomic Force Microscopy AFM

Binding Energy BE

Carbon Dioxide CO_2

Charge q

Conductivity σ

Contact Potential Difference CPD

Continuous-Wave CW

Current I

Current-Voltage I-V

Diffusion Length L_D

Dimethyl Sulfoxide DMSO

Dimethylformamide DMF

Electrochemical Metallization Mechanism ECM

Energy Dispersive X-ray EDX

Equivalent Circuit EC

External Quantum Efficiencies EQEs

Formic Acid HCOOH

Forward Scan FS

Full Width at Half Maximum FWHM

Grazing Incidence X-ray Diffraction GIXRD

Hafnium Oxide HfO_2

High Frequency HF

High-Resistance State HRS

Hydrogen Bromide HBr

Impedance Spectroscopy IS

Indium Tin Oxide ITO

Instrument Response Function IRF

Intermediate Frequency IF

Internet of Things IoT

Confined Inverse Temperature Crystallization CITC

Inverse Temperature Crystallization ITC

Inverted Hysteresis IH

Kelvin Probe Force Microscopy KPFM

Kinetic Energy KE

Kinetic Relaxation Times τ_{kin}

Lead(II) Bromide $PbBr_2$

Light Emitting Diodes LEDs

Low Frequencies LF

Low-Resistance State LRS

Magnetic Flux ϕ

Matrix-Vector Multiplication MVM

Metal Halide Perovskites MHPs

Methylamine CH_3NH_2)

Methylammonium Bromide MABr

Microampere μA

Micro-Photoluminescence μPL

Milliampere mA

Mobility μ

Molecular Oxygen O_2

Normal Hysteresis NH

Open-Circuit Voltage V_{OC}

Perovskite Solar Cells PSCs

Photoluminescence PL

Photomultiplier Tube PMT

Poly[bis(4-phenyl)(2,4,6-trimethylphenyl)amine PTAA

Polycrystalline PC

Polycrystalline Perovskite Solar Cells PC-PSCs

Polymethylmethacrylate PMMA

Power Conversion Efficiency PCE

Pre-trained Transformer GPT

Resistive Random-Access Memory ReRAM

Reverse Scan RS

Root-Mean-Square RMS

Scanning Electron Microscopy SEM

Scanning Photocurrent Microscopy SPCM

Single Crystal Perovskite Solar Cells SC-PSCs

Single-Crystal SC

Single-Crystal Metal Halide Perovskites SC-MHPs

Space-Charge-Limited Current SCLC

Spike-Timing-Dependent Plasticity STDP

Spiking Neural Networks SNNs

Surface Photovoltage SPV

Surface Polarization Model SPM

Tantalum Oxide TaO_x

Temperature-Cooling Crystallization TCC

Trap-Filled Limit TFL

Thin Single Crystal TSC

Time Resolved Photoluminescence TRPL

Time-Correlated Single Photon Counting TCSPC

Time-of-Flight TOF)

Time-Resolved Photoluminescence TRPL

Titanium Dioxide TiO_2

Transient Absorption Spectroscopy TAS

Transient Photovoltage TPV

Ultraviolet UV

Valence Change Mechanism VCM

Voltage V

Water H_2O

X-Ray Diffraction XRD

X-Ray Photoelectron Spectroscopy XPS

γ-butyrolactone GBL

Constants

Boltzmann constant	$k_B = 1.380649 \times 10^{-23}$ J/K
vacuum permittivity	$\varepsilon_0 = 8.854 \text{ x } 10^{-12}$ F/m
elementary charge	$q = 1.602\text{x}10^{-19}$ C

KEYWORDS

Metal halide perovskite

Single Crystal

Memristor

Neurmorphic computing

Multistate

Endurance

Surface modification

Synthesis

Compositional engineering

Structural engineering

LRS/HRS ratio

Photoluminescence

Non-volatile

Confined inverse temperature crystallization

LIST OF PUBLICATIONS

[1] I. Fernandez-Guillen *et al.*, «Boosting Photoluminescence in $MAPbBr_3$ Single Crystals through Laser-Based Surface Modification», *ACS Photonics*, vol. 10, n.º 12, pp. 4151-4159, dic. 2023, doi: 10.1021/acsphotonics.3c00777.

[2] I. Fernandez-Guillen *et al.*, «Perovskite Thin Single Crystal for a High Performance and Long Endurance Memristor», *Adv. Electron. Mater.*, vol. 10, n.º 5, p. 2300475, may 2024, doi: 10.1002/aelm.202300475.

[3] A. Liang *et al.*, «Reassigning the Pressure-Induced Phase Transitions of Methylammonium Lead Bromide Perovskite», *J. Am. Chem. Soc.*, vol. 144, n.º 43, pp. 20099-20108, nov. 2022, doi: 10.1021/jacs.2c09457.

[4] A. Liang *et al.*, «Pressure-Induced Phase Transition versus Amorphization in Hybrid Methylammonium Lead Bromide Perovskite», *J. Phys. Chem. C*, vol. 127, n.º 26, pp. 12821-12826, jul. 2023, doi: 10.1021/acs.jpcc.3c03263.

[5] J. Noguera-Gómez, I. Fernández-Guillen, P. F. Betancur, V. S. Chirvony, P. P. Boix, y R. Abargues, «Low-demanding in situ crystallization method for tunable and stable perovskite nanoparticle thin films», *Matter*, vol. 5, n.º 10, pp. 3541-3552, oct. 2022, doi: 10.1016/j.matt.2022.07.017.

[6] J. S. Solomon *et al.*, «Oriented 2D Ruddlesden-Popper metal halides by pulsed laser deposition», *Npj 2D Mater. Appl.*, vol. 9, n.º 1, p. 50, jun. 2025, doi: 10.1038/s41699-025-00571-3.

BIBLIOGRAPHY

[1] H. Werthner *et al.*, Eds., *Introduction to Digital Humanism: A Textbook*. Cham: Springer Nature Switzerland, 2024. doi: 10.1007/978-3-031-45304-5.

[2] E. Mollick, «Establishing Moore's Law», *IEEE Ann. Hist. Comput.*, vol. 28, n.º 3, pp. 62-75, jul. 2006, doi: 10.1109/MAHC.2006.45.

[3] I. L. Markov, «Limits on fundamental limits to computation», *Nature*, vol. 512, n.º 7513, pp. 147-154, ago. 2014, doi: 10.1038/nature13570.

[4] D. Le, B. Arig, M. Isik, I. C. Dikmen, y T. Karadag, «A Review of Memory Wall for Neuromorphic Computing», 24 de febrero de 2025, *arXiv*: arXiv:2502.16823. doi: 10.48550/arXiv.2502.16823.

[5] F. Zhu, P. Xu, y J. Zong, «Moore's Law: The potential, limits, and breakthroughs», *Appl. Comput. Eng.*, vol. 10, n.º 1, pp. 307-315, sep. 2023, doi: 10.54254/2755-2721/10/20230038.

[6] M. Hosseini, P. Gao, y C. Vivas-Valencia, «A social-environmental impact perspective of generative artificial intelligence», *Environ. Sci. Ecotechnology*, vol. 23, p. 100520, ene. 2025, doi: 10.1016/j.ese.2024.100520.

[7] D. R. E. Ewim, N. Ninduwezuor-Ehiobu, O. F. Orikpete, B. A. Egbokhaebho, A. A. Fawole, y C. Onunka, «Impact of Data Centers on Climate Change: A Review of Energy Efficient Strategies», *J. Eng. Exact Sci.*, vol. 9, n.º 6, pp. 16397-01e, ago. 2023, doi: 10.18540/jcecvl9iss6pp16397-01e.

[8] J. Domaradzki, D. Wojcieszak, T. Kotwica, y E. Mańkowska, «Memristors: a Short Review on Fundamentals, Structures, Materials and Applications», *Int. J. Electron. Telecommun.*, pp. 373-381, ene. 2020, doi: 10.24425/ijet.2020.131888.

[9] K. Roy, A. Jaiswal, y P. Panda, «Towards spike-based machine intelligence with neuromorphic computing», *Nature*, vol. 575, n.º 7784, pp. 607-617, nov. 2019, doi: 10.1038/s41586-019-1677-2.

[10] W. Chen *et al.*, «Essential Characteristics of Memristors for Neuromorphic Computing», *Adv. Electron. Mater.*, vol. 9, n.º 2, p. 2200833, feb. 2023, doi: 10.1002/aelm.202200833.

[11] R. Khan, N. U. Rehman, S. Iqbal, S. Abdullaev, y H. M. Aldosari, «Resistive Switching Properties in Memristors for Optoelectronic Synaptic Memristors: Deposition Techniques, Key Performance Parameters, and Applications», *ACS Appl. Electron. Mater.*, vol. 6, n.º 1, pp. 73-119, ene. 2024, doi: 10.1021/acsaelm.3c01323.

[12] C. D. Schuman, S. R. Young, B. P. Maldonado, y B. C. Kaul, «Real-Time Evolution and Deployment of Neuromorphic Computing at The Edge», en *2021 12th International Green and Sustainable Computing Conference (IGSC)*, Pullman, WA, USA: IEEE, oct. 2021, pp. 1-8. doi: 10.1109/IGSC54211.2021.9651607.

[13] C. D. Schuman, S. R. Kulkarni, M. Parsa, J. P. Mitchell, P. Date, y B. Kay, «Opportunities for neuromorphic computing algorithms and applications», *Nat. Comput. Sci.*, vol. 2, n.º 1, pp. 10-19, ene. 2022, doi: 10.1038/s43588-021-00184-y.

[14] A. Fedorova *et al.*, «Advancing Neural Networks: Innovations and Impacts on Energy Consumption», *Adv. Electron. Mater.*, vol. 10, n.º 12, p. 2400258, dic. 2024, doi: 10.1002/aelm.202400258.

[15] B. George, «THE ECONOMICS OF ENERGY EFFICIENCY: HUMAN COGNITION VS. AI LARGE LANGUAGE MODELS», vol. 14, n.º 2.

[16] K. Yamazaki, V.-K. Vo-Ho, D. Bulsara, y N. Le, «Spiking Neural Networks and Their Applications: A Review», *Brain Sci.*, vol. 12, n.º 7, p. 863, jun. 2022, doi: 10.3390/brainsci12070863.

[17] O. Elkabetz y N. Cohen, «Continuous vs. Discrete Optimization of Deep Neural Networks».

[18] C. Hong, X. Wei, J. Wang, B. Deng, H. Yu, y Y. Che, «Training Spiking Neural Networks for Cognitive Tasks: A Versatile Framework Compatible With Various Temporal Codes», *IEEE Trans.*

Neural Netw. Learn. Syst., vol. 31, n.º 4, pp. 1285-1296, abr. 2020, doi: 10.1109/TNNLS.2019.2919662.

[19] X. Zhang, A. Huang, Q. Hu, Z. Xiao, y P. K. Chu, «Neuromorphic Computing with Memristor Crossbar», *Phys. Status Solidi A*, vol. 215, n.º 13, p. 1700875, jul. 2018, doi: 10.1002/pssa.201700875.

[20] H. Li *et al.*, «Memristive Crossbar Arrays for Storage and Computing Applications», *Adv. Intell. Syst.*, vol. 3, n.º 9, p. 2100017, sep. 2021, doi: 10.1002/aisy.202100017.

[21] Y. Jeong y W. Lu, «Neuromorphic Computing Using Memristor Crossbar Networks: A Focus on Bio-Inspired Approaches», *IEEE Nanotechnol. Mag.*, vol. 12, n.º 3, pp. 6-18, sep. 2018, doi: 10.1109/MNANO.2018.2844901.

[22] J. Haase, «Parametrization of resistive crossbar arrays for vector matrix multiplication», en *Proceedings of the 9th International Workshop on Equation-based Object-oriented Modeling Languages and Tools*, Berlin Germany: ACM, nov. 2019, pp. 37-44. doi: 10.1145/3365984.3365987.

[23] Y. Zhang, P. Huang, B. Gao, J. Kang, y H. Wu, «Oxide-based filamentary RRAM for deep learning», *J. Phys. Appl. Phys.*, vol. 54, n.º 8, p. 083002, feb. 2021, doi: 10.1088/1361-6463/abc5e7.

[24] S. J. Kim, S. Kim, y H. W. Jang, «Competing memristors for brain-inspired computing», *iScience*, vol. 24, n.º 1, p. 101889, ene. 2021, doi: 10.1016/j.isci.2020.101889.

[25] L. Chua, «Memristor-The missing circuit element», *IEEE Trans. Circuit Theory*, vol. 18, n.º 5, pp. 507-519, 1971, doi: 10.1109/TCT.1971.1083337.

[26] D. B. Strukov, G. S. Snider, D. R. Stewart, y R. S. Williams, «The missing memristor found», *Nature*, vol. 453, n.º 7191, pp. 80-83, may 2008, doi: 10.1038/nature06932.

[27] P. Thakkar, J. Gosai, H. J. Gogoi, y A. Solanki, «From fundamentals to frontiers: a review of memristor mechanisms, modeling and emerging applications», *J. Mater. Chem. C*, vol. 12, n.º 5, pp. 1583-1608, 2024, doi: 10.1039/D3TC03692H.

[28] R. Wang *et al.*, «Recent Advances of Volatile Memristors: Devices, Mechanisms, and Applications», *Adv. Intell. Syst.*, vol. 2, n.º 9, p. 2000055, sep. 2020, doi: 10.1002/aisy.202000055.

[29] T. Moon *et al.*, «Leveraging volatile memristors in neuromorphic computing: from materials to system implementation», *Mater. Horiz.*, vol. 11, n.º 20, pp. 4840-4866, 2024, doi: 10.1039/D4MH00675E.

[30] X. Yan *et al.*, «Graphene Oxide Quantum Dots Based Memristors with Progressive Conduction Tuning for Artificial Synaptic Learning», *Adv. Funct. Mater.*, vol. 28, n.º 40, p. 1803728, oct. 2018, doi: 10.1002/adfm.201803728.

[31] B. Zhao, M. Xiao, y Y. N. Zhou, «Synaptic learning behavior of a TiO_2 nanowire memristor», *Nanotechnology*, vol. 30, n.º 42, p. 425202, oct. 2019, doi: 10.1088/1361-6528/ab3260.

[32] G. Zhou *et al.*, «Volatile and Nonvolatile Memristive Devices for Neuromorphic Computing», *Adv. Electron. Mater.*, vol. 8, n.º 7, p. 2101127, jul. 2022, doi: 10.1002/aelm.202101127.

[33] S. Pal, V. Gupta, W. H. Ki, y A. Islam, «Design and development of memristor-based RRAM», *IET Circuits Devices Syst.*, vol. 13, n.º 4, pp. 548-557, jul. 2019, doi: 10.1049/iet-cds.2018.5388.

[34] A. M. S. T. Abdelwahed, A. Neale, M. Anis, y L. Wei, «8T1R: A Novel Low-power High-speed RRAM-based Non-volatile SRAM Design», en *Proceedings of the 26th edition on Great Lakes Symposium on VLSI*, Boston Massachusetts USA: ACM, may 2016, pp. 239-244. doi: 10.1145/2902961.2903016.

[35] Y. Van De Burgt *et al.*, «A non-volatile organic electrochemical device as a low-voltage artificial synapse for neuromorphic computing», *Nat. Mater.*, vol. 16, n.º 4, pp. 414-418, abr. 2017, doi: 10.1038/nmat4856.

[36] H. Abbas *et al.*, «A memristor crossbar array of titanium oxide for non-volatile memory and neuromorphic applications», *Semicond. Sci. Technol.*, vol. 32, n.º 6, p. 065014, jun. 2017, doi: 10.1088/1361-6641/aa6a3a.

[37] M. A. Shakib, Z. Gao, y C. Lamuta, «Synaptic Properties of Geopolymer Memristors: Synaptic Plasticity, Spike-Rate-Dependent Plasticity, and Spike-Timing-Dependent Plasticity», *ACS Appl. Electron. Mater.*, vol. 5, n.º 9, pp. 4875-4884, sep. 2023, doi: 10.1021/acsaelm.3c00654.

[38] V. Milo *et al.*, «Multilevel HfO2-based RRAM devices for low-power neuromorphic networks», *APL Mater.*, vol. 7, n.º 8, p. 081120, ago. 2019, doi: 10.1063/1.5108650.

[39] L. Wang, Y. Wang, y D. Wen, «Switching-enhanced RRAM for reliable synaptic simulation and multilevel data storage», *J. Alloys Compd.*, vol. 892, p. 162180, feb. 2022, doi: 10.1016/j.jallcom.2021.162180.

[40] B. Mohammad *et al.*, «State of the art of metal oxide memristor devices», *Nanotechnol. Rev.*, vol. 5, n.º 3, ene. 2016, doi: 10.1515/ntrev-2015-0029.

[41] A. P. James, Ed., *Deep Learning Classifiers with Memristive Networks: Theory and Applications*, vol. 14. en Modeling and Optimization in Science and Technologies, vol. 14. Cham: Springer International Publishing, 2020. doi: 10.1007/978-3-030-14524-8.

[42] Y. Chen, G. Liu, C. Wang, W. Zhang, R.-W. Li, y L. Wang, «Polymer memristor for information storage and neuromorphic applications», *Mater. Horiz.*, vol. 1, n.º 5, p. 489, jun. 2014, doi: 10.1039/C4MH00067F.

[43] L. Yuan, S. Liu, W. Chen, F. Fan, y G. Liu, «Organic Memory and Memristors: From Mechanisms, Materials to Devices», *Adv. Electron. Mater.*, vol. 7, n.º 11, p. 2100432, nov. 2021, doi: 10.1002/aelm.202100432.

[44] Y. Li, «Challenges and Issues of Using Polymers as Structural Materials in MEMS: A Review», *J. Microelectromechanical Syst.*, vol. 27, n.º 4, pp. 581-598, ago. 2018, doi: 10.1109/JMEMS.2018.2837684.

[45] X. Xiao *et al.*, «Recent Advances in Halide Perovskite Memristors: Materials, Structures, Mechanisms, and Applications», *Adv. Mater. Technol.*, vol. 5, n.º 6, p. 1900914, jun. 2020, doi: 10.1002/admt.201900914.

[46] W. Peixiong *et al.*, «A mini review of recent progress on halide perovskite memristor devices: materials science, challenges and applications», *Mater. Today Energy*, vol. 45, p. 101692, oct. 2024, doi: 10.1016/j.mtener.2024.101692.

[47] Q. A. Akkerman y L. Manna, «What Defines a Halide Perovskite?», *ACS Energy Lett.*, vol. 5, n.º 2, pp. 604-610, feb. 2020, doi: 10.1021/acsenergylett.0c00039.

[48] Z. Xiao y Y. Yan, «Progress in Theoretical Study of Metal Halide Perovskite Solar Cell Materials», *Adv. Energy Mater.*, vol. 7, n.º 22, p. 1701136, nov. 2017, doi: 10.1002/aenm.201701136.

[49] J. Lim *et al.*, «Elucidating the long-range charge carrier mobility in metal halide perovskite thin films», *Energy Environ. Sci.*, vol. 12, n.º 1, pp. 169-176, 2019, doi: 10.1039/C8EE03395A.

[50] S. Adjokatse, H.-H. Fang, y M. A. Loi, «Broadly tunable metal halide perovskites for solid-state light-emission applications», *Mater. Today*, vol. 20, n.º 8, pp. 413-424, oct. 2017, doi: 10.1016/j.mattod.2017.03.021.

[51] Y. Cheng, Y. Peng, A. K.-Y. Jen, y H.-L. Yip, «Development and Challenges of Metal Halide Perovskite Solar Modules», *Sol. RRL*, vol. 6, n.º 3, p. 2100545, mar. 2022, doi: 10.1002/solr.202100545.

[52] Y. Wang y H. Sun, «All-Inorganic Metal Halide Perovskite Nanostructures: From Photophysics to Light-Emitting Applications», *Small Methods*, vol. 2, n.º 1, p. 1700252, ene. 2018, doi: 10.1002/smtd.201700252.

[53] I. Fernandez-Guillen *et al.*, «Perovskite Thin Single Crystal for a High Performance and Long Endurance Memristor», *Adv. Electron. Mater.*, vol. 10, n.º 5, p. 2300475, may 2024, doi: 10.1002/aelm.202300475.

[54] G. Kim y A. Petrozza, «Defect Tolerance and Intolerance in Metal-Halide Perovskites», *Adv. Energy Mater.*, vol. 10, n.º 37, p. 2001959, oct. 2020, doi: 10.1002/aenm.202001959.

[55] Z. Saki, M. M. Byranvand, N. Taghavinia, M. Kedia, y M. Saliba, «Solution-processed perovskite thin-films: the journey from lab- to large-scale solar cells», *Energy Environ. Sci.*, vol. 14, n.º 11, pp. 5690-5722, 2021, doi: 10.1039/D1EE02018H.

[56] G. Wang *et al.*, «Efficient perovskite solar cell fabricated in ambient air using one-step spin-coating», *RSC Adv.*, vol. 6, n.º 49, pp. 43299-43303, 2016, doi: 10.1039/C6RA05893K.

[57] N. J. Jeon, J. H. Noh, Y. C. Kim, W. S. Yang, S. Ryu, y S. I. Seok, «Solvent engineering for high-performance inorganic–organic hybrid perovskite solar cells», *Nat. Mater.*, vol. 13, n.º 9, pp. 897-903, sep. 2014, doi: 10.1038/nmat4014.

[58] P. Jia *et al.*, «The Trapped Charges at Grain Boundaries in Perovskite Solar Cells», *Adv. Funct. Mater.*, vol. 31, n.º 49, p. 2107125, dic. 2021, doi: 10.1002/adfm.202107125.

[59] J. S. Yun *et al.*, «Humidity-Induced Degradation via Grain Boundaries of $HC(NH_2)_2PbI_3$ Planar Perovskite Solar Cells», *Adv. Funct. Mater.*, vol. 28, n.º 11, p. 1705363, mar. 2018, doi: 10.1002/adfm.201705363.

[60] B. Murali, H. K. Kolli, J. Yin, R. Ketavath, O. M. Bakr, y O. F. Mohammed, «Single Crystals: The Next Big Wave of Perovskite Optoelectronics», *ACS Mater. Lett.*, vol. 2, n.º 2, pp. 184-214, feb. 2020, doi: 10.1021/acsmaterialslett.9b00290.

[61] B. Wenger, P. K. Nayak, X. Wen, S. V. Kesava, N. K. Noel, y H. J. Snaith, «Consolidation of the optoelectronic properties of CH3NH3PbBr3 perovskite single crystals», *Nat. Commun.*, vol. 8, n.º 1, p. 590, sep. 2017, doi: 10.1038/s41467-017-00567-8.

[62] Y. Cho, H. R. Jung, y W. Jo, «Halide perovskite single crystals: growth, characterization, and stability for optoelectronic applications», *Nanoscale*, vol. 14, n.º 26, pp. 9248-9277, 2022, doi: 10.1039/D2NR00513A.

[63] J. Li *et al.*, «Perovskite Single Crystals: Synthesis, Optoelectronic Properties, and Application», *Adv. Funct. Mater.*, vol. 31, n.º 11, p. 2008684, mar. 2021, doi: 10.1002/adfm.202008684.

[64] X. Jiang, X. Fu, D. Ju, S. Yang, Z. Chen, y X. Tao, «Designing Large-Area Single-Crystal Perovskite Solar Cells», *ACS Energy Lett.*, vol. 5, n.º 6, pp. 1797-1803, jun. 2020, doi: 10.1021/acsenergylett.0c00436.

[65] L. Chen *et al.*, «Surface Passivation of $MAPbBr_3$ Perovskite Single Crystals to Suppress Ion Migration and Enhance Photoelectronic Performance», *ACS Appl. Mater. Interfaces*, vol. 14, n.º 8, pp. 10917-10926, mar. 2022, doi: 10.1021/acsami.1c21948.

[66] X.-D. Wang *et al.*, «Surface passivated halide perovskite single-crystal for efficient photoelectrochemical synthesis of dimethoxydihydrofuran», *Nat. Commun.*, vol. 12, n.º 1, p. 1202, feb. 2021, doi: 10.1038/s41467-021-21487-8.

[67] J. Y. Kim, J.-W. Lee, H. S. Jung, H. Shin, y N.-G. Park, «High-Efficiency Perovskite Solar Cells», *Chem. Rev.*, vol. 120, n.º 15, pp. 7867-7918, ago. 2020, doi: 10.1021/acs.chemrev.0c00107.

[68] W. Zhao *et al.*, «Omnibearing Molecular-Locking of Perovskite Lattice Enables High-Performance Perovskite Solar Cells with Efficiency over 26%», *Adv. Funct. Mater.*, vol. 35, n.º 15, p. 2423096, abr. 2025, doi: 10.1002/adfm.202423096.

[69] F. Li, Y. Liang, y R. Zheng, «A balanced view of ion migration in halide perovskite electronics», *Newton*, vol. 1, n.º 3, p. 100096, may 2025, doi: 10.1016/j.newton.2025.100096.

[70] U. Erdil *et al.*, «Mimicking Outdoor Ion Migration in Perovskite Solar Cells: A Forward Bias, No-Light Accelerated Aging Approach», *ACS Energy Lett.*, vol. 10, n.º 3, pp. 1529-1537, mar. 2025, doi: 10.1021/acsenergylett.5c00376.

[71] K. T. Tanko *et al.*, «The Roles of Ion Migration on Perovskite Solar Cell Operational Stability at Various Illumination Intensities», *Sol. RRL*, p. 202500162, jun. 2025, doi: 10.1002/solr.202500162.

[72] R. Fukuda, T. Nishimura, M.-H. Yu, C.-C. Chueh, y A. Yamada, «Impact of Ionic Conduction on Hysteresis and Long-Term Degradation in Perovskite Solar Cells», *ACS Appl. Energy Mater.*, vol. 8, n.º 2, pp. 759-766, ene. 2025, doi: 10.1021/acsaem.4c01993.

[73] L. Munoz-Diaz *et al.*, «Inductive and Capacitive Hysteresis of Halide Perovskite Solar Cells and Memristors Under Illumination», *Front. Energy Res.*, vol. 10, p. 914115, jul. 2022, doi: 10.3389/fenrg.2022.914115.

[74] N. Onoda-Yamamuro, T. Matsuo, y H. Suga, «Dielectric study of CH3NH3PbX3 (X = Cl, Br, I)», *J. Phys. Chem. Solids*, vol. 53, n.º 7, pp. 935-939, jul. 1992, doi: 10.1016/0022-3697(92)90121-S.

[75] S. Ravishankar *et al.*, «Surface Polarization Model for the Dynamic Hysteresis of Perovskite Solar Cells», *J. Phys. Chem. Lett.*, vol. 8, n.º 5, pp. 915-921, mar. 2017, doi: 10.1021/acs.jpclett.7b00045.

[76] Y. Liu *et al.*, «Two-Inch-Sized Perovskite CH_3 NH_3 PbX_3 (X = Cl, Br, I) Crystals: Growth and Characterization», *Adv. Mater.*, vol. 27, n.º 35, pp. 5176-5183, sep. 2015, doi: 10.1002/adma.201502597.

[77] W. Wang *et al.*, «Growth of mixed-halide perovskite single crystals», *CrystEngComm*, vol. 20, n.º 12, pp. 1635-1643, 2018, doi: 10.1039/C7CE01691C.

[78] Y. Fang, Q. Dong, Y. Shao, Y. Yuan, y J. Huang, «Highly narrowband perovskite single-crystal photodetectors enabled by surface-charge recombination», *Nat. Photonics*, vol. 9, n.º 10, pp. 679-686, oct. 2015, doi: 10.1038/nphoton.2015.156.

[79] Q. Lin, D. J. Kubicki, M. Omrani, F. Alam, y M. Abdi-Jalebi, «The race between complicated multiple cation/anion compositions and stabilization of $FAPbI_3$ for halide perovskite solar cells», *J. Mater. Chem. C*, vol. 11, n.º 7, pp. 2449-2468, 2023, doi: 10.1039/D2TC04529J.

[80] R. Prasanna *et al.*, «Band Gap Tuning via Lattice Contraction and Octahedral Tilting in Perovskite Materials for Photovoltaics», *J. Am. Chem. Soc.*, vol. 139, n.º 32, pp. 11117-11124, ago. 2017, doi: 10.1021/jacs.7b04981.

[81] Y. Fang, H. Wei, Q. Dong, y J. Huang, «Quantification of re-absorption and re-emission processes to determine photon recycling efficiency in perovskite single crystals», *Nat. Commun.*, vol. 8, n.º 1, p. 14417, feb. 2017, doi: 10.1038/ncomms14417.

[82] M. Cinquino *et al.*, «Managing Growth and Dimensionality of Quasi 2D Perovskite Single-Crystalline Flakes for Tunable Excitons Orientation», *Adv. Mater.*, vol. 33, n.º 48, p. 2102326, dic. 2021, doi: 10.1002/adma.202102326.

[83] X. Dong *et al.*, «$MAPbX_3$ Perovskite Single Crystals for Advanced Optoelectronic Applications: Progress, Challenges, and Perspective», *Small*, vol. 21, n.º 11, p. 2412809, mar. 2025, doi: 10.1002/smll.202412809.

[84] D. Shi *et al.*, «Low trap-state density and long carrier diffusion in organolead trihalide perovskite single crystals», *Science*, vol. 347, n.º 6221, pp. 519-522, ene. 2015, doi: 10.1126/science.aaa2725.

[85] D. Kiermasch, A. Baumann, M. Fischer, V. Dyakonov, y K. Tvingstedt, «Revisiting lifetimes from transient electrical characterization of thin film solar cells; a capacitive concern evaluated for silicon, organic and perovskite devices», *Energy Environ. Sci.*, vol. 11, n.º 3, pp. 629-640, 2018, doi: 10.1039/C7EE03155F.

[86] T. Kirchartz, J. A. Márquez, M. Stolterfoht, y T. Unold, «Photoluminescence-Based Characterization of Halide Perovskites for Photovoltaics», *Adv. Energy Mater.*, vol. 10, n.º 26, p. 1904134, jul. 2020, doi: 10.1002/aenm.201904134.

[87] J. Bisquert, «Interpretation of the Recombination Lifetime in Halide Perovskite Devices by Correlated Techniques», *J. Phys. Chem. Lett.*, vol. 13, n.º 31, pp. 7320-7335, ago. 2022, doi: 10.1021/acs.jpclett.2c01776.

[88] S. Akel, A. Kulkarni, U. Rau, y T. Kirchartz, «Relevance of Long Diffusion Lengths for Efficient Halide Perovskite Solar Cells», *PRX Energy*, vol. 2, n.º 1, p. 013004, mar. 2023, doi: 10.1103/PRXEnergy.2.013004.

[89] E. A. Duijnstee, J. M. Ball, V. M. Le Corre, L. J. A. Koster, H. J. Snaith, y J. Lim, «Toward Understanding Space-Charge Limited Current Measurements on Metal Halide Perovskites», *ACS Energy Lett.*, vol. 5, n.º 2, pp. 376-384, feb. 2020, doi: 10.1021/acsenergylett.9b02720.

[90] Y. Liu *et al.*, «A 1300 mm^2 Ultrahigh-Performance Digital Imaging Assembly using High-Quality Perovskite Single Crystals», *Adv. Mater.*, vol. 30, n.º 29, p. 1707314, jul. 2018, doi: 10.1002/adma.201707314.

[91] Q. Dong *et al.*, «Electron-hole diffusion lengths > 175 µm in solution-grown CH_3 NH_3 PbI_3 single crystals», *Science*, vol. 347, n.º 6225, pp. 967-970, feb. 2015, doi: 10.1126/science.aaa5760.

[92] Z. Zuo *et al.*, «Enhanced Optoelectronic Performance on the (110) Lattice Plane of an $MAPbBr_3$ Single Crystal», *J. Phys. Chem. Lett.*, vol. 8, n.º 3, pp. 684-689, feb. 2017, doi: 10.1021/acs.jpclett.6b02812.

[93] Y. Ma *et al.*, «Suppressing Ion Migration across Perovskite Grain Boundaries by Polymer Additives», *Adv. Funct. Mater.*, vol. 31, n.º 3, p. 2006802, ene. 2021, doi: 10.1002/adfm.202006802.

[94] H. Zai, Y. Ma, Q. Chen, y H. Zhou, «Ion migration in halide perovskite solar cells: Mechanism, characterization, impact and suppression», *J. Energy Chem.*, vol. 63, pp. 528-549, dic. 2021, doi: 10.1016/j.jechem.2021.08.006.

[95] C. Eames, J. M. Frost, P. R. F. Barnes, B. C. O'Regan, A. Walsh, y M. S. Islam, «Ionic transport in hybrid lead iodide perovskite solar cells», *Nat. Commun.*, vol. 6, n.º 1, p. 7497, jun. 2015, doi: 10.1038/ncomms8497.

[96] X. Xiao *et al.*, «Suppressed Ion Migration along the In-Plane Direction in Layered Perovskites», *ACS Energy Lett.*, vol. 3, n.º 3, pp. 684-688, mar. 2018, doi: 10.1021/acsenergylett.8b00047.

[97] J. Jiang *et al.*, «Synergistic strain engineering of perovskite single crystals for highly stable and sensitive X-ray detectors with low-bias imaging and monitoring», *Nat. Photonics*, vol. 16, n.º 8, pp. 575-581, ago. 2022, doi: 10.1038/s41566-022-01024-9.

[98] Y. Zhang, Y. Liu, Z. Xu, Z. Yang, y S. (Frank) Liu, «2D Perovskite Single Crystals with Suppressed Ion Migration for High-Performance Planar-Type Photodetectors», *Small*, vol. 16, n.º 42, p. 2003145, oct. 2020, doi: 10.1002/smll.202003145.

[99] W. Xu *et al.*, «In-situ passivating surface defects of ultra-thin MAPbBr3 perovskite single crystal films for high performance photodetectors», *Chin. J. Struct. Chem.*, vol. 44, n.º 1, p. 100454, ene. 2025, doi: 10.1016/j.cjsc.2024.100454.

[100] X. Guo *et al.*, «Mitigating Surface Deficiencies of Perovskite Single Crystals Enables Efficient Solar Cells with Enhanced Moisture and Reverse-Bias Stability», *Adv. Funct. Mater.*, vol. 33, n.º 22, p. 2213995, may 2023, doi: 10.1002/adfm.202213995.

[101] Y. Liu *et al.*, «20-mm-Large Single-Crystalline Formamidinium-Perovskite Wafer for Mass Production of Integrated Photodetectors», *Adv. Opt. Mater.*, vol. 4, n.º 11, pp. 1829-1837, nov. 2016, doi: 10.1002/adom.201600327.

[102] J. Siekmann, S. Ravishankar, y T. Kirchartz, «Apparent Defect Densities in Halide Perovskite Thin Films and Single Crystals», *ACS Energy Lett.*, vol. 6, n.º 9, pp. 3244-3251, sep. 2021, doi: 10.1021/acsenergylett.1c01449.

[103] D. Kim *et al.*, «Probing Facet-Dependent Surface Defects in $MAPbI_3$ Perovskite Single Crystals», *J. Phys. Chem. C*, vol. 123, n.º 23, pp. 14144-14151, jun. 2019, doi: 10.1021/acs.jpcc.9b00943.

[104] W.-G. Li, H.-S. Rao, B.-X. Chen, X.-D. Wang, y D.-B. Kuang, «A formamidinium–methylammonium lead iodide perovskite single crystal exhibiting exceptional optoelectronic properties and long-term stability», *J. Mater. Chem. A*, vol. 5, n.º 36, pp. 19431-19438, 2017, doi: 10.1039/C7TA04608A.

[105] S. Kundu y T. L. Kelly, «In situ studies of the degradation mechanisms of perovskite solar cells», *EcoMat*, vol. 2, n.º 2, p. e12025, jun. 2020, doi: 10.1002/eom2.12025.

[106] J. Rappich, F. Lang, V. V. Brus, O. Shargaieva, T. Dittrich, y N. H. Nickel, «Light-Induced Defect Generation in CH_3 NH_3 PbI_3 Thin Films and Single Crystals», *Sol. RRL*, vol. 4, n.º 2, p. 1900216, feb. 2020, doi: 10.1002/solr.201900216.

[107] Z. Zhang, W. Kim, M. J. Ko, y Y. Li, «Perovskite single-crystal thin films: preparation, surface engineering, and application», *Nano Converg.*, vol. 10, n.º 1, p. 23, may 2023, doi: 10.1186/s40580-023-00373-7.

[108] J. Yan *et al.*, «Advances in the Synthesis of Halide Perovskite Single Crystals for Optoelectronic Applications», *Chem. Mater.*, vol. 35, n.º 7, pp. 2683-2712, abr. 2023, doi: 10.1021/acs.chemmater.2c03505.

[109] X. Shi *et al.*, «Vapor Phase Growth of Air-Stable Hybrid Perovskite $FAPbBr_3$ Single-Crystalline Nanosheets», *Nano Lett.*, vol. 24, n.º 7, pp. 2299-2307, feb. 2024, doi: 10.1021/acs.nanolett.3c04604.

[110] R. M. Muslimawati, M. Manawan, K. Takahashi, Y. Furukawa, y A. Bahtiar, «Single Crystal Perovskite $MAPbBr_3$ Prepared by Using Anti-solvent Vapor-assisted Crystallization Method», *J. Phys. Conf. Ser.*, vol. 2376, n.º 1, p. 012005, nov. 2022, doi: 10.1088/1742-6596/2376/1/012005.

[111] H. Shen, R. Nan, Z. Jian, y X. Li, «Defect step controlled growth of perovskite MAPbBr3 single crystal», *J. Mater. Sci.*, vol. 54, n.º 17, pp. 11596-11603, sep. 2019, doi: 10.1007/s10853-019-03710-6.

[112] M. I. Saidaminov *et al.*, «High-quality bulk hybrid perovskite single crystals within minutes by inverse temperature crystallization», *Nat. Commun.*, vol. 6, n.º 1, p. 7586, jul. 2015, doi: 10.1038/ncomms8586.

[113] Y. Zhang, Y. Liu, y S. (Frank) Liu, «Composition Engineering of Perovskite Single Crystals for High-Performance Optoelectronics», *Adv. Funct. Mater.*, vol. 33, n.º 9, p. 2210335, feb. 2023, doi: 10.1002/adfm.202210335.

[114] Z. Lv *et al.*, «Recent advances in space-confined synthesis of perovskite single-crystal thin films», *Mater. Today Nano*, vol. 29, p. 100550, mar. 2025, doi: 10.1016/j.mtnano.2024.100550.

[115] M. N. Lintangpradipto *et al.*, «Single-Crystal Methylammonium-Free Perovskite Solar Cells with Efficiencies Exceeding 24% and High Thermal Stability», *ACS Energy Lett.*, vol. 8, n.º 11, pp. 4915-4922, nov. 2023, doi: 10.1021/acsenergylett.3c01935.

[116] S. Han *et al.*, «Halide Tunable Perovskite Single Crystals as Efficient Photodetector», *Adv. Funct. Mater.*, vol. 35, n.º 17, p. 2421770, abr. 2025, doi: 10.1002/adfm.202421770.

[117] Y. Xu *et al.*, «Solution-Processed Epitaxial Growth of MAPbI3 Single-Crystal Films for Highly Stable Photodetectors», *Front. Mater.*, vol. 8, p. 651957, abr. 2021, doi: 10.3389/fmats.2021.651957.

[118] C. Wang *et al.*, «Metal Halide Perovskite Single Crystals toward Electroluminescent Applications», *Adv. Funct. Mater.*, vol. 35, n.º 21, p. 2401189, may 2025, doi: 10.1002/adfm.202401189.

[119] H. Zhang *et al.*, «High-Luminance Microsized CH_3 NH_3 $PbBr_3$ Single-Crystal-Based Light-Emitting Diodes via a Facile Liquid-Insulator Bridging Route», *ACS Nano*, vol. 16, n.º 4, pp. 6394-6403, abr. 2022, doi: 10.1021/acsnano.2c00488.

[120] Q. Zhang, S. T. Ha, X. Liu, T. C. Sum, y Q. Xiong, «Room-Temperature Near-Infrared High-Q Perovskite Whispering-Gallery Planar Nanolasers», *Nano Lett.*, vol. 14, n.º 10, pp. 5995-6001, oct. 2014, doi: 10.1021/nl503057g.

[121] J. Xing *et al.*, «Modulating the optical and electrical properties of MAPbBr3 single crystals via voltage regulation engineering and application in memristors», *Light Sci. Appl.*, vol. 9, n.º 1, p. 111, jun. 2020, doi: 10.1038/s41377-020-00349-w.

[122] H. Tian *et al.*, «Extremely Low Operating Current Resistive Memory Based on Exfoliated 2D Perovskite Single Crystals for Neuromorphic Computing», *ACS Nano*, vol. 11, n.º 12, pp. 12247-12256, dic. 2017, doi: 10.1021/acsnano.7b05726.

[123] J. Cui, X. Fu, H. Zhou, J. Yin, M. Wu, y X. Zhang, «Synthesis, structure, mobility and memristor properties of tetragonal CH_3 NH_3 $PbBr_3$ perovskite single crystals», *Dalton Trans.*, vol. 50, n.º 30, pp. 10365-10368, 2021, doi: 10.1039/D1DT00492A.

[124] Y. Xiao *et al.*, «A review of memristor: material and structure design, device performance, applications and prospects», *Sci. Technol. Adv. Mater.*, vol. 24, n.º 1, p. 2162323, dic. 2023, doi: 10.1080/14686996.2022.2162323.

[125] T. Zhang, C. Hu, y S. Yang, «Ion Migration: A "Double-Edged Sword" for Halide-Perovskite-Based Electronic Devices», *Small Methods*, vol. 4, n.º 5, p. 1900552, may 2020, doi: 10.1002/smtd.201900552.

[126] K. Yan *et al.*, «High-performance perovskite memristor based on methyl ammonium lead halides», *J. Mater. Chem. C*, vol. 4, n.º 7, pp. 1375-1381, 2016, doi: 10.1039/c6tc00141f.

[127] A. Bou, C. Gonzales, P. P. Boix, Y. Vaynzof, A. Guerrero, y J. Bisquert, «Kinetics of Volatile and Nonvolatile Halide Perovskite Devices: The Conductance-Activated Quasi-Linear Memristor (CALM) Model», *J. Phys. Chem. Lett.*, vol. 16, n.º 1, pp. 69-76, ene. 2025, doi: 10.1021/acs.jpclett.4c03132.

[128] W. Zhang *et al.*, «Chemical passivation and grain-boundary manipulation via in situ cross-linking strategy for scalable flexible perovskite solar cells», *Sci. Adv.*, vol. 11, n.º 5, p. eadr2290, ene. 2025, doi: 10.1126/sciadv.adr2290.

[129] C. Wang *et al.*, «Crystallization and Defect Chemistry Dual Engineering for $MAPbI_3$ Perovskite Solar Cells with Efficiency Approaching 22%», *ACS Sustain. Chem. Eng.*, vol. 10, n.º 51, pp. 17318-17326, dic. 2022, doi: 10.1021/acssuschemeng.2c05816.

[130] P. Schouwink *et al.*, «Structure and properties of complex hydride perovskite materials», *Nat. Commun.*, vol. 5, n.º 1, p. 5706, dic. 2014, doi: 10.1038/ncomms6706.

[131] L. Li, Y. Chen, C. Cai, P. Ma, H. Ji, y G. Zou, «Single Crystal Halide Perovskite Film for Nonlinear Resistive Memory with Ultrahigh Switching Ratio», *Small*, vol. 18, n.º 3, p. 2103881, ene. 2022, doi: 10.1002/smll.202103881.

[132] J. S. Han *et al.*, «Lead-Free All-Inorganic Cesium Tin Iodide Perovskite for Filamentary and Interface-Type Resistive Switching toward Environment-Friendly and Temperature-Tolerant Nonvolatile Memories», *ACS Appl. Mater. Interfaces*, vol. 11, n.º 8, pp. 8155-8163, feb. 2019, doi: 10.1021/acsami.8b15769.

[133] X. Guan *et al.*, «Light-Responsive Ion-Redistribution-Induced Resistive Switching in Hybrid Perovskite Schottky Junctions», *Adv. Funct. Mater.*, vol. 28, n.º 3, p. 1704665, ene. 2018, doi: 10.1002/adfm.201704665.

[134] S.-Y. Kim, H. Zhang, y J. Rubio-Magnieto, «Operating Mechanism Principles and Advancements for Halide Perovskite-Based Memristors and Neuromorphic Devices», *J. Phys. Chem. Lett.*, vol. 15, n.º 40, pp. 10087-10103, oct. 2024, doi: 10.1021/acs.jpclett.4c02170.

[135] S. Poblador, M. Maestro-Izquierdo, M. Zabala, M. B. González, y F. Campabadal, «Methodology for the characterization and observation of filamentary spots in HfOx-based memristor devices», *Microelectron. Eng.*, vol. 223, p. 111232, feb. 2020, doi: 10.1016/j.mee.2020.111232.

[136] J. C. Pérez-Martínez *et al.*, «Role of Metal Contacts on Halide Perovskite Memristors», *Adv. Funct. Mater.*, vol. 33, n.º 47, p. 2305211, nov. 2023, doi: 10.1002/adfm.202305211.

[137] A. Solanki, A. Guerrero, Q. Zhang, J. Bisquert, y T. C. Sum, «Interfacial Mechanism for Efficient Resistive Switching in Ruddlesden–Popper Perovskites for Non-volatile Memories», *J. Phys. Chem. Lett.*, vol. 11, n.º 2, pp. 463-470, ene. 2020, doi: 10.1021/acs.jpclett.9b03181.

[138] X. Zhao, H. Xu, Z. Wang, Y. Lin, y Y. Liu, «Memristors with organic-inorganic halide perovskites», *InfoMat*, vol. 1, n.º 2, pp. 183-210, jun. 2019, doi: 10.1002/inf2.12012.

[139] S. Lee, W. B. Kim, J. M. Lee, H. J. Kim, J. H. Choi, y H. S. Jung, «Oxide Passivation of Halide Perovskite Resistive Memory Device: A Strategy for Overcoming Endurance Problem», *ACS Appl. Mater. Interfaces*, vol. 13, n.º 37, pp. 44577-44584, sep. 2021, doi: 10.1021/acsami.1c13210.

[140] B. Jiang *et al.*, «Advances in Metal Halide Perovskite Memristors: A Review from a Co-Design Perspective», *Adv. Sci.*, vol. 12, n.º 2, p. 2409291, ene. 2025, doi: 10.1002/advs.202409291.

[141] X. Zhang, X. Zhao, y Z. Wang, «Polyacrylonitrile Passivation for Enhancing the Optoelectronic Switching Performance of Halide Perovskite Memristor for Image Boolean Logic Applications», *Nanomaterials*, vol. 13, n.º 15, p. 2174, jul. 2023, doi: 10.3390/nano13152174.

[142] E. Yoo *et al.*, «Strategic extended air stability of organolead halide perovskite nonvolatile memory devices», *J. Alloys Compd.*, vol. 811, p. 151999, nov. 2019, doi: 10.1016/j.jallcom.2019.151999.

[143] M. Patel, D. D. Kumbhar, J. Gosai, M. R. Sekhar, A. T. Mallajosyula, y A. Solanki, «Hybrid Perovskite-Based Flexible and Stable Memristor by Complete Solution Process for Neuromorphic Computing», *Adv. Electron. Mater.*, vol. 9, n.º 4, p. 2200908, abr. 2023, doi: 10.1002/aelm.202200908.

[144] Y. Wang *et al.*, «Self-learning effect of CsFAMAPbIBr memristor achieved by electroforming process», *Mater. Chem. Phys.*, vol. 310, p. 128488, dic. 2023, doi: 10.1016/j.matchemphys.2023.128488.

[145] X. Zhao *et al.*, «Photoassisted Electroforming Method for Reliable Low-Power Organic–Inorganic Perovskite Memristors», *Adv. Funct. Mater.*, vol. 30, n.º 17, p. 1910151, abr. 2020, doi: 10.1002/adfm.201910151.

[146] C. Gonzales y A. Guerrero, «Mechanistic and Kinetic Analysis of Perovskite Memristors with Buffer Layers: The Case of a Two-Step Set Process», *J. Phys. Chem. Lett.*, vol. 14, n.º 6, pp. 1395-1402, feb. 2023, doi: 10.1021/acs.jpclett.2c03669.

[147] J. Xing *et al.*, «Thickness-dependent carrier lifetime and mobility for MAPbBr3 single crystals», *Mater. Today Phys.*, vol. 14, p. 100240, ago. 2020, doi: 10.1016/j.mtphys.2020.100240.

[148] A. Guerrero, J. Bisquert, y G. Garcia-Belmonte, «Impedance Spectroscopy of Metal Halide Perovskite Solar Cells from the Perspective of Equivalent Circuits», *Chem. Rev.*, vol. 121, n.º 23, pp. 14430-14484, dic. 2021, doi: 10.1021/acs.chemrev.1c00214.

[149] «A decade of perovskite photovoltaics», *Nat. Energy*, vol. 4, n.º 1, pp. 1-1, ene. 2019, doi: 10.1038/s41560-018-0323-9.

[150] J. Burschka *et al.*, «Sequential deposition as a route to high-performance perovskite-sensitized solar cells», *Nature*, vol. 499, n.º 7458, pp. 316-319, jul. 2013, doi: 10.1038/nature12340.

[151] G. E. Eperon, S. D. Stranks, C. Menelaou, M. B. Johnston, L. M. Herz, y H. J. Snaith, «Formamidinium lead trihalide: a broadly tunable perovskite for efficient planar heterojunction solar cells», *Energy Environ. Sci.*, vol. 7, n.º 3, p. 982, 2014, doi: 10.1039/c3ee43822h.

[152] J. Zhou y J. Huang, «Photodetectors Based on Organic–Inorganic Hybrid Lead Halide Perovskites», *Adv. Sci.*, vol. 5, n.º 1, p. 1700256, ene. 2018, doi: 10.1002/advs.201700256.

[153] L. Lei, Q. Dong, K. Gundogdu, y F. So, «Metal Halide Perovskites for Laser Applications», *Adv. Funct. Mater.*, vol. 31, n.º 16, p. 2010144, abr. 2021, doi: 10.1002/adfm.202010144.

[154] X.-K. Liu *et al.*, «Metal halide perovskites for light-emitting diodes», *Nat. Mater.*, vol. 20, n.º 1, pp. 10-21, ene. 2021, doi: 10.1038/s41563-020-0784-7.

[155] N.-G. Park, «Perovskite solar cells: an emerging photovoltaic technology», *Mater. Today*, vol. 18, n.º 2, pp. 65-72, mar. 2015, doi: 10.1016/j.mattod.2014.07.007.

[156] H. J. Snaith, «Perovskites: The Emergence of a New Era for Low-Cost, High-Efficiency Solar Cells», *J. Phys. Chem. Lett.*, vol. 4, n.º 21, pp. 3623-3630, nov. 2013, doi: 10.1021/jz4020162.

[157] T. M. Brenner, D. A. Egger, L. Kronik, G. Hodes, y D. Cahen, «Hybrid organic—inorganic perovskites: low-cost semiconductors with intriguing charge-transport properties», *Nat. Rev. Mater.*, vol. 1, n.º 1, p. 15007, ene. 2016, doi: 10.1038/natrevmats.2015.7.

[158] T. S. Sherkar *et al.*, «Recombination in Perovskite Solar Cells: Significance of Grain Boundaries, Interface Traps, and Defect Ions», *ACS Energy Lett.*, vol. 2, n.º 5, pp. 1214-1222, may 2017, doi: 10.1021/acsenergylett.7b00236.

[159] M. B. Johnston y L. M. Herz, «Hybrid Perovskites for Photovoltaics: Charge-Carrier Recombination, Diffusion, and Radiative Efficiencies», *Acc. Chem. Res.*, vol. 49, n.º 1, pp. 146-154, ene. 2016, doi: 10.1021/acs.accounts.5b00411.

[160] J. Jeong *et al.*, «Pseudo-halide anion engineering for α-FAPbI3 perovskite solar cells», *Nature*, vol. 592, n.º 7854, pp. 381-385, abr. 2021, doi: 10.1038/s41586-021-03406-5.

[161] C. Lin, «Stabilizing Organic–Inorganic Lead Halide Perovskite Solar Cells With Efficiency Beyond 20%», *Front. Chem.*, vol. 8, p. 592, jul. 2020, doi: 10.3389/fchem.2020.00592.

[162] Q. Wang *et al.*, «Scaling behavior of moisture-induced grain degradation in polycrystalline hybrid perovskite thin films», *Energy Environ. Sci.*, vol. 10, n.º 2, pp. 516-522, 2017, doi: 10.1039/C6EE02941H.

[163] T. Leijtens *et al.*, «Carrier trapping and recombination: the role of defect physics in enhancing the open circuit voltage of metal halide perovskite solar cells», *Energy Environ. Sci.*, vol. 9, n.º 11, pp. 3472-3481, 2016, doi: 10.1039/C6EE01729K.

[164] S. P. Dunfield *et al.*, «From Defects to Degradation: A Mechanistic Understanding of Degradation in Perovskite Solar Cell Devices and Modules», *Adv. Energy Mater.*, vol. 10, n.º 26, p. 1904054, jul. 2020, doi: 10.1002/aenm.201904054.

[165] J.-W. Lee, S.-H. Bae, N. De Marco, Y.-T. Hsieh, Z. Dai, y Y. Yang, «The role of grain boundaries in perovskite solar cells», *Mater. Today Energy*, vol. 7, pp. 149-160, mar. 2018, doi: 10.1016/j.mtener.2017.07.014.

[166] N. Phung *et al.*, «The Role of Grain Boundaries on Ionic Defect Migration in Metal Halide Perovskites», *Adv. Energy Mater.*, vol. 10, n.º 20, p. 1903735, may 2020, doi: 10.1002/aenm.201903735.

[167] A. Zohar, M. Kulbak, I. Levine, G. Hodes, A. Kahn, y D. Cahen, «What Limits the Open-Circuit Voltage of Bromide Perovskite-Based Solar Cells?», *ACS Energy Lett.*, vol. 4, n.º 1, pp. 1-7, ene. 2019, doi: 10.1021/acsenergylett.8b01920.

[168] J.-P. Correa-Baena *et al.*, «Identifying and suppressing interfacial recombination to achieve high open-circuit voltage in perovskite solar cells», *Energy Environ. Sci.*, vol. 10, n.º 5, pp. 1207-1212, 2017, doi: 10.1039/C7EE00421D.

[169] M. I. Saidaminov, A. L. Abdelhady, G. Maculan, y O. M. Bakr, «Retrograde solubility of formamidinium and methylammonium lead halide perovskites enabling rapid single crystal growth», *Chem. Commun.*, vol. 51, n.º 100, pp. 17658-17661, 2015, doi: 10.1039/C5CC06916E.

[170] Y. Liu *et al.*, «Low-temperature-gradient crystallization for multi-inch high-quality perovskite single crystals for record performance photodetectors», *Mater. Today*, vol. 22, pp. 67-75, ene. 2019, doi: 10.1016/j.mattod.2018.04.002.

[171] A. Y. Alsalloum *et al.*, «Low-Temperature Crystallization Enables 21.9% Efficient Single-Crystal $MAPbI_3$ Inverted Perovskite Solar Cells», *ACS Energy Lett.*, vol. 5, n.º 2, pp. 657-662, feb. 2020, doi: 10.1021/acsenergylett.9b02787.

[172] L. Qiu, S. He, L. K. Ono, y Y. Qi, «Progress of Surface Science Studies on ABX_3 -Based Metal Halide Perovskite Solar Cells», *Adv. Energy Mater.*, vol. 10, n.º 48, p. 2003594, dic. 2020, doi: 10.1002/aenm.202003594.

[173] S. Bonabi Naghadeh, B. Luo, G. Abdelmageed, Y.-C. Pu, C. Zhang, y J. Z. Zhang, «Photophysical Properties and Improved Stability of Organic–Inorganic Perovskite by Surface Passivation», *J. Phys. Chem. C*, vol. 122, n.º 28, pp. 15799-15818, jul. 2018, doi: 10.1021/acs.jpcc.8b03681.

[174] R. Wang *et al.*, «Constructive molecular configurations for surface-defect passivation of perovskite photovoltaics», *Science*, vol. 366, n.º 6472, pp. 1509-1513, dic. 2019, doi: 10.1126/science.aay9698.

[175] J. Li, B. Li, G. Yang, D. Zheng, y J. Yu, «Crystallization and defects regulation of efficient inverted perovskite solar cells via glycine ethyl ester hydrochloride», *Appl. Surf. Sci.*, vol. 608, p. 155269, ene. 2023, doi: 10.1016/j.apsusc.2022.155269.

[176] M. Kedia *et al.*, «Light Makes Right: Laser Polishing for Surface Modification of Perovskite Solar Cells», *ACS Energy Lett.*, vol. 8, n.º 6, pp. 2603-2610, jun. 2023, doi: 10.1021/acsenergylett.3c00469.

[177] Y.-C. Zhao, W.-K. Zhou, X. Zhou, K.-H. Liu, D.-P. Yu, y Q. Zhao, «Quantification of light-enhanced ionic transport in lead iodide perovskite thin films and its solar cell applications», *Light Sci. Appl.*, vol. 6, n.º 5, pp. e16243-e16243, oct. 2016, doi: 10.1038/lsa.2016.243.

[178] H. Wang *et al.*, «Ligand-Modulated Excess PbI_2 Nanosheets for Highly Efficient and Stable Perovskite Solar Cells», *Adv. Mater.*, vol. 32, n.º 21, p. 2000865, may 2020, doi: 10.1002/adma.202000865.

[179] Y. Zhao *et al.*, «Double-Side-Passivated Perovskite Solar Cells with Ultra-low Potential Loss», *Sol. RRL*, vol. 3, n.º 2, p. 1800296, feb. 2019, doi: 10.1002/solr.201800296.

[180] B. Shi *et al.*, «Unraveling the Passivation Process of PbI_2 to Enhance the Efficiency of Planar Perovskite Solar Cells», *J. Phys. Chem. C*, vol. 122, n.º 37, pp. 21269-21276, sep. 2018, doi: 10.1021/acs.jpcc.8b08075.

[181] Y. C. Kim *et al.*, «Beneficial Effects of PbI_2 Incorporated in Organo-Lead Halide Perovskite Solar Cells», *Adv. Energy Mater.*, vol. 6, n.º 4, p. 1502104, feb. 2016, doi: 10.1002/aenm.201502104.

[182] Q. Chen *et al.*, «Controllable Self-Induced Passivation of Hybrid Lead Iodide Perovskites toward High Performance Solar Cells», *Nano Lett.*, vol. 14, n.º 7, pp. 4158-4163, jul. 2014, doi: 10.1021/nl501838y.

[183] G. Li *et al.*, «Effect of PbI2 passivation to grain boundary of perovskite film with cation and anion co-mixing on performance of photovoltaic devices», *Mater. Lett.*, vol. 273, p. 127979, ago. 2020, doi: 10.1016/j.matlet.2020.127979.

[184] D. Bi, A. M. El-Zohry, A. Hagfeldt, y G. Boschloo, «Unraveling the Effect of PbI_2 Concentration on Charge Recombination Kinetics in Perovskite Solar Cells», *ACS Photonics*, vol. 2, n.º 5, pp. 589-594, may 2015, doi: 10.1021/ph500255t.

[185] C. Luo, Y. Zhao, X. Wang, F. Gao, y Q. Zhao, «Self-Induced Type-I Band Alignment at Surface Grain Boundaries for Highly Efficient and Stable Perovskite Solar Cells», *Adv. Mater.*, vol. 33, n.º 40, p. 2103231, oct. 2021, doi: 10.1002/adma.202103231.

[186] D. Meggiolaro *et al.*, «Energy Level Tuning at the $MAPbI_3$ Perovskite/Contact Interface Using Chemical Treatment», *ACS Energy Lett.*, vol. 4, n.º 9, pp. 2181-2184, sep. 2019, doi: 10.1021/acsenergylett.9b01584.

[187] X. Chi *et al.*, «Elucidating Surface and Bulk Emission in 3D Hybrid Organic–Inorganic Lead Bromide Perovskites», *Adv. Opt. Mater.*, vol. 6, n.º 15, p. 1800470, ago. 2018, doi: 10.1002/adom.201800470.

[188] A. Merdasa *et al.*, «Impact of Excess Lead Iodide on the Recombination Kinetics in Metal Halide Perovskites», *ACS Energy Lett.*, vol. 4, n.º 6, pp. 1370-1378, jun. 2019, doi: 10.1021/acsenergylett.9b00774.

[189] A. Merdasa, M. Bag, Y. Tian, E. Källman, A. Dobrovolsky, y I. G. Scheblykin, «Super-Resolution Luminescence Microspectroscopy Reveals the Mechanism of Photoinduced Degradation in CH_3 NH_3 PbI_3 Perovskite Nanocrystals», *J. Phys. Chem. C*, vol. 120, n.º 19, pp. 10711-10719, may 2016, doi: 10.1021/acs.jpcc.6b03512.

[190] W. Peng *et al.*, «Solution-Grown Monocrystalline Hybrid Perovskite Films for Hole-Transporter-Free Solar Cells», *Adv. Mater.*, vol. 28, n.º 17, pp. 3383-3390, may 2016, doi: 10.1002/adma.201506292.

[191] B. Wu *et al.*, «Discerning the Surface and Bulk Recombination Kinetics of Organic–Inorganic Halide Perovskite Single Crystals», *Adv. Energy Mater.*, vol. 6, n.º 14, p. 1600551, jul. 2016, doi: 10.1002/aenm.201600551.

[192] N. Droseros, D. Tsokkou, y N. Banerji, «Photophysics of Methylammonium Lead Tribromide Perovskite: Free Carriers, Excitons, and Sub-Bandgap States», *Adv. Energy Mater.*, vol. 10, n.º 13, p. 1903258, abr. 2020, doi: 10.1002/aenm.201903258.

[193] H.-S. Kim y N.-G. Park, «Importance of tailoring lattice strain in halide perovskite crystals», *NPG Asia Mater.*, vol. 12, n.º 1, p. 78, dic. 2020, doi: 10.1038/s41427-020-00265-w.

[194] A. Liang *et al.*, «Reassigning the Pressure-Induced Phase Transitions of Methylammonium Lead Bromide Perovskite», *J. Am. Chem. Soc.*, vol. 144, n.º 43, pp. 20099-20108, nov. 2022, doi: 10.1021/jacs.2c09457.

[195] Y. Chen *et al.*, «Strain engineering and epitaxial stabilization of halide perovskites», *Nature*, vol. 577, n.º 7789, pp. 209-215, ene. 2020, doi: 10.1038/s41586-019-1868-x.

[196] C. Zhu *et al.*, «Strain engineering in perovskite solar cells and its impacts on carrier dynamics», *Nat. Commun.*, vol. 10, n.º 1, p. 815, feb. 2019, doi: 10.1038/s41467-019-08507-4.

[197] K. M. Boopathi *et al.*, «Permanent Lattice Compression of Lead-Halide Perovskite for Persistently Enhanced Optoelectronic Properties», *ACS Energy Lett.*, vol. 5, n.º 2, pp. 642-649, feb. 2020, doi: 10.1021/acsenergylett.9b02810.

[198] M. R. Leyden *et al.*, «Methylammonium Lead Bromide Perovskite Light-Emitting Diodes by Chemical Vapor Deposition», *J. Phys. Chem. Lett.*, vol. 8, n.º 14, pp. 3193-3198, jul. 2017, doi: 10.1021/acs.jpclett.7b01093.

[199] J. M. Azpiroz, E. Mosconi, J. Bisquert, y F. De Angelis, «Defect migration in methylammonium lead iodide and its role in perovskite solar cell operation», *Energy Environ. Sci.*, vol. 8, n.º 7, pp. 2118-2127, 2015, doi: 10.1039/C5EE01265A.

[200] L. Mao *et al.*, «Organic Cation Alloying on Intralayer A and Interlayer A’ sites in 2D Hybrid Dion–Jacobson Lead Bromide Perovskites (A’)(A)Pb_2 Br_7», *J. Am. Chem. Soc.*, vol. 142, n.º 18, pp. 8342-8351, may 2020, doi: 10.1021/jacs.0c01625.

[201] E. J. Juarez-Perez, L. K. Ono, M. Maeda, Y. Jiang, Z. Hawash, y Y. Qi, «Photodecomposition and thermal decomposition in methylammonium halide lead perovskites and inferred design principles to increase photovoltaic device stability», *J. Mater. Chem. A*, vol. 6, n.º 20, pp. 9604-9612, 2018, doi: 10.1039/C8TA03501F.

[202] N. Aristidou *et al.*, «The Role of Oxygen in the Degradation of Methylammonium Lead Trihalide Perovskite Photoactive Layers», *Angew. Chem. Int. Ed.*, vol. 54, n.º 28, pp. 8208-8212, jul. 2015, doi: 10.1002/anie.201503153.

[203] I. S. Zhidkov *et al.*, «Temperature Dependence of Photochemical Degradation of MAPbBr3 Perovskite», *Coatings*, vol. 12, n.º 8, p. 1066, jul. 2022, doi: 10.3390/coatings12081066.

[204] M. L. De Giorgi, T. Lippolis, N. F. Jamaludin, C. Soci, A. Bruno, y M. Anni, «Origin of Amplified Spontaneous Emission Degradation in $MAPbBr_3$ Thin Films under Nanosecond-UV Laser Irradiation», *J. Phys. Chem. C*, vol. 124, n.º 19, pp. 10696-10704, may 2020, doi: 10.1021/acs.jpcc.0c02331.

[205] I. S. Zhidkov *et al.*, «XPS evidence of degradation mechanism in CH_3 NH_3 PbI_3 hybrid perovskite», *J. Phys. Condens. Matter*, vol. 32, n.º 9, p. 095501, feb. 2020, doi: 10.1088/1361-648X/ab576f.

[206] C. Das, M. Wussler, T. Hellmann, T. Mayer, y W. Jaegermann, «*In situ* XPS study of the surface chemistry of MAPI solar cells under operating conditions in vacuum», *Phys. Chem. Chem. Phys.*, vol. 20, n.º 25, pp. 17180-17187, 2018, doi: 10.1039/C8CP01259H.

[207] L. McGovern, M. H. Futscher, L. A. Muscarella, y B. Ehrler, «Understanding the Stability of $MAPbBr_3$ versus $MAPbI_3$: Suppression of Methylammonium Migration and Reduction of Halide Migration», *J. Phys. Chem. Lett.*, vol. 11, n.º 17, pp. 7127-7132, sep. 2020, doi: 10.1021/acs.jpclett.0c01822.

[208] D. R. Ceratti *et al.*, «Self-Healing Inside $APbBr_3$ Halide Perovskite Crystals», *Adv. Mater.*, vol. 30, n.º 10, p. 1706273, mar. 2018, doi: 10.1002/adma.201706273.

[209] G. Nan, X. Zhang, y G. Lu, «Self-Healing of Photocurrent Degradation in Perovskite Solar Cells: The Role of Defect-Trapped Excitons», *J. Phys. Chem. Lett.*, vol. 10, n.º 24, pp. 7774-7780, dic. 2019, doi: 10.1021/acs.jpclett.9b03413.

[210] M.-J. Zhang *et al.*, «Carrier Transport Improvement of CH_3 NH_3 PbI_3 Film by Methylamine Gas Treatment», *ACS Appl. Mater. Interfaces*, vol. 8, n.º 45, pp. 31413-31418, nov. 2016, doi: 10.1021/acsami.6b10418.

[211] Y. Zhang *et al.*, «Auto-passivation of crystal defects in hybrid imidazolium/methylammonium lead iodide films by fumigation with methylamine affords high efficiency perovskite solar cells», *Nano Energy*, vol. 58, pp. 105-111, abr. 2019, doi: 10.1016/j.nanoen.2019.01.027.

[212] M. T. Nayakasinghe, Y. Han, N. Sivapragasam, D. S. Kilin, N. Oncel, y U. Burghaus, «Adsorption of Formic Acid on CH_3 NH_3 PbI_3 Lead–Halide Organic–Inorganic Perovskites», *J. Phys. Chem. C*, vol. 123, n.º 37, pp. 22873-22886, sep. 2019, doi: 10.1021/acs.jpcc.9b03319.

[213] M. T. Nayakasinghe, Y. Han, N. Sivapragasam, D. S. Kilin, y U. Burghaus, «Unexpected high binding energy of CO_2 on CH_3 NH_3 PbI_3 lead-halide organic–inorganic perovskites *via* bicarbonate formation», *Chem. Commun.*, vol. 54, n.º 71, pp. 9949-9952, 2018, doi: 10.1039/C8CC04749A.

[214] J. Yang, B. D. Siempelkamp, D. Liu, y T. L. Kelly, «Investigation of CH_3 NH_3 PbI_3 Degradation Rates and Mechanisms in Controlled Humidity Environments Using *in Situ* Techniques», *ACS Nano*, vol. 9, n.º 2, pp. 1955-1963, feb. 2015, doi: 10.1021/nn506864k.

[215] W. Tress, «Metal Halide Perovskites as Mixed Electronic–Ionic Conductors: Challenges and Opportunities—From Hysteresis to Memristivity», *J. Phys. Chem. Lett.*, vol. 8, n.º 13, pp. 3106-3114, jul. 2017, doi: 10.1021/acs.jpclett.7b00975.

[216] P. Calado *et al.*, «Evidence for ion migration in hybrid perovskite solar cells with minimal hysteresis», *Nat. Commun.*, vol. 7, n.º 1, p. 13831, dic. 2016, doi: 10.1038/ncomms13831.

[217] P. Lopez-Varo *et al.*, «Effects of Ion Distributions on Charge Collection in Perovskite Solar Cells», *ACS Energy Lett.*, vol. 2, n.º 6, pp. 1450-1453, jun. 2017, doi: 10.1021/acsenergylett.7b00424.

[218] D. A. Jacobs *et al.*, «Hysteresis phenomena in perovskite solar cells: the many and varied effects of ionic accumulation», *Phys. Chem. Chem. Phys.*, vol. 19, n.º 4, pp. 3094-3103, 2017, doi: 10.1039/C6CP06989D.

[219] Y. Rong *et al.*, «Tunable hysteresis effect for perovskite solar cells», *Energy Environ. Sci.*, vol. 10, n.º 11, pp. 2383-2391, 2017, doi: 10.1039/C7EE02048A.

[220] S. Ravishankar *et al.*, «Influence of Charge Transport Layers on Open-Circuit Voltage and Hysteresis in Perovskite Solar Cells», *Joule*, vol. 2, n.º 4, pp. 788-798, abr. 2018, doi: 10.1016/j.joule.2018.02.013.

[221] O. Almora, I. Zarazua, E. Mas-Marza, I. Mora-Sero, J. Bisquert, y G. Garcia-Belmonte, «Capacitive Dark Currents, Hysteresis, and Electrode Polarization in Lead Halide Perovskite Solar Cells», *J. Phys. Chem. Lett.*, vol. 6, n.º 9, pp. 1645-1652, may 2015, doi: 10.1021/acs.jpclett.5b00480.

[222] P. Lopez-Varo *et al.*, «Device Physics of Hybrid Perovskite Solar cells: Theory and Experiment», *Adv. Energy Mater.*, vol. 8, n.º 14, p. 1702772, may 2018, doi: 10.1002/aenm.201702772.

[223] I. Zarazua, J. Bisquert, y G. Garcia-Belmonte, «Light-Induced Space-Charge Accumulation Zone as Photovoltaic Mechanism in Perovskite Solar Cells», *J. Phys. Chem. Lett.*, vol. 7, n.º 3, pp. 525-528, feb. 2016, doi: 10.1021/acs.jpclett.5b02810.

[224] D. Kumbhar, M. Jain, y A. Solanki, «Forming free non-volatile Resistive Switching mechanism in Ruddlesden Popper Perovskite Memristors», en *2022 International Conference for Advancement in Technology (ICONAT)*, Goa, India: IEEE, ene. 2022, pp. 1-6. doi: 10.1109/ICONAT53423.2022.9725938.

[225] K. Sakhatskyi *et al.*, «Assessing the Drawbacks and Benefits of Ion Migration in Lead Halide Perovskites», *ACS Energy Lett.*, vol. 7, n.º 10, pp. 3401-3414, oct. 2022, doi: 10.1021/acsenergylett.2c01663.

[226] K. Rogdakis *et al.*, «Mixed-Halide Perovskite Memristors with Gate-Tunable Functions Operating at Low-Switching Electric Fields», *Adv. Electron. Mater.*, vol. 9, n.º 12, p. 2300424, dic. 2023, doi: 10.1002/aelm.202300424.

[227] «Implementation of an artificial neuron circuit model based on high speed AlN stacked threshold switching devices», *Front. Phys.*, vol. 20, n.º 3, p. 34201, 2025, doi: 10.15302/frontphys.2025.034201.

[228] S. Parveen, L. T. Manamel, A. Mukherjee, S. Sagar, y B. C. Das, «Analog Memristor of Lead-Free Cs_4 $CuSb_2$ Cl_{12} Layered Double Perovskite Nanocrystals as Solid-State Electronic Synapse for

Neuromorphic Computing», *Adv. Mater. Interfaces*, vol. 9, n.º 30, p. 2200562, oct. 2022, doi: 10.1002/admi.202200562.

[229] Y. Zhuo *et al.*, «A Dynamical Compact Model of Diffusive and Drift Memristors for Neuromorphic Computing», *Adv. Electron. Mater.*, vol. 8, n.º 8, p. 2100696, ago. 2022, doi: 10.1002/aelm.202100696.

[230] E. J. Fuller *et al.*, «Parallel programming of an ionic floating-gate memory array for scalable neuromorphic computing».

[231] G. Karunaratne *et al.*, «Robust high-dimensional memory-augmented neural networks», *Nat. Commun.*, vol. 12, n.º 1, p. 2468, abr. 2021, doi: 10.1038/s41467-021-22364-0.

[232] B. Hwang y J.-S. Lee, «Hybrid Organic-Inorganic Perovskite Memory with Long-Term Stability in Air», *Sci. Rep.*, vol. 7, n.º 1, p. 673, 2017, doi: 10.1038/s41598-017-00778-5.

[233] P. C. Harikesh, B. Febriansyah, R. A. John, y N. Mathews, «Hybrid organic–inorganic halide perovskites for scaled-in neuromorphic devices», *MRS Bull.*, vol. 45, n.º 8, pp. 641-648, ago. 2020, doi: 10.1557/mrs.2020.193.

[234] M.-C. Yen *et al.*, «All-inorganic perovskite quantum dot light-emitting memories», *Nat. Commun.*, vol. 12, n.º 1, p. 4460, jul. 2021, doi: 10.1038/s41467-021-24762-w.

[235] H. Kim, J. S. Han, S. G. Kim, S. Y. Kim, y H. W. Jang, «Halide perovskites for resistive random-access memories», *J. Mater. Chem. C*, vol. 7, n.º 18, pp. 5226-5234, 2019, doi: 10.1039/C8TC06031B.

[236] D.-H. Kwon *et al.*, «Atomic structure of conducting nanofilaments in TiO2 resistive switching memory», *Nat. Nanotechnol.*, vol. 5, n.º 2, pp. 148-153, feb. 2010, doi: 10.1038/nnano.2009.456.

[237] E. Yoo, M. Lyu, J.-H. Yun, C. Kang, Y. Choi, y L. Wang, «Bifunctional resistive switching behavior in an organolead halide perovskite based Ag/CH_3 NH_3 PbI_{3-x} Cl_x /FTO structure», *J. Mater. Chem. C*, vol. 4, n.º 33, pp. 7824-7830, 2016, doi: 10.1039/C6TC02503J.

[238] C. Wang, W. Cao, H. Shen, H. Gao, H. Zhou, y X. Guo, «Crystal Structure, Band Gap, and Optoelectronic Performance of Lead-Free Cs_2 $FeCl_5$ $\cdot H_2$ O Erythrosiderite-Halide Single Crystal and Its Thin Film», *Eur. J. Inorg. Chem.*, vol. 28, n.º 5, p. e202400628, feb. 2025, doi: 10.1002/ejic.202400628.

[239] R. A. John *et al.*, «Reconfigurable halide perovskite nanocrystal memristors for neuromorphic computing», *Nat. Commun.*, vol. 13, n.º 1, p. 2074, abr. 2022, doi: 10.1038/s41467-022-29727-1.

[240] H. Fang *et al.*, «Band-Edge Exciton Fine Structure and Exciton Recombination Dynamics in Single Crystals of Layered Hybrid Perovskites», *Adv. Funct. Mater.*, vol. 30, n.º 6, p. 1907979, feb. 2020, doi: 10.1002/adfm.201907979.

[241] F. Zhang *et al.*, «Self-Seeding Growth for Perovskite Solar Cells with Enhanced Stability», *Joule*, vol. 3, n.º 6, pp. 1452-1463, jun. 2019, doi: 10.1016/j.joule.2019.03.023.

[242] M. Chen, Y. Yuan, Y. Liu, D. Cao, y C. Xu, «High-quality all-inorganic $CsPbBr_3$ single crystals prepared by a facile one-step solution growth method», *RSC Adv.*, vol. 12, n.º 23, pp. 14838-14843, 2022, doi: 10.1039/D2RA01900K.

[243] F. Zhou, Y. Liu, X. Shen, M. Wang, F. Yuan, y Y. Chai, «Low-Voltage, Optoelectronic CH3NH3PbI3−xClx Memory with Integrated Sensing and Logic Operations», *Adv. Funct. Mater.*, vol. 28, n.º 15, 2018, doi: 10.1002/adfm.201800080.

[244] H. Cai, G. Ma, Y. He, L. Lu, J. Zhang, y H. Wang, «Compact pure phase CsPbBr3 perovskite film with significantly improved stability for high-performance memory», *Ceram. Int.*, vol. 45, n.º 1, pp. 1150-1155, 2019, doi: 10.1016/j.ceramint.2018.09.297.

[245] C. Zou, L. He, y L. Y. Lin, «Vacuum-Deposited Inorganic Perovskite Memory Arrays with Long-Term Ambient Stability», *Phys. Status Solidi - Rapid Res. Lett.*, vol. 13, n.º 9, pp. 1-6, 2019, doi: 10.1002/pssr.201900182.

[246] J. H. Heo *et al.*, «Memory effect behavior with respect to the crystal grain size in the organic-inorganic hybrid perovskite nonvolatile resistive random access memory», *Sci. Rep.*, vol. 7, n.º 1, pp. 1-8, 2017, doi: 10.1038/s41598-017-16805-4.

[247] Y. H. Lee, D. H. Kim, C. Wu, y T. W. Kim, «Memristive devices with a large memory margin based on nanocrystalline organic-inorganic hybrid CH3NH3PbBr3 perovskite active layer», *Org. Electron.*, vol. 62, n.º August, pp. 412-418, 2018, doi: 10.1016/j.orgel.2018.08.034.

[248] C. Gu y J. S. Lee, «Flexible Hybrid Organic-Inorganic Perovskite Memory», *ACS Nano*, vol. 10, n.º 5, pp. 5413-5418, 2016, doi: 10.1021/acsnano.6b01643.

[249] B. M. Bresolin, C. Günnemann, D. W. Bahnemann, y M. Sillanpää, «Pb-free Cs3Bi2I9 perovskite as a visible-light-active photocatalyst for organic pollutant degradation», *Nanomaterials*, vol. 10, n.º 4, pp. 1-13, 2020, doi: 10.3390/nano10040763.

[250] G. Lin *et al.*, «An organic-inorganic hybrid perovskite logic gate for better computing», *J. Mater. Chem. C*, vol. 3, n.º 41, pp. 10793-10798, 2015, doi: 10.1039/c5tc02270c.

[251] J. Choi *et al.*, «Organolead Halide Perovskites for Low Operating Voltage Multilevel Resistive Switching», *Adv. Mater.*, vol. 28, n.º 31, pp. 6562-6567, 2016, doi: 10.1002/adma.201600859.

[252] Y. Wang *et al.*, «Photonic Synapses Based on Inorganic Perovskite Quantum Dots for Neuromorphic Computing», *Adv. Mater.*, vol. 30, n.º 38, pp. 1-9, 2018, doi: 10.1002/adma.201802883.

[253] K. Kang *et al.*, «High-Performance Solution-Processed Organo-Metal Halide Perovskite Unipolar Resistive Memory Devices in a Cross-Bar Array Structure», *Adv. Mater.*, vol. 31, n.º 21, pp. 1-9, 2019, doi: 10.1002/adma.201804841.

[254] Y.-X. Chen *et al.*, «General Space-Confined On-Substrate Fabrication of Thickness-Adjustable Hybrid Perovskite Single-Crystalline Thin Films», *J. Am. Chem. Soc.*, vol. 138, n.º 50, pp. 16196-16199, dic. 2016, doi: 10.1021/jacs.6b09388.

[255] D. Bogachuk *et al.*, «Perovskite Solar Cells with Carbon-Based Electrodes – Quantification of Losses and Strategies to Overcome Them», *Adv. Energy Mater.*, vol. 12, n.º 10, p. 2103128, mar. 2022, doi: 10.1002/aenm.202103128.

[256] D. Bogachuk *et al.*, «Low-temperature carbon-based electrodes in perovskite solar cells», *Energy Environ. Sci.*, vol. 13, n.º 11, pp. 3880-3916, 2020, doi: 10.1039/D0EE02175J.

[257] D. Sanjay Khone, S. Bera, y A. Singh Rana, «Investigations of endurance and retention in tantalum oxide based memristor», *Mater. Today Proc.*, p. S2214785323012804, mar. 2023, doi: 10.1016/j.matpr.2023.03.238.

[258] S. G. Kim *et al.*, «Dual-Phase All-Inorganic Cesium Halide Perovskites for Conducting-Bridge Memory-Based Artificial Synapses», *Adv. Funct. Mater.*, vol. 29, n.º 49, p. 1906686, dic. 2019, doi: 10.1002/adfm.201906686.

[259] J. J. Yang, D. B. Strukov, y D. R. Stewart, «Memristive devices for computing», *Nat. Nanotechnol.*, vol. 8, n.º 1, pp. 13-24, ene. 2013, doi: 10.1038/nnano.2012.240.

[260] Y.-W. Hsiao, S.-Y. Wang, C.-L. Huang, C.-C. Leu, y C.-F. Shih, «Resistive Switching Property of Organic–Inorganic Tri-Cation Lead Iodide Perovskite Memory Device», *Nanomaterials*, vol. 10, n.º 6, p. 1155, jun. 2020, doi: 10.3390/nano10061155.

[261] D. Li *et al.*, «MoS_2 Memristors Exhibiting Variable Switching Characteristics toward Biorealistic Synaptic Emulation», *ACS Nano*, vol. 12, n.º 9, pp. 9240-9252, sep. 2018, doi: 10.1021/acsnano.8b03977.

[262] O. Almora *et al.*, «Discerning recombination mechanisms and ideality factors through impedance analysis of high-efficiency perovskite solar cells», *Nano Energy*, vol. 48, pp. 63-72, jun. 2018, doi: 10.1016/j.nanoen.2018.03.042.

[263] S.-M. Yoo, S. J. Yoon, J. A. Anta, H. J. Lee, P. P. Boix, y I. Mora-Seró, «An Equivalent Circuit for Perovskite Solar Cell Bridging Sensitized to Thin Film Architectures», *Joule*, vol. 3, n.º 10, pp. 2535-2549, oct. 2019, doi: 10.1016/j.joule.2019.07.014.

[264] C. Gonzales, A. Bou, A. Guerrero, y J. Bisquert, «Capacitive and Inductive Characteristics of Volatile Perovskite Resistive Switching Devices with Analog Memory», *J. Phys. Chem. Lett.*, vol. 15, n.º 25, pp. 6496-6503, jun. 2024, doi: 10.1021/acs.jpclett.4c00945.

[265] C. Gonzales, A. Guerrero, y J. Bisquert, «Transition from Capacitive to Inductive Hysteresis: A Neuron-Style Model to Correlate $I - V$ Curves to Impedances of Metal Halide Perovskites», *J. Phys. Chem. C*, vol. 126, n.º 32, pp. 13560-13578, ago. 2022, doi: 10.1021/acs.jpcc.2c02729.

[266] F. Ebadi, N. Taghavinia, R. Mohammadpour, A. Hagfeldt, y W. Tress, «Origin of apparent light-enhanced and negative capacitance in perovskite solar cells», *Nat. Commun.*, vol. 10, n.º 1, p. 1574, abr. 2019, doi: 10.1038/s41467-019-09079-z.

[267] D. A. Jacobs *et al.*, «The two faces of capacitance: New interpretations for electrical impedance measurements of perovskite solar cells and their relation to hysteresis», *J. Appl. Phys.*, vol. 124, n.º 22, p. 225702, dic. 2018, doi: 10.1063/1.5063259.

[268] D. Klotz, «Negative capacitance or inductive loop? – A general assessment of a common low frequency impedance feature», *Electrochem. Commun.*, vol. 98, pp. 58-62, ene. 2019, doi: 10.1016/j.elecom.2018.11.017.

[269] J. Bisquert y A. Guerrero, «Chemical Inductor», *J. Am. Chem. Soc.*, vol. 144, n.º 13, pp. 5996-6009, abr. 2022, doi: 10.1021/jacs.2c00777.

[270] E. Hernández-Balaguera y J. Bisquert, «Negative Transient Spikes in Halide Perovskites», *ACS Energy Lett.*, vol. 7, n.º 8, pp. 2602-2610, ago. 2022, doi: 10.1021/acsenergylett.2c01252.

[271] M. Berruet *et al.*, «Physical Model for the Current–Voltage Hysteresis and Impedance of Halide Perovskite Memristors», *ACS Energy Lett.*, vol. 7, n.º 3, pp. 1214-1222, mar. 2022, doi: 10.1021/acsenergylett.2c00121.

[272] J. Bisquert, «Electrical Charge Coupling Dominates the Hysteresis Effect of Halide Perovskite Devices», *J. Phys. Chem. Lett.*, vol. 14, n.º 4, pp. 1014-1021, feb. 2023, doi: 10.1021/acs.jpclett.2c03812.

[273] H. Wang, A. Guerrero, A. Bou, A. M. Al-Mayouf, y J. Bisquert, «Kinetic and material properties of interfaces governing slow response and long timescale phenomena in perovskite solar cells», *Energy Environ. Sci.*, vol. 12, n.º 7, pp. 2054-2079, 2019, doi: 10.1039/C9EE00802K.

[274] G. Zhou *et al.*, «Second-order associative memory circuit hardware implemented by the evolution from battery-like capacitance to resistive switching memory», *iScience*, vol. 25, n.º 10, p. 105240, oct. 2022, doi: 10.1016/j.isci.2022.105240.

[275] H. Rong, H. Zhang, S. Xiao, C. Li, y C. Hu, «Optimizing energy consumption for data centers», *Renew. Sustain. Energy Rev.*, vol. 58, pp. 674-691, 2016, doi: 10.1016/j.rser.2015.12.283.

[276] H. S. P. Wong y S. Salahuddin, «Memory leads the way to better computing», *Nat. Nanotechnol.*, vol. 10, n.º 3, pp. 191-194, 2015, doi: 10.1038/nnano.2015.29.

[277] H. Seok, D. Lee, S. Son, H. Choi, G. Kim, y T. Kim, «Beyond von Neumann Architecture: Brain-Inspired Artificial Neuromorphic Devices and Integrated Computing», *Adv. Electron. Mater.*, vol. 10, n.º 8, 2024, doi: 10.1002/aelm.202300839.

[278] H. Chen *et al.*, «Improved charge extraction in inverted perovskite solar cells with dual-site-binding ligands», *Science*, vol. 384, n.º 6692, pp. 189-193, 2024, doi: 10.1126/science.adm9474.

[279] J. Thiesbrummel *et al.*, «Ion-induced field screening as a dominant factor in perovskite solar cell operational stability», *Nat. Energy*, vol. 9, n.º 6, pp. 664-676, 2024, doi: 10.1038/s41560-024-01487-w.

[280] C. A. Aranda, A. O. Alvarez, V. S. Chivrony, C. Das, M. Rai, y M. Saliba, «Overcoming ionic migration in perovskite solar cells through alkali metals», *Joule*, vol. 8, n.º 1, pp. 241-254, 2024, doi: 10.1016/j.joule.2023.11.011.

[281] C. Zhang, Y. Li, C. Ma, y Q. Zhang, «Recent Progress of Organic–Inorganic Hybrid Perovskites in RRAM, Artificial Synapse, and Logic Operation», *Small Sci.*, vol. 2, n.º 2, 2022, doi: 10.1002/smsc.202100086.

[282] W. Peixiong *et al.*, «A mini review of recently progress on halide perovskite memristor devices: materials sciences, challenges and applications», *Mater. Today Energy*, vol. 45, p. 101692, 2024, doi: 10.1016/j.mtener.2024.101692.

[283] I. Fernandez-Guillen *et al.*, «Perovskite Thin Single Crystal for a High Performance and Long Endurance Memristor», *Adv. Electron. Mater.*, vol. 10, n.º 5, pp. 1-9, 2024, doi: 10.1002/aelm.202300475.

[284] R. A. John *et al.*, «Reconfigurable halide perovskite nanocrystal memristors for neuromorphic computing», *Nat. Commun.*, vol. 13, n.º 1, pp. 1-10, 2022, doi: 10.1038/s41467-022-29727-1.

[285] F. Luo, W. M. Zhong, X. G. Tang, J. Y. Chen, Y. P. Jiang, y Q. X. Liu, «Application of artificial synapse based on all-inorganic perovskite memristor in neuromorphic computing», *Nano Mater. Sci.*, vol. 6, n.º 1, pp. 68-76, 2024, doi: 10.1016/j.nanoms.2023.01.003.

[286] I. H. Im *et al.*, «Halide Perovskites-Based Diffusive Memristors for Artificial Mechano-Nociceptive System», *Adv. Mater.*, vol. 36, n.º 1, pp. 1-13, 2024, doi: 10.1002/adma.202307334.

[287] M. Kumar, H. S. Kim, D. Y. Park, M. S. Jeong, y J. Kim, «Compliance-Free Multileveled Resistive Switching in a Transparent 2D Perovskite for Neuromorphic Computing», *ACS Appl. Mater. Interfaces*, vol. 10, n.º 15, pp. 12768-12772, 2018, doi: 10.1021/acsami.7b19406.

[288] S. Zhai *et al.*, «Multilevel resistive switching in stable all-inorganic n-i-p double perovskite memristor», *iScience*, vol. 26, n.º 4, p. 106461, 2023, doi: 10.1016/j.isci.2023.106461.

[289] S. Y. Kim, H. Zhang, y J. Rubio-Magnieto, «Operating Mechanism Principles and Advancements for Halide Perovskite-Based Memristors and Neuromorphic Devices», *J. Phys. Chem. Lett.*, pp. 10087-10103, 2024, doi: 10.1021/acs.jpclett.4c02170.

[290] B. Li *et al.*, «Metal halide perovskites for resistive switching memory devices and artificial synapses», *J. Mater. Chem. C*, vol. 7, n.º 25, pp. 7476-7493, 2019, doi: 10.1039/c9tc02233c.

[291] H. L. Park y T. W. Lee, «Organic and perovskite memristors for neuromorphic computing», *Org. Electron.*, vol. 98, n.º April, p. 106301, 2021, doi: 10.1016/j.orgel.2021.106301.

[292] J. Yang *et al.*, «A Perovskite Memristor with Large Dynamic Space for Analog-Encoded Image Recognition», *ACS Nano*, vol. 16, n.º 12, pp. 21324-21333, 2022, doi: 10.1021/acsnano.2c09569.

[293] S. P. Dunfield *et al.*, «From Defects to Degradation: A Mechanistic Understanding of Degradation in Perovskite Solar Cell Devices and Modules», *Adv. Energy Mater.*, vol. 10, n.º 26, pp. 1-35, 2020, doi: 10.1002/aenm.201904054.

[294] D. Yang, X. Li, y H. Zeng, «Surface Chemistry of All Inorganic Halide Perovskite Nanocrystals: Passivation Mechanism and Stability», *Adv. Mater. Interfaces*, vol. 5, n.º 8, pp. 1-13, 2018, doi: 10.1002/admi.201701662.

[295] A. J. Barker *et al.*, «Defect-Assisted Photoinduced Halide Segregation in Mixed-Halide Perovskite Thin Films», *ACS Energy Lett.*, vol. 2, n.º 6, pp. 1416-1424, 2017, doi: 10.1021/acsenergylett.7b00282.

[296] M. Ledinsky *et al.*, «Impact of cation multiplicity on halide perovskite defect densities and solar cell voltages», *J. Phys. Chem. C*, vol. 124, n.º 50, pp. 27333-27339, 2020, doi: 10.1021/acs.jpcc.0c08193.

[297] H. Zai, Y. Ma, Q. Chen, y H. Zhou, «Ion migration in halide perovskite solar cells: Mechanism, characterization, impact and suppression», *J. Energy Chem.*, vol. 63, pp. 528-549, 2021, doi: 10.1016/j.jechem.2021.08.006.

[298] A. J. Barker *et al.*, «Defect-Assisted Photoinduced Halide Segregation in Mixed-Halide Perovskite Thin Films», *ACS Energy Lett.*, vol. 2, n.º 6, pp. 1416-1424, 2017, doi: 10.1021/acsenergylett.7b00282.

[299] Y.-X. Chen *et al.*, «General Space-Confined On-Substrate Fabrication of Thickness-Adjustable Hybrid Perovskite Single-Crystalline Thin Films», *J. Am. Chem. Soc.*, vol. 138, n.º 50, pp. 16196-16199, dic. 2016, doi: 10.1021/jacs.6b09388.

[300] S. Shrestha *et al.*, «Long carrier diffusion length in two-dimensional lead halide perovskite single crystals», *Chem*, vol. 8, n.º 4, pp. 1107-1120, 2022, doi: 10.1016/j.chempr.2022.01.008.

[301] B. Turedi *et al.*, «Single-Crystal Perovskite Solar Cells Exhibit Close to Half A Millimeter Electron-Diffusion Length», *Adv. Mater.*, vol. 34, n.º 47, pp. 1-9, 2022, doi: 10.1002/adma.202202390.

[302] J. Zhang *et al.*, «Carrier Diffusion and Recombination Anisotropy in the MAPbI3 Single Crystal», *ACS Appl. Mater. Interfaces*, vol. 13, n.º 25, pp. 29827-29834, 2021, doi: 10.1021/acsami.1c07056.

[303] Z. Chen *et al.*, «Single-Crystal MAPbI3 Perovskite Solar Cells Exceeding 21% Power Conversion Efficiency», *ACS Energy Lett.*, vol. 4, n.º 6, pp. 1258-1259, 2019, doi: 10.1021/acsenergylett.9b00847.

[304] Y. Nakamura, N. Shibayama, A. Hori, T. Matsushita, H. Segawa, y T. Kondo, «Crystal Systems and Lattice Parameters of CH3NH3Pb(I1-xBrx)3 Determined Using Single Crystals: Validity of Vegard's Law», *Inorg. Chem.*, vol. 59, n.º 10, pp. 6709-6716, 2020, doi: 10.1021/acs.inorgchem.9b03421.

[305] A. Liang *et al.*, «Reassigning the Pressure-Induced Phase Transitions of Methylammonium Lead Bromide Perovskite», *J. Am. Chem. Soc.*, vol. 144, n.º 43, pp. 20099-20108, 2022, doi: 10.1021/jacs.2c09457.

[306] S. Y. Kim *et al.*, «Ternary diagrams of the phase, optical bandgap energy and photoluminescence of mixed-halide perovskites», *Acta Mater.*, vol. 181, pp. 460-469, 2019, doi: 10.1016/j.actamat.2019.10.008.

[307] W. Wang *et al.*, «Growth of mixed-halide perovskite single crystals», *CrystEngComm*, vol. 20, n.º 12, pp. 1635-1643, 2018, doi: 10.1039/c7ce01691c.

[308] C. M. Sutter-Fella *et al.*, «High Photoluminescence Quantum Yield in Band Gap Tunable Bromide Containing Mixed Halide Perovskites», *Nano Lett.*, vol. 16, n.º 1, pp. 800-806, 2016, doi: 10.1021/acs.nanolett.5b04884.

[309] A. J. Barker *et al.*, «Defect-Assisted Photoinduced Halide Segregation in Mixed-Halide Perovskite Thin Films», *ACS Energy Lett.*, vol. 2, n.º 6, pp. 1416-1424, 2017, doi: 10.1021/acsenergylett.7b00282.

[310] A. J. Knight *et al.*, «Halide Segregation in Mixed-Halide Perovskites: Influence of A-Site Cations», *ACS Energy Lett.*, vol. 6, n.º 2, pp. 799-808, 2021, doi: 10.1021/acsenergylett.0c02475.

[311] E. T. Hoke, D. J. Slotcavage, E. R. Dohner, A. R. Bowring, H. I. Karunadasa, y M. D. McGehee, «Reversible photo-induced trap formation in mixed-halide hybrid perovskites for photovoltaics», *Chem. Sci.*, vol. 6, n.º 1, pp. 613-617, 2015, doi: 10.1039/c4sc03141e.

[312] M. Lanza *et al.*, «Standards for the Characterization of Endurance in Resistive Switching Devices», *ACS Nano*, vol. 15, n.º 11, pp. 17214-17231, 2021, doi: 10.1021/acsnano.1c06980.

[313] M. Zhao, B. Gao, Y. Xi, F. Xu, H. Wu, y H. Qian, «Endurance and Retention Degradation of Intermediate Levels in Filamentary Analog RRAM», *IEEE J. Electron Devices Soc.*, vol. 7, n.º July, pp. 1239-1247, 2019, doi: 10.1109/JEDS.2019.2943017.

[314] P. Mark y W. Helfrich, «Space-charge-limited currents in organic crystals», *J. Appl. Phys.*, vol. 33, n.º 1, pp. 205-215, 1962, doi: 10.1063/1.1728487.

[315] R. H. Bube, «Trap Density Determination by Space-Charge-Limited Currents», *J. Appl. Phys.*, vol. 33, n.º 5, pp. 1733-1737, 1962, doi: 10.1063/1.1728818.

[316] J. Siekmann, S. Ravishankar, y T. Kirchartz, «Apparent Defect Densities in Halide Perovskite Thin Films and Single Crystals», *ACS Energy Lett.*, vol. 6, n.º 9, pp. 3244-3251, 2021, doi: 10.1021/acsenergylett.1c01449.

[317] D. Meggiolaro, E. Mosconi, y F. De Angelis, «Formation of Surface Defects Dominates Ion Migration in Lead-Halide Perovskites», *ACS Energy Lett.*, vol. 4, n.º 3, pp. 779-785, 2019, doi: 10.1021/acsenergylett.9b00247.

[318] H. Zai, Y. Ma, Q. Chen, y H. Zhou, «Ion migration in halide perovskite solar cells: Mechanism, characterization, impact and suppression», *J. Energy Chem.*, vol. 63, pp. 528-549, 2021, doi: 10.1016/j.jechem.2021.08.006.